SIMULATIONS OF THE SMALL-SCALE TURBULENT DYNAMO

ALEXANDER A. SCHEKOCHIHIN,[1] STEVEN C. COWLEY,[2] AND SAMUEL F. TAYLOR[3]

Plasma Physics Group, Imperial College, Blackett Laboratory, Prince Consort Road, London SW7 2BW, UK

JASON L. MARON[4]

Department of Physics and Astronomy, University of Rochester, Rochester, NY 14627; and Center for Magnetic Reconnection Studies,
Department of Physics and Astronomy, University of Iowa, 203 Van Allen Hall, Iowa City, IA 52242

AND

JAMES C. MCWILLIAMS

Department of Atmospheric Sciences, UCLA, Los Angeles, CA 90095-1565

ABSTRACT

We report the results of an extensive numerical study of the small-scale turbulent dynamo. The primary focus is on the case of large magnetic Prandtl numbers Pr_m, which is relevant for hot low-density astrophysical plasmas. A Pr_m parameter scan is given for the model case of viscosity-dominated (low Reynolds number) turbulence. We concentrate on three topics: magnetic energy spectra and saturation levels, the structure of the magnetic field lines, and intermittency of the field strength distribution. The main results are as follows: (1) the folded structure of the field (direction reversals at the resistive scale, field lines curved at the scale of the flow) persists from the kinematic to the nonlinear regime; (2) the field distribution is self-similar and appears to be lognormal during the kinematic regime and exponential in the saturated state; and (3) the bulk of the magnetic energy is at the resistive scale in the kinematic regime and remains there after saturation, although the magnetic energy spectrum becomes much shallower. We propose an analytical model of saturation based on the idea of partial two-dimensionalization of the velocity gradients with respect to the local direction of the magnetic folds. The model-predicted saturated spectra are in excellent agreement with numerical results. Comparisons with large-Re, moderate-Pr_m runs are carried out to confirm the relevance of these results and to test heuristic scenarios of dynamo saturation. New features at large Re are elongation of the folds in the nonlinear regime from the viscous scale to the box scale and the presence of an intermediate nonlinear stage of slower than exponential magnetic energy growth accompanied by an increase of the resistive scale and partial suppression of the kinetic energy spectrum in the inertial range. Numerical results for the saturated state do not support scale-by-scale equipartition between magnetic and kinetic energies, with a definite excess of magnetic energy at small scales. A physical picture of the saturated state is proposed.

Subject headings: magnetic fields — methods: numerical — MHD — plasmas — turbulence

1. INTRODUCTION

1.1. *Large- and Small-Scale Magnetic Fields in Astrophysics*

Magnetic fields are detected everywhere in the universe: stars, accretion disks, galaxies, and galaxy clusters all carry dynamically important magnetic fields (some of the relevant reviews and observations are Kronberg 1994, 2002; Beck et al. 1996; Minter & Spangler 1996; Zweibel & Heiles 1997; Vallée 1997, 1998; Balbus & Hawley 1998; Kulsrud 1999; Weiss & Tobias 2000; Title 2000; Beck 2000, 2001; Ferrière 2001; Kronberg et al. 2001; Carilli & Taylor 2002; Han & Wielebinski 2002; Widrow 2002; Tobias 2002; Ossendrijver 2003; Han et al. 2004; Brandenburg & Subramanian 2004). There are two kinds of magnetic fields observed. First, there are *large-scale fields*, i.e., fields spatially coherent at scales comparable to the size of the astrophysical object that they inhabit. Two examples of such fields are the cyclic dipolar field of the Sun and the spiral fields of galaxies. Second, there are *small-scale fields*, e.g., the fluctuating fields in the solar photosphere, galaxies, and clusters. They are associated with the turbulent motions of the constituent plasmas and exist at scales below those at which the turbulence is forced. Both types of fields are usually strong enough to be dynamically important. The challenge is to construct a theory of their origin, evolution, and structure consistent with observations and to understand the role these fields play in the dynamics of astrophysical objects.

A physically plausible scenario for the origin and maintenance of these fields is a turbulent dynamo, which would amplify a weak seed field and culminate in a nonlinear saturated state. Just as magnetic fields can be classified into large- and small-scale varieties, there are also two kinds of dynamo responsible for these fields. First, three-dimensional velocity fields sufficiently random in space and/or time will amplify small-scale magnetic fluctuations via random stretching of the field lines (Batchelor 1950; Zel'dovich et al. 1984; Childress & Gilbert 1995). Since it is a small-scale process, we believe that this *small-scale dynamo* can be studied in a homogeneous and isotropic setting. In contrast, the generation and structure

of the large-scale magnetic fields cannot be understood without going beyond the homogeneous picture and taking into account large-scale object-specific features: boundary conditions, rotation, helicity, mean velocity shear, density stratification, etc. These effects can combine with turbulence to give rise to the second kind of dynamo: the *large-scale dynamo*. This is usually handled in the mean-field framework (e.g., Moffatt 1978; Parker 1979; Ruzmaikin et al. 1988; Brandenburg & Subramanian 2004). Mean-field theories tend to assume that all small-scale magnetic fluctuations result from the shredding of the mean field by the turbulence. Such *induced small-scale fields* do exist, but they vanish if the mean field vanishes and are distinct from the dynamo-generated small-scale fields. Neglecting the latter is, in fact, not a priori justified because the small-scale dynamo is usually much faster than the large-scale one: it amplifies magnetic energy at the rate of turbulent stretching and produces dynamically significant fields before the large-scale fields can grow appreciably (e.g., Kulsrud & Anderson 1992; Kulsrud 1999). Procedures that have been devised for incorporating the effect of the small-scale fields into the mean-field theory (Vainshtein & Kichatinov 1983; Rädler et al. 2003 and references therein) usually do not evolve the small-scale component self-consistently, requiring instead certain statistical information about the small-scale fields to be supplied at the modeling stage. Thus, solving the large-scale problem is predicated on making correct assumptions about the small scales.

Whether the magnetic fields are dynamo generated or stem from primordial and/or external mechanisms (Kulsrud et al. 1997a; Kronberg et al. 2001), the key question is how they are maintained in the course of their interaction with the ambient turbulence. Unless the large-scale field is extremely strong, we must always ask why it is not quickly churned up by the small-scale turbulence. Any large-scale field configuration must be consistent with the presence and continued regeneration of considerable amounts of small-scale magnetic energy. In galaxies and clusters, both large- and small-scale fields are in the microgauss range, which corresponds to magnetic energy densities in approximate equipartition with the kinetic energy density of the turbulent motions in these objects. This suggests that we are observing a self-consistent nonlinear state of MHD turbulence.

While it is surely the interplay between motions and magnetic fields at disparate scales that ultimately determines the nature of the observed states, the above considerations motivate us to focus on the homogeneous isotropic small-scale MHD turbulence. From the point of view of theoretical physics, this is an attempt to understand the universal features before tackling the object-specific ones. From the point of view of numerical experimentation, this approach is unavoidable because simulating the full picture requires resolving *multiple* scale separations that are well beyond the capabilities of current computers and are likely to remain so for many years to come.

1.2. *The Scales in the Problem*

The issue of multiple scale ranges is important, so let us examine it in more detail. The hierarchy of scales in an astrophysical object can be outlined as follows. The largest spatial scale is the system size L. The energy that feeds the turbulence is injected at the outer, or forcing, scale l_0. For objects with nontrivial geometry such as stars or galactic disks, $l_0 \ll L$. This is the first scale separation in the problem. It is used by mean-field theories to split all fields into mean and
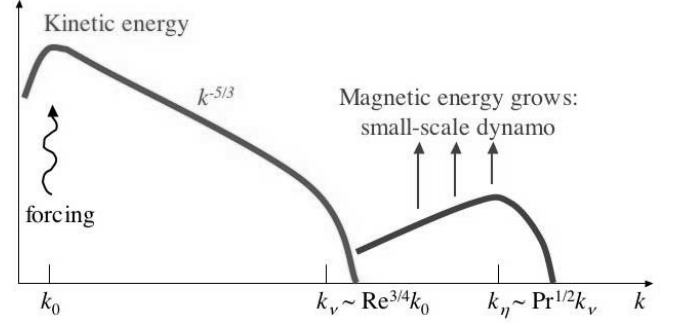

Fig. 1.—Sketch of scale ranges and energy spectra in a large-Pr_m medium.

fluctuating components with averages being done over scales of order and below l_0.

The energy cascades from l_0 down to the viscous dissipation scale l_ν. In purely hydrodynamic systems, the latter is called the Kolmogorov inner scale. Kolmogorov's 1941 dimensional theory of turbulence (e.g., Frisch 1995) gives $l_\nu \sim \mathrm{Re}^{-3/4} l_0$. The hydrodynamic Reynolds number $\mathrm{Re} \sim u_0 l_0 / \nu$ is usually fairly large for astrophysical systems, so $l_\nu \ll l_0$ (u_0 is the typical velocity at the outer scale, ν is the fluid viscosity). This is the second scale separation in the problem. It is at scales between the outer and the inner scale—the inertial range—that the universal physics of turbulence is contained.

If magnetic fields are present, they bring in their own dissipation scale l_η associated with the magnetic diffusivity η of the plasma (Spitzer 1962). The ratio $\mathrm{Pr}_m = \nu/\eta$ is called the magnetic Prandtl number. Using the Spitzer values for the viscosity and magnetic diffusivity of a fully ionized plasma, one finds $\mathrm{Pr}_m \sim 10^{-5} T^4/n$, where T is temperature in K and n is the particle concentration in cm^{-3}. In the case of a partially ionized gas with neutral-dominated viscosity (e.g., warm interstellar medium), we can estimate $\nu \sim v_{\mathrm{th}}/\sigma n$, where v_{th} is the thermal speed and σ is the atomic cross section. The formula for Pr_m is then $\mathrm{Pr}_m \sim 10^7 T^2/n$. In hot low-density plasmas such as (warm) interstellar and intracluster media, as well as in some accretion disks, $\mathrm{Pr}_m \gg 1$ (see, e.g., Brandenburg & Subramanian 2004). Systems with $\mathrm{Pr}_m \gg 1$ will be the primary focus of this paper. If a weak magnetic field is amplified by Kolmogorov turbulence, the magnetic energy exponentiation time is the same as the turnover time of the viscous-scale eddies because these eddies are the fastest ones. Balancing the viscous eddy turnover time with the magnetic field diffusion time gives an estimate for the resistive scale in the kinematic (weak field) regime: $l_\eta \sim \mathrm{Pr}_m^{-1/2} l_\nu$. As $\mathrm{Pr}_m \gg 1$, $l_\eta \ll l_\nu$. This is the third scale separation in the problem. The scale range in between contains degrees of freedom that are accessible to magnetic fluctuations but not to velocities (Fig. 1). It is hardly surprising that these degrees of freedom are quickly occupied: the small-scale kinematic dynamo spreads magnetic energy over the subviscous range and piles it up at the resistive scale (e.g., Kulsrud & Anderson 1992). The key question then is what happens when the small-scale fields become sufficiently strong for the Lorentz force to react back on the flow.

We have identified three scale ranges, $L \gg l_0 \gg l_\nu \gg l_\eta$. To give a concrete example, let us give order-of-magnitude estimates for these scales in our Galaxy. The disk diameter is $L \sim 10^4$ pc; the supernova scale at which the turbulence is stirred is $l_0 \sim 10^2$ pc; the Reynolds number is $\mathrm{Re} \sim 10^5$, so the viscous scale is $l_\nu \sim 10^{-2}$ pc; the Prandtl number is $\mathrm{Pr}_m \sim 10^{14}$, so the resistive scale is 10^4 km, a tiny distance by galactic standards (note § 2.6). The associated timescales are the

period of galactic rotation $T \sim 10^8$ yr, the outer eddy turnover time $\tau_0 \sim 10^7$ yr, and the viscous eddy turnover time $\tau_\nu \sim 10^5$ yr. The mean-field dynamo theory gives a large-scale galactic field exponentiating in a rotation time T, while the timescale for the growth of the small-scale magnetic energy is τ_ν (Kulsrud & Anderson 1992). This illustrates our earlier point that the small-scale dynamo tends to be faster than the large-scale one.

1.3. *Simulating the Problem*

Simultaneously resolving all of these scales is not achievable in numerical simulations. Even if the large-scale object-specific features are forsaken and only isotropic homogeneous MHD turbulence with large Re and Pr_m is considered in a periodic box, it is still not possible to simulate both the hydrodynamic inertial and the magnetic subviscous ranges in the same box.

In the relevant numerical work so far, a popular course of action has been to run simulations with $Pr_m = 1$ (Meneguzzi et al. 1981; Kida et al. 1991; Kleva & Drake 1995; Miller et al. 1996; Cho & Vishniac 2000; Mininni et al. 2003; Haugen et al. 2003; our runs a1, a2, and A in § 5). This choice is usually motivated by the view of MHD turbulence as a cascade of interacting Alfvén wave packets (Kraichnan 1965; Goldreich & Sridhar 1995). In an Alfvén wave, velocity and magnetic fluctuations are equal, dissipation occurs at either viscous or resistive scale, whichever is larger, and whatever happens below that scale is usually not expected to affect the inertial range physics.

In fact, this theory only appears to work for *anisotropic* MHD turbulence with an externally imposed strong mean field (Maron & Goldreich 2001; Cho et al. 2002; Müller et al. 2003). In (forced) simulations with zero mean field, one invariably sees that velocity and magnetic field are not symmetric, their statistics are not the same, they do not dissipate at the same rate or at the same scale, and there is no scale-by-scale equipartition of kinetic and magnetic energies, as there should have been if the turbulence had been purely Alfvénic (see Maron et al. 2004 and § 5.1.2). The picture that does emerge is rather that of a very significant excess of magnetic energy at small scales and the magnetic energy spectra resembling the resistively dominated spectra of the small-scale large-Pr_m kinematic dynamo.

A natural step beyond $Pr_m = 1$ is to look at Prandtl numbers above, but of the order of, unity (Meneguzzi et al. 1981; Chou 2001; Brandenburg 2001; Maron & Blackman 2002; Maron et al. 2004; Archontis et al. 2003a, 2003b; Haugen et al. 2004; our run B in § 5) more or less in the hope that essential features of the $Pr_m \gg 1$ regime would be captured. This way, the inertial range might be resolvable, but the subviscous one (whose width is $\sim Pr_m^{1/2}$) is largely sacrificed. This approach is, to some extent, justified (see § 5). However, as the asymmetry between magnetic and velocity field becomes more pronounced with increasing Pr_m, one is faced with the realization that the $Pr_m \gtrsim 1$ case represents a nonasymptotic mixed state about which it is very hard to make any clear statements. We have pointed out in an earlier paper (Schekochihin et al. 2002b; see also § 5.2.3) that, in order for the effects of the scale separation between l_ν and l_η on the nonlinear physics to be fully present, one must have $Pr_m \gg Re^{1/2} \gg 1$. Astrophysical plasmas have no problem satisfying this condition, but numerically simulating this regime is not, as yet, possible.

We believe that the key feature of isotropic MHD turbulence is the scale separation that arises between velocities and magnetic fields. In an atrophied nonasymptotic form, this scale separation is discernible even at $Pr_m = 1$. Therefore, in most of this paper (with the exception of § 5), we follow Kinney et al. (2000) in choosing to resolve the subviscous range while sacrificing the inertial one. Namely, we set up our simulation in such a way that the forcing and viscous scales are comparable, while most of the available resolution is spent on the subviscous range.[5] At resolutions of 256^3, we can study Prandtl numbers up to 2500, which just barely allows us to make some statements about the asymptotic $Pr_m \gg 1$ limit. Furthermore, this approach allows us to study Pr_m dependence of our model, which is the only parameter scan that can at present be afforded. Some preliminary results obtained in the same setting (at lower resolutions) were published in Schekochihin et al. (2002d).

1.4. *Plan of the Paper*

Our numerical setup, equations, and the limitations of the model are discussed in more detail in § 2. Section 3 is devoted to a detailed study of the kinematic regime, which will be important for understanding further developments. Section 4 treats the nonlinear saturated state. Summaries are provided at the end of each of these two sections to help the reader identify the key points. In § 5 our understanding of the physics of the nonlinear dynamo with large Reynolds numbers is outlined and some tentative comparisons are made with the results of simulations with large Re and Pr_m of order unity. Section 6 discusses the scope of applicability of the large-Pr_m dynamo results and discusses directions of future work. An itemized summary of the main results and conclusions of the paper is given in § 7.

2. THE MODEL

2.1. *The Equations and the Code*

We consider the equations of incompressible MHD:

$$\frac{d}{dt}\boldsymbol{u} = \nu\Delta\boldsymbol{u} - \nabla p + \boldsymbol{B}\cdot\nabla\boldsymbol{B} + \boldsymbol{f}, \tag{1}$$

$$\frac{d}{dt}\boldsymbol{B} = \boldsymbol{B}\cdot\nabla\boldsymbol{u} + \eta\Delta\boldsymbol{B}, \tag{2}$$

---

[5] Note that another approach in which low Reynolds numbers are often considered is to study magnetic field growth and saturation in, and nonlinear modifications to, specific deterministic time-independent or time-periodic velocity fields with chaotic trajectories that are known to be dynamos in the kinematic limit (Childress & Gilbert 1995). The best-documented velocity fields of this sort are the ABC flows. The strategy then is to set up a forcing function that, in the absence of the magnetic field, would reproduce a given flow as a solution to the Navier-Stokes equation, to keep Re below the stability threshold of this solution (or to use some simplified model of the velocity equation that accomplishes the same), and to model the fast-dynamo regime by maximizing Pr_m (Galanti et al. 1992; Cattaneo et al. 1996; Maksymczuk & Gilbert 1999). This approach differs from ours in that the velocity field is not random in time, nor is it homogeneous in space, so such features as stagnation points of the flow, transport barriers, etc., may acquire a degree of importance that cannot be a feature of real turbulence. The redeeming advantage here is in being able to deal with a velocity field that, unlike in the case of real turbulence, does not constitute an unsolved problem by itself, so one has more control over the numerical experiment and some of the nonlinear effects may be more straightforward to detect. In some of these studies, Re is allowed to exceed the hydrodynamic stability threshold (Zienicke et al. 1998; Brummell et al. 2001), in which case the small-scale results are probably universal because of the usual physical expectation that the small-scale properties of turbulence are insensitive to the particular choice of large-scale forcing. Of course, in order for such a universality argument to work, Re must be sufficiently large, and resolving large Prandtl numbers is again problematic.

TABLE 1

Index of Runs

Run	ν	η	Pr_m	Grid	Re	$\langle u^2 \rangle$	$\langle B^2 \rangle$	$\langle B^4 \rangle/\langle B^2 \rangle^2$	$k_\lambda/2\pi$	$k_{rms}/2\pi$	$k_{B \times J}/2\pi$	$k_{B \cdot J}/2\pi$	$k_\parallel/2\pi$	$C_{K,B}$
S0-kin	5×10^{-2}	2×10^{-3}	25	64^3	2.0	0.39	Decays	3.9	1.1	3.4	2.2	0.77	0.52	-0.948
S1-kin	5×10^{-2}	10^{-3}	50	128^3	2.0	0.39	Grows	4.8	1.1	4.8	3.1	0.87	0.54	-0.971
S2-kin	5×10^{-2}	4×10^{-4}	125	128^3	2.0	0.39	Grows	6.2	1.1	7.1	4.6	1.0	0.69	-0.984
S3-kin	5×10^{-2}	2×10^{-4}	250	128^3	2.1	0.43	Grows	8.9	1.1	9.7	6.4	0.93	0.57	-0.991
S4-kin	5×10^{-2}	10^{-4}	500	256^3	2.0	0.41	Grows	9.4	1.1	13	8.8	1.1	0.55	-0.996
S1-sat	5×10^{-2}	10^{-3}	50	128^3	2.0	0.39	0.13	3.9	1.1	4.4	2.8	0.95	0.53	-0.967
S2-sat	5×10^{-2}	4×10^{-4}	125	128^3	1.9	0.36	0.20	3.7	1.1	5.8	3.6	1.2	0.55	-0.977
S3-sat	5×10^{-2}	2×10^{-4}	250	128^3	1.9	0.34	0.36	3.6	1.1	6.9	4.3	1.5	0.56	-0.981
S4-sat	5×10^{-2}	10^{-4}	500	256^3	1.9	0.36	0.33	4.1	1.1	8.9	5.5	1.8	0.57	-0.989
S5-sat[a]	5×10^{-2}	4×10^{-5}	1250	256^3	1.8	0.33	0.49	4.0	1.2	12	7.4	2.4	0.60	-0.992
S6-sat[b]	5×10^{-2}	2×10^{-5}	2500	256^3	1.8	0.32	0.43	4.1	1.2	15	9.6	3.0	0.77	-0.987
a0-kin	4×10^{-3}	4×10^{-3}	1	64^3	52	1.7	Decays	2.9	2.0	4.3	2.6	1.9	0.83	-0.841
a1-kin	2×10^{-3}	2×10^{-3}	1	128^3	100	1.7	Grows	3.2	2.6	6.9	4.3	2.7	1.2	-0.858
a2-kin[b]	10^{-3}	10^{-3}	1	128^3	210	1.7	Grows	3.5	3.6	10	6.3	3.9	1.8	-0.891
A-kin	5×10^{-4}	5×10^{-4}	1	256^3	450	2.0	Grows	6.3	5.0	18	12	7.0	3.1	-0.941
a1-sat	2×10^{-3}	2×10^{-3}	1	128^3	100	1.7	0.062	2.7	2.4	6.5	4.0	2.6	1.1	-0.862
a2-sat	10^{-3}	10^{-3}	1	128^3	200	1.6	0.20	2.8	2.7	7.9	4.4	3.5	1.0	-0.899
A-sat	5×10^{-4}	5×10^{-4}	1	256^3	390	1.5	0.25	3.2	3.3	11	6.0	4.2	1.0	-0.972
B-kin	2×10^{-3}	2×10^{-4}	10	256^3	100	1.6	Grows	8.5	2.6	19	12	4.1	1.3	-0.987
B-sat	2×10^{-3}	2×10^{-4}	10	256^3	80	0.98	0.42	3.3	2.3	12	6.8	3.8	0.66	-0.988

Notes.—In the labels assigned to the runs, "kin" means kinematic regime and "sat" means saturated state. See eq. (60) for the definition of Re, eqs. (13)–(17) for the definitions of the various k-values, and eq. (26) for the definition of $C_{K,B}$.

[a] In the kinematic regime, this run requires higher resolution.

[b] These runs are slightly underresolved.

where $d/dt = \partial_t + \boldsymbol{u} \cdot \nabla$ is the advective time derivative, $\boldsymbol{u}(t, \boldsymbol{x})$ is the velocity field, $\boldsymbol{B}(t, \boldsymbol{x})$ is the magnetic field, and $\boldsymbol{f}(t, \boldsymbol{x})$ is the body force. The pressure gradient ∇p (which includes magnetic pressure) is determined by the incompressibility condition $\nabla \cdot \boldsymbol{u} = 0$. We have normalized p and $\boldsymbol{B}$ by ρ and $(4\pi\rho)^{1/2}$, respectively, where $\rho = $ const is the plasma density.

Equations (1) and (2) are solved in a triply periodic box by the pseudospectral method (see code description in Maron & Goldreich 2001; Maron et al. 2004). The body force $\boldsymbol{f}$ is random, nonhelical, applied at the largest scales in the box ($k_0/2\pi = 1, 2$), and white in time (i.e., statistically independent at each time step):

$$\left\langle f^i(t, \boldsymbol{x}) f^j(t', \boldsymbol{x}') \right\rangle = \delta(t - t') \epsilon^{ij}(\boldsymbol{x} - \boldsymbol{x}'). \qquad (3)$$

For a white-noise forcing, the average injected power is fixed:

$$\frac{1}{2} \frac{d}{dt} \langle u^2 \rangle = -\nu \left\langle |\nabla \boldsymbol{u}|^2 \right\rangle - \langle \boldsymbol{BB} : \nabla \boldsymbol{u} \rangle + \epsilon, \qquad (4)$$

where $\epsilon = \langle \boldsymbol{u} \cdot \boldsymbol{f} \rangle = \frac{1}{2} \epsilon^{ii}(0) = $ const. The code units are based on box size 1 and injected power $\epsilon = 1$.

All runs are listed in Table 1. Runs S0–S6 are viscosity dominated (§ 2.3) with S4 being the main time-history run. Runs a1, a2, A, and B have larger Re but smaller Pr_m (see § 5).

2.2. Averaging

Mathematically speaking, all fields are random because the forcing is random. The system is isotropic and homogeneous in space, so all vector fields have zero mean and all points in the box are equally nonspecial. In theory, the angle brackets mean ensemble averages with respect to the forcing realizations and to the initial conditions. In practical measurements,

one can (based on the usual ergodic assumption) use volume and time averaging instead. In what follows, wherever time histories are plotted, only volume averaging is done, while for quantities averaged over the kinematic or saturated stages of our runs, both volume and time averaging are performed. Error bars show the mean square deviations of volume averages at particular times from the time-averaged values.

Averages in the kinematic regime are over 20 code time units (51 snapshots with time separation $\Delta t = 0.4$) for runs S0–S4, over 6 time units (31 snapshots, $\Delta t = 0.2$) for runs A and B, over 35 time units (71 snapshots, $\Delta t = 0.5$) for run a1, and over 15 time units (31 snapshots, $\Delta t = 0.5$) for run a2; averages in the saturated state are over 20 time units (51 snapshots, $\Delta t = 0.4$) for runs S1–S6, over 10 time units (51 snapshots, $\Delta t = 0.2$) for runs A and B, and over 30 time units (61 snapshots, $\Delta t = 0.5$) for runs a1 and a2. We have checked that increasing the averaging intervals does not alter the results. One code time unit roughly corresponds to the box crossing time (roughly the turnover time of the outer eddies).

2.3. The Viscosity-dominated Limit

As we can only adequately resolve either the inertial or the subviscous range, but not both, we choose to concentrate on the latter. In the runs reported in §§ 3 and 4 (but not in § 5), the viscosity is fixed at $\nu = 5 \times 10^{-2}$, which effectively leads to $l_0 \sim l_\nu$. The velocity field in these runs is not, strictly speaking, turbulent. It is still random in time because the external forcing is random, but it is smooth in space as a result of very strong viscous dissipation. Advection by a random but spatially smooth flow is known as the *Batchelor regime* (Batchelor 1959). From the point of view of realistic turbulence, such a flow is probably a fairly good model of the viscous-scale

eddies acting on the magnetic fluctuations in the subviscous range. In this interpretation, the external forcing f models the energy supply from the Kolmogorov cascade to the motions at the viscous scale.

We emphasize that, while f is white in time, the resulting velocity is not. In order to see this, let us consider equation (1) in the more drastic limit of $\mathrm{Re} \ll 1$, so the hydrodynamic non-linearity can be neglected, and let the Lorentz forces be negligible as well. Then the solution of equation (1) in k space is

$$\boldsymbol{u}(t,\, \boldsymbol{k}) = e^{-\nu k^2 t} \boldsymbol{u}(t=0,\, \boldsymbol{k}) + \int_0^t d\tau\, e^{-\nu k^2 \tau} \boldsymbol{f}(t-\tau,\, \boldsymbol{k}). \quad (5)$$

If f is Gaussian, so is $\boldsymbol{u}$, but $\boldsymbol{u}$ has a finite correlation time:

$$\left\langle u^i(t,\, \boldsymbol{k}) u^j(t',\, \boldsymbol{k}')\right\rangle = (2\pi)^3 \delta(\boldsymbol{k}+\boldsymbol{k}') \frac{1}{2\nu k^2} e^{-\nu k^2 |t-t'|} \epsilon^{ij}(\boldsymbol{k}), \quad (6)$$

where $\epsilon^{ij}(\boldsymbol{k}) = \int d^3 y\, e^{-i\boldsymbol{k}\cdot\boldsymbol{y}} \epsilon^{ij}(\boldsymbol{y})$ is the Fourier transform of the forcing correlation tensor (eq. [3]), and we took t, $t' \gg (\nu k_0^2)^{-1}$, k_0 being the forcing wavenumber. The velocity correlation time is then $\tau_c \sim (\nu k_0^2)^{-1}$. Equations (5) and (6) are strictly valid only if $\nu k^2 \gg k u_k$ for all k. In our simulations, we chose ν so that $\nu k_0^2 \sim k_0 u_{k_0}$ ($\Leftrightarrow k_\nu \sim k_0$), i.e., just large enough for the inertial range to collapse. The obvious estimate for the velocity correlation time in this regime is $\tau_c \sim (k_0 u_{k_0})^{-1}$. Given the limitation of not having an inertial range, we believe this to be a sensible way of modeling turbulent motions.

Explicit contact can be made between the viscosity-dominated model and the analytical results from the kinematic dynamo theory. One of the very few time-dependent random flows for which kinematic dynamo is exactly solvable is a Gaussian white velocity field $v(t,\, \boldsymbol{x})$:

$$\left\langle v^i(t,\, \boldsymbol{x}) v^j(t',\, \boldsymbol{x}')\right\rangle = \delta(t-t') \kappa^{ij}(\boldsymbol{x}-\boldsymbol{x}'). \quad (7)$$

This model was introduced by Kazantsev (1968) and, in the context of passive scalar advection, independently by Kraichnan (1968). For the $\mathrm{Pr}_m \gg 1$ problems, many quantities of interest then turn out to depend only on the first few coefficients in the Taylor expansion of the velocity correlation tensor:

$$\kappa^{ij}(\boldsymbol{y}) = \kappa_0 \delta^{ij} - \frac{1}{2}\kappa_2\left(y^2 \delta^{ij} - \frac{1}{2}y^i y^j\right)$$
$$+ \frac{1}{4!}\kappa_4 y^2\left(y^2 \delta^{ij} - \frac{2}{3}y^i y^j\right) + \dots . \quad (8)$$

Increasing ν in equations (5) and (6) above the value at which $k_\nu \sim k_0$ is equivalent to decreasing the correlation time of the flow. Thus, the velocity field in the viscosity-dominated model reduces to the Kazantsev velocity in the limit $\nu \to \infty$, provided that the force is rescaled to keep the integral of the time correlation function constant: $\epsilon^{ij}(\boldsymbol{k}) = \nu^2 k^4 \kappa^{ij}(\boldsymbol{k})$ (i.e., $\boldsymbol{f} = -\nu \Delta v$). Since we owe much of our understanding of the kinematic dynamo to the Kazantsev model (e.g., Kazantsev 1968; Artamonova & Sokoloff 1986; Kulsrud & Anderson 1992; Gruzinov et al. 1996; Chertkov et al. 1999; Schekochihin et al. 2002b, 2002c, 2004b), it is convenient to be able to consider the nonlinear problem as a well-defined extension of it.

2.4. Incompressibility

We use incompressible MHD even though most astrophysical flows are not incompressible at large scales. For example, the supernova forcing of the galactic turbulence produces sonic velocities at the outer scale. However, motions at smaller scales are subsonic and mostly vortical and incompressible (e.g., Boldyrev et al. 2002; Porter et al. 2002; Balsara et al. 2004). As we are interested in the small-scale dynamo, which is driven by the smallest eddies, the incompressibility assumption is, therefore, reasonable. This view is further supported by the satisfactory outcome of a number of comparisons (carried out by N. E. Haugen 2003, private communication) between our simulations (§ 5) and the simulations of Haugen et al. (2003, 2004), who used a compressible grid code.

2.5. Helicity

Our simulations are nonhelical in the sense that the net kinetic helicity is zero, $\langle \boldsymbol{u}\cdot(\nabla\times\boldsymbol{u})\rangle = 0$ (helicity *fluctuations* are allowed). The net helicity of the flow can be controlled via the helical component of the external forcing (Maron & Blackman 2002). Helicity is usually considered important because it is present in some of the astrophysical objects of interest. However, net helicity is a large-scale feature associated with overall rotation. Its effects should only be felt at timescales comparable to the rotation timescale, which is usually much longer than the turnover time of the turbulent eddies. Furthermore, helicity undergoes an inverse cascade from small scales to the largest scale in the box (Frisch et al. 1975; Pouquet et al. 1976). While net helicity is crucial for the generation of the box-scale magnetic field (essentially the mean field), the above considerations suggest that it probably does not play a significant role in the small-scale dynamo. In the viscosity-dominated simulations reported in §§ 3 and 4, the box scale is the viscous scale and the external forcing models energy influx from larger scales, so allowing helical forcing is not a physically sensible choice. In the large-Re runs of § 5, the effect of helicity would be interesting to study, but it would introduce another scale separation into the problem (between the box size and the forcing scale) and, therefore, require dramatic increases in numerical resolution.

2.6. Plasma Dissipation Processes

Our choice of Laplacian diffusion operators to describe viscous and resistive cutoffs is only a very crude model of the actual dissipation processes in astrophysical plasmas.

In a fully ionized plasma, ions become magnetized already at relatively low magnetic field strengths and the hydrodynamic viscosity must be replaced by a more general tensor viscosity (Braginskii 1965; see also Montgomery 1992), which is locally anisotropic and very inefficient at damping velocity gradients perpendicular to the magnetic field: the perpendicular components of the viscosity tensor vanish in the limit of zero Larmor radius (the magnetic diffusivity also becomes anisotropic, but the difference between its perpendicular and parallel components is only a factor of ~ 2). This can alter the physics at subviscous scales (Malyshkin & Kulsrud 2002; Balbus 2004).

In partially ionized plasmas (e.g., in the interstellar medium), viscous dissipation is controlled by neutral species and can be assumed isotropic. However, in the presence of neutrals, ambipolar damping might enhance magnetic field diffusion (e.g., Zweibel 1988, 2002; Kulsrud & Anderson 1992; Proctor & Zweibel 1992; Brandenburg & Zweibel 1994; Brandenburg & Subramanian 2000; Kim & Diamond 2002).

Finally, since the mean free path in astrophysical plasmas is often much larger than the scale associated with the Spitzer
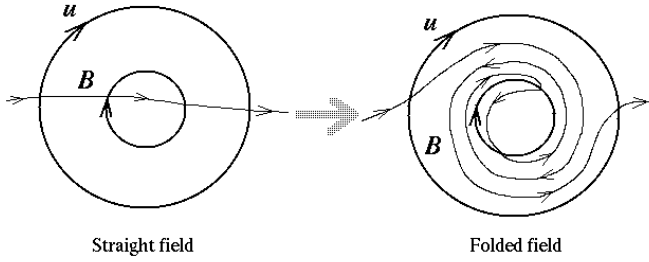
FIG. 2.—Stretching and folding of field lines by turbulent eddies.

FIG. 3.—Exponential growth and saturation of the magnetic energy. Full time history is only shown for run S4. See Table 1 for the index of runs.

resistivity, the magnetic field diffusion could be superseded by kinetic damping effects not contained in the MHD description (Foote & Kulsrud 1979; Kulsrud et al. 1997b).

These and other effects outside the MHD paradigm can be important. However, in this paper we have opted to study the problem in the simplest available formulation: that provided by equations (1) and (2). We believe that this minimal model already contains the essentials of the small-scale dynamo physics.

3. THE KINEMATIC DYNAMO

The kinematic dynamo is a natural starting point for a numerical experiment. What we learn about magnetic fields in the kinematic limit will motivate our investigation of the nonlinear regime. This is a rather detailed study, so a busy reader anxious to get to the nonlinear matters may skip to the short summary in § 3.5 and on to § 4.

The small-scale turbulent dynamo is caused by the random stretching of the (nearly) frozen-in field lines by the ambient random flow. Stretching leads to exponential growth of the field strength (Batchelor 1950). The growth rate $\gamma \sim \nabla u$ is then naturally of the order of the inverse eddy turnover time. In the case of Kolmogorov turbulence, it is the turnover time τ_ν of the smallest (viscous scale) eddies because they are the fastest (see § 5.1.1). For the magnetic fields at subviscous scales, the action of these eddies is roughly equivalent to the application of a random linear shear. Without diffusion ($\eta = 0$), stretching is not opposed by any dissipation mechanism. However, stretching is necessarily accompanied by the refinement of the field scale (Fig. 2), which proceeds exponentially fast in time and also at the eddy turnover rate. Thus, the field scale eventually becomes comparable to the diffusion (resistive) scale, bringing an end to the diffusion-free evolution. The characteristic time during which diffusion-free considerations apply is $t \sim \gamma^{-1} \ln (l_\nu/l_\eta) \sim \gamma^{-1} \ln (\mathrm{Pr}_m^{1/2})$, assuming that the initial field varies at the velocity scales.

Once diffusion enters the picture, it will (partially) offset the effect of random stretching (see § 3.3). If magnetic energy continues to grow exponentially in this regime with a growth rate that does not vanish as $\eta \rightarrow +0$, the dynamo is called *fast* (Vainshtein & Zel'dovich 1972). Whether any given flow is a fast dynamo is a problem that very rarely has an analytical solution (Childress & Gilbert 1995). In practice, since the advent of numerical simulations, turbulent flows have more often than not been found to support fast dynamo action (see references in § 1.3 and discussion in § 6.1). In what follows, we shall see that magnetic fluctuations that result from this dynamo have a distinctive structure (see §§ 3.2 and 3.3).

In all our runs, the initial magnetic field had a spectrum concentrated at velocity scales so that both diffusion-free and diffusive regimes of the kinematic dynamo are realized. As a result of resolution constraints, the diffusion-free stage is never longer than 2 time u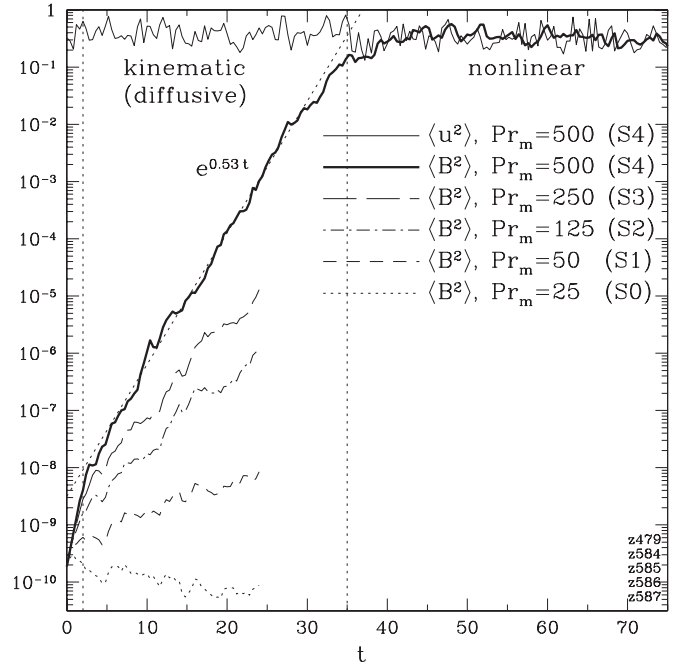nits. The diffusive stage is quite long, so it is possible to extract statistical information by averaging over 20 time units. The magnetic energy grows exponentially from the initial value of $\sim 10^{-10}$ to saturated values of order unity (Fig. 3).

In this section we study the properties of the growing field. We concentrate on three main questions. First, what is its energy spectrum? This is considered in § 3.1. Second, what does the field "look" like? The field structure is studied in § 3.2. Third, how does it fill the volume? This question is treated in § 3.4 in terms of the field strength statistics. Section 3.3 is a qualitative interlude discussing the physical reasons for the existence of the small-scale dynamo.

3.1. *The Magnetic Energy Spectrum and Growth Rate*

The evolution of the angle-integrated magnetic energy spectrum, $M(k) = \frac{1}{2} \int d\Omega_k \, k^2 \langle |\boldsymbol{B}(\boldsymbol{k})|^2 \rangle$, in the large-$\mathrm{Pr}_m$ regime is the best-understood part of the kinematic dynamo physics. For the Kazantsev velocity model, $M(k)$ can be shown to satisfy a closed integrodifferential equation, which, for $k \gg k_\nu$, reduces to a simple Fokker-Planck equation (Kazantsev 1968; Vainshtein 1972, 1980, 1982; Kulsrud & Anderson 1992; Gruzinov et al. 1996; Schekochihin et al. 2002a)

$$\partial_t M = \frac{\bar{\gamma}}{5} \frac{\partial}{\partial k} \left(k^2 \frac{\partial}{\partial k} M - 4kM \right) + 2\bar{\gamma}M - 2\eta k^2 M, \quad (9)$$

where $\bar{\gamma} = (5/4)\kappa_2 \sim \nabla u$ is comparable to the inverse turnover time of the viscous eddies. Integrating equation (9) gives

$$\partial_t \langle B^2 \rangle = 2\bar{\gamma} \langle B^2 \rangle - 2\eta k_{\mathrm{rms}}^2 \langle B^2 \rangle, \quad (10)$$

so $\bar{\gamma}$ is the growth rate of the rms magnetic field in the absence of diffusion (the stretching rate). Without diffusion, equation (9) describes a spreading lognormal profile with a peak moving exponentially fast toward ever larger wavenumbers, $k_{\mathrm{peak}} \propto \exp (\frac{3}{5} \bar{\gamma} t)$, the amplitude of each mode growing exponentially at

the rate $\frac{3}{4}\bar{\gamma}$, and the dispersion of $\ln k$ increasing linearly in time as $\frac{4}{5}\bar{\gamma}t$.

Once the resistive scale is reached and diffusion becomes important, further increase of k stops. The spectrum is a solution of an eigenvalue problem for equation (9) with $M(k) \propto \exp(\lambda\bar{\gamma}t)$. Here $\lambda < 2$ because diffusion dissipates some of the dynamo-generated energy: equation (10) is an expression of this competition between stretching and diffusion. If λ tends to a positive η-independent constant in the limit $\eta \rightarrow +0$, stretching wins and the dynamo is fast. In order to solve this eigenvalue problem, we must specify the boundary condition at small k. In principle, this boundary condition can be determined only by solving the original integrodifferential equation of which equation (9) is an asymptotic form for $k \gg k_\nu$. This integrodifferential equation contains the velocity statistics at all scales and cannot be solved in a general and model-independent way. However, the eigenvalues are not very sensitive to the boundary condition: a natural choice is to impose a zero-flux constraint at some infrared cutoff k_* (Schekochihin et al. 2002b), but a number of other reasonable options give the same solution,[6]

$$M(k) \simeq (\text{const})e^{\lambda\bar{\gamma}t}k^{3/2}K_0(k/k_\eta), \qquad (11)$$

$$\lambda \simeq \frac{3}{4} - \frac{\pi^2}{5\left[\ln(k_\eta/k_*)\right]^2}, \qquad (12)$$

where $k_\eta = (\bar{\gamma}/10\eta)^{1/2}$ and K_0 is the Macdonald function. In the limit $\eta \rightarrow +0$, we get $\lambda \rightarrow \frac{3}{4}$, a fast dynamo. Note that $\frac{3}{4}\bar{\gamma}$ is the rate at which individual k-space modes grow as a result of random stretching, so the effect of diffusion is simply to stop the magnetic energy from spreading to ever larger k (Kulsrud & Anderson 1992; Schekochihin et al. 2002a).

The numerical results broadly confirm this theoretical picture. In Figure 3 we show the evolution of the magnetic energy for several values of Pr_m. The growth is exponential in time, and, for $\text{Pr}_m = 500$, the growth rate after resistive scales are reached ($t \gtrsim 2$) is reduced compared to the diffusion-free regime by a factor that is actually quite close to $\frac{3}{8}$, predicted by the Kazantsev model.[7] The growth rate at smaller values of Pr_m is smaller, as a result of nonnegligible reduction by diffusion as suggested by the logarithmic correction in equation (12).

The Prandtl number must exceed a certain critical value $\text{Pr}_{m,c}$ in order for the dynamo to be possible. Indeed, in equation (12), for $k_* \sim k_\nu$, we have $k_\eta/k_* \sim \text{Pr}_m^{1/2}$ and setting $\lambda = 0$ gives a rough estimate of the threshold below which the dynamo is resistively suppressed: $\text{Pr}_{m,c} \sim 26$. In our runs, we

have found growth at $\text{Pr}_m = 50$ and decay at $\text{Pr}_m = 25$, so $\text{Pr}_{m,c} \in (25, 50)$. Note that both the Kazantsev velocity with smooth correlation tensor given by equation (8) and the velocity field in our simulations are single-scale flows with $\text{Re} \sim 1$, so $\text{Pr}_{m,c}$ simply corresponds to the critical magnetic Reynolds number $\text{Re}_{m,c} = \text{Re} \, \text{Pr}_{m,c}$. Since for our viscosity-dominated runs $\text{Re} \simeq 2$, we have $\text{Re}_{m,c} \in (50, 100)$.

The diffusion-free spreading of the magnetic energy toward resistive scales and the subsequent self-similar growth of the spectrum with a peak at the resistive scale (eq. [11]) are manifest in Figure 4a. The $k^{3/2}$ scaling appears to be correct (Fig. 4b), although resolving a broader scaling range is necessary for definite corroboration. The occasional strong disruptions of the self-similar growth (Fig. 4a) are discussed at the end of § 3.4.3.

3.2. The Folded Structure

The small-scale magnetic fields produced by the dynamo are not, in fact, completely devoid of large-scale coherence. The smallness of their characteristic scale is due primarily to the rapid (in space) field reversals transverse to the local field direction. Along themselves, the fields vary at scales comparable to the size of the eddies. This folded structure is schematically illustrated in Figure 2 and is evident in field visualizations (Fig. 5).

There are many ways to diagnose the folded structure. Ott and coworkers studied the field reversals in map dynamos in terms of magnetic flux cancellation (see review by Ott 1998 and numerical results by Cattaneo et al. 1995). Chertkov et al. (1999) considered two-point correlation functions of the magnetic field and found large-scale correlations along the field and short-scale correlations across. The simplest approach is, in fact, to measure average characteristic scales at which the field varies in the directions perpendicular and parallel to itself. In two dimensions, this was done by Kinney et al. (2000). In three dimensions, the characteristic scales are studied in § 3.2.1. A more detailed description of the field's "statistical geometry" is provided by the distribution of the field-line curvature (§ 3.2.4) and by its relation to the field strength (§ 3.2.3). The advantage of this approach is that curvature is a local quantity, so we only have to look at one-point statistics. It is also directly involved in the Lorentz tension force (eq. [27]), thus providing information about the onset of the nonlinear back-reaction (§ 4). An analytical theory based on the Kazantsev model was developed in an earlier paper (Schekochihin et al. 2002c). The numerical study below is motivated by the quantitative predictions made there.

3.2.1. Characteristic Scales

We define the characteristic parallel wavenumber of the field

$$k_\parallel = \left(\frac{\langle|\boldsymbol{B}\cdot\nabla\boldsymbol{B}|^2\rangle}{\langle B^4\rangle}\right)^{1/2} \qquad (13)$$

and its characteristic perpendicular wavenumber

$$k_{\boldsymbol{B}\times\boldsymbol{J}} = \left(\frac{\langle|\boldsymbol{B}\times\boldsymbol{J}|^2\rangle}{\langle B^4\rangle}\right)^{1/2}, \qquad (14)$$

---

[6] These include, e.g., requiring that the magnetic field second-order correlation function decay exponentially at large distances (Artamonova & Sokoloff 1986; Subramanian 1997) or setting $M(k_*) = 0$ (Schekochihin et al. 2002a). Kulsrud & Anderson (1992) solved the integrodifferential equation for the spectrum numerically, using a Kolmogorov spectrum for velocity, and also obtained $\lambda = \frac{3}{4}$. See also Gruzinov et al. (1996) for yet another argument leading to the same result.

[7] We hesitate to claim that this is a corroboration of the specific number that obtains in the Kazantsev model rather than a mere coincidence. The Kazantsev velocity is δ-correlated in time, which cannot be a good quantitative description of the velocity field in our simulations (see § 2.3). It is well known that finite correlation time effects can result in first-order corrections to the dynamo growth rate (Chandran 1997; Kinney et al. 2000; Schekochihin & Kulsrud 2001; Chou 2001; Kleeorin et al. 2002). While the scalings in the Kazantsev model may be universal (e.g., the power tail of the curvature pdf; § 3.2), the values of growth rates can only a priori be considered as qualitative predictions.
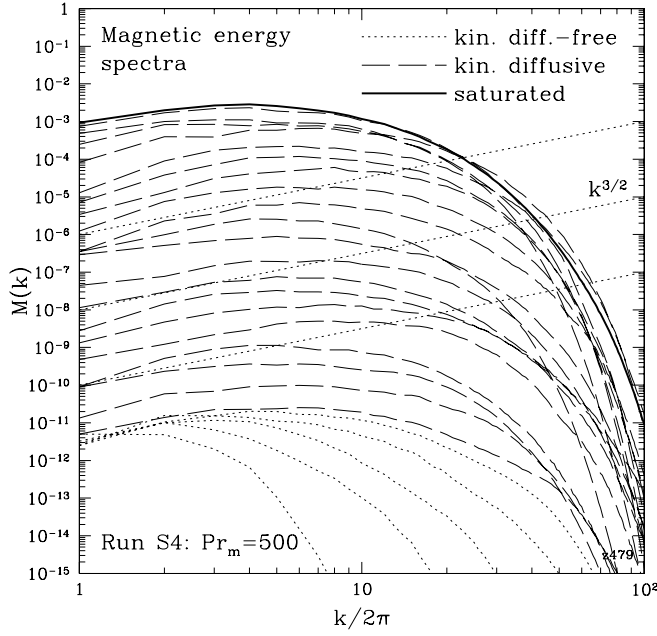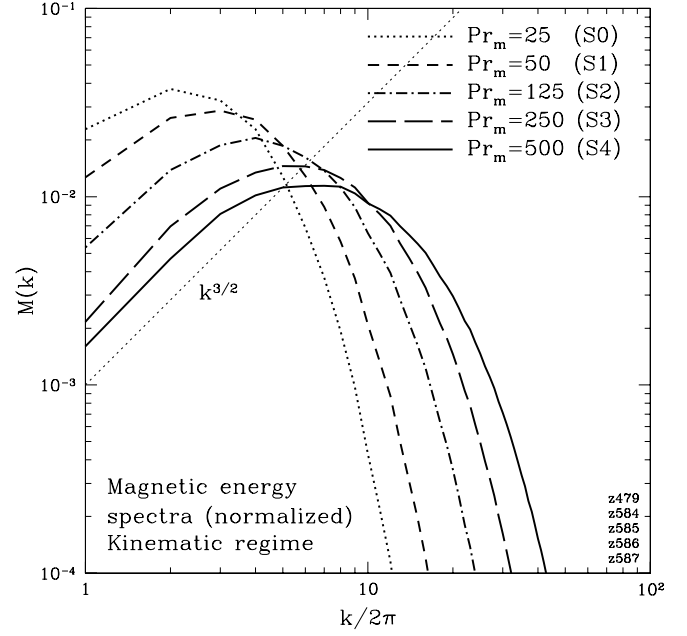
FIG. 4a

FIG. 4b

FIG. 4.—(a) Evolution of the magnetic energy spectrum for run S4. The spectra for the diffusion-free regime ($0 \le t < 2$) are given at time intervals of $\Delta t = 0.4$. The subsequent evolution ($2 \le t \le 40$) is represented by spectra at time intervals $\Delta t = 2$. (b) Magnetic energy spectra (normalized by the total magnetic energy and averaged) during the kinematic stage. Note that for run S0 dynamo is resistively suppressed.

where $\boldsymbol{J} = \nabla \times \boldsymbol{B}$. The overall field variation is measured by the rms wavenumber

$$k_{\rm rms} = \left[\frac{1}{\langle B^2 \rangle / 2} \int_0^\infty dk\, k^2 M(k) \right]^{1/2} = \left(\frac{\langle |\nabla \boldsymbol{B}|^2 \rangle}{\langle B^2 \rangle} \right)^{1/2}. \quad (15)$$
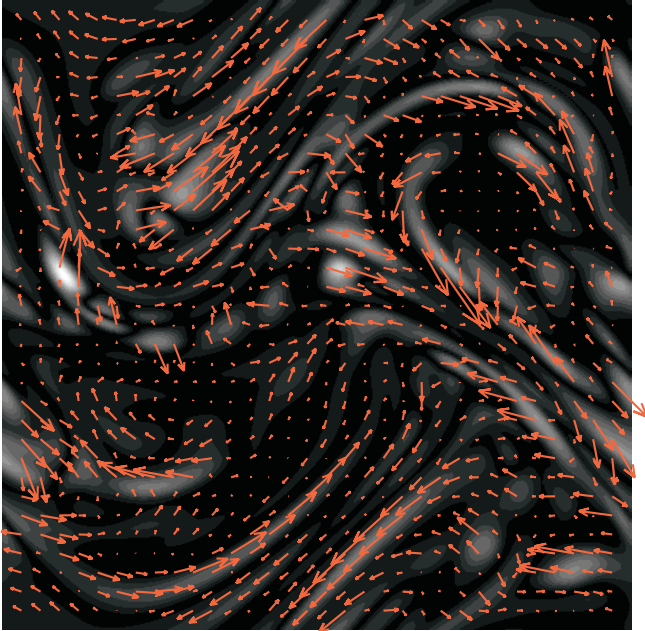
FIG. 5.—Cross section of the magnetic field strength (*gray scale*) and in-plane field direction (*red arrows*) at $t = 20$ during the kinematic stage of run S4. Lighter regions correspond to stronger fields. Note that what appears to be strong-field "clumps" are, in fact, cross sections of folds transverse to the page.

While both $k_{\boldsymbol{B} \times \boldsymbol{J}}$ and $k_{\rm rms}$ grow exponentially during the diffusion-free regime and saturate at values that scale as $k_\eta \sim k_\nu \Pr_m^{1/2}$ (cf. Brummell et al. 2001), the parallel wavenumber $k_\parallel$ remains approximately constant and comparable to k_ν (Schekochihin et al. 2002c; see also Fig. 6). For comparison, we also plot (Fig. 6) the rms wavenumber of the velocity field,

$$k_\lambda = \left[\frac{1}{\langle u^2 \rangle / 2} \int_0^\infty dk\, k^2 E(k) \right]^{1/2} = \left(\frac{\langle |\nabla \boldsymbol{u}|^2 \rangle}{\langle u^2 \rangle} \right)^{1/2} = \frac{\sqrt{5}}{\lambda}, \quad (16)$$

where $E(k)$ is the angle-integrated kinetic energy spectrum and λ is the Taylor microscale of the flow defined in the standard way (Frisch 1995). In Kolmogorov turbulence, $\lambda \sim \mathrm{Re}^{-1/2} l_0 \sim \mathrm{Re}^{1/4} l_\nu$, so $k_\lambda \sim \mathrm{Re}^{-1/4} k_\nu$.

In order to estimate the degree of misalignment between the direction-reversing fields, it is instructive to look at a characteristic wavenumber of field variation in the direction orthogonal to both $\boldsymbol{B}$ and $\boldsymbol{B} \times \boldsymbol{J}$:

$$k_{\boldsymbol{B} \cdot \boldsymbol{J}} = \left(\frac{\langle |\boldsymbol{B} \cdot \boldsymbol{J}|^2 \rangle}{\langle B^4 \rangle} \right)^{1/2}. \quad (17)$$

Figure 6 and Table 1 show that $k_{\boldsymbol{B} \cdot \boldsymbol{J}} \sim k_\nu$ and does not increase with $\Pr_m$ in the kinematic regime. Thus, the reversing straight fields are fairly well aligned and the flux surfaces are sheets.

3.2.2. Fourth-Order Spectra

One can probe further into the behavior of the quantities $\boldsymbol{B} \cdot \nabla \boldsymbol{B}$, $\boldsymbol{B} \times \boldsymbol{J}$, and $\boldsymbol{B} \cdot \boldsymbol{J}$ by looking at their spectra. All these
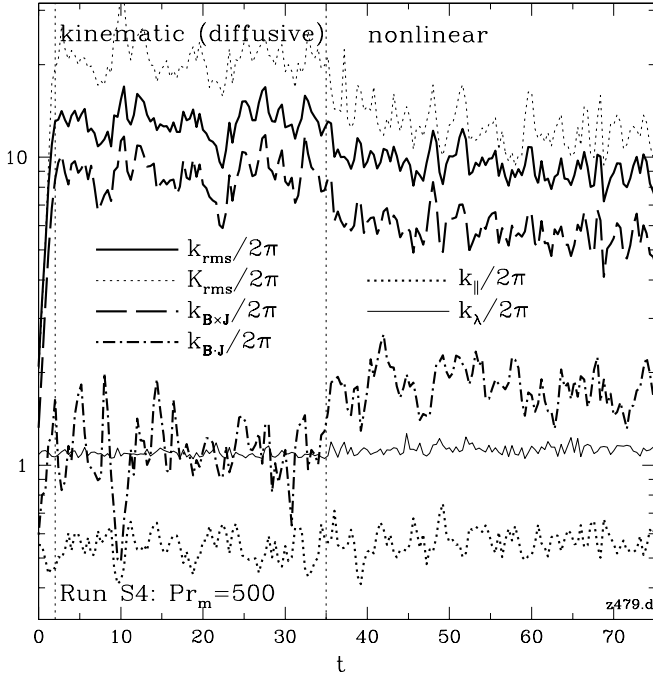
Fig. 6a

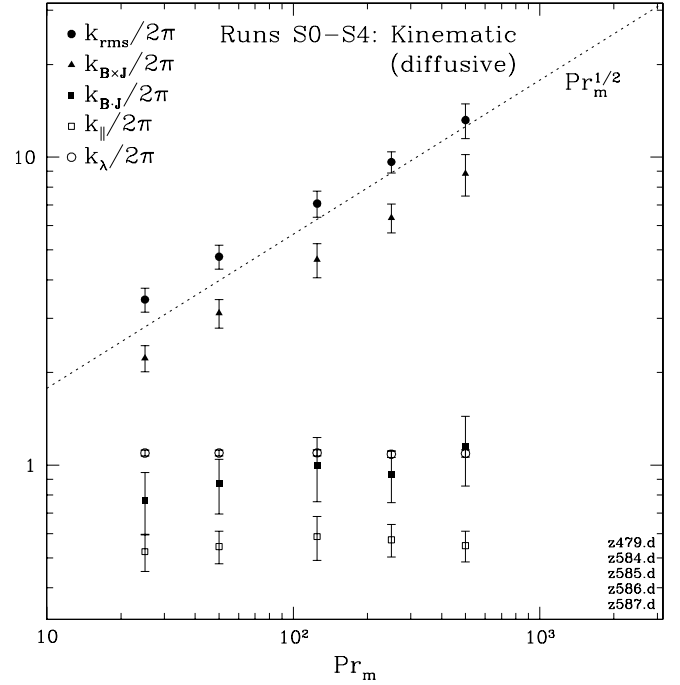Fig. 6b

Fig. 6.—(a) Evolution of characteristic wavenumbers (defined in § 3.2.1) and of $K_{rms} = \langle |\hat{\boldsymbol{b}} \cdot \nabla \hat{\boldsymbol{b}}|^2 \rangle^{1/2}$ for run S4. (b) Averaged values of the same wavenumbers vs. Pr_m during the kinematic stage of runs S0–S4. Note that for run S0 dynamo is resistively suppressed. The values plotted are listed in Table 1.

spectra are, in fact, controlled by the spectrum of B^2, which turns out to be flat. Define angle-averaged spectra

$$M_4(k) = \frac{1}{2} \int d\Omega_{\boldsymbol{k}} \, k^2 \left\langle |(B^2)(\boldsymbol{k})|^2 \right\rangle, \qquad (18)$$

$$M_{\boldsymbol{B}\times\boldsymbol{J}}(k) = \frac{1}{2} \int d\Omega_{\boldsymbol{k}} \, k^2 \left\langle |(\boldsymbol{B}\times\boldsymbol{J})(\boldsymbol{k})|^2 \right\rangle, \qquad (19)$$

$$M_{\boldsymbol{B}\cdot\boldsymbol{J}}(k) = \frac{1}{2} \int d\Omega_{\boldsymbol{k}} \, k^2 \left\langle |(\boldsymbol{B}\cdot\boldsymbol{J})(\boldsymbol{k})|^2 \right\rangle, \qquad (20)$$

$$T(k) = \frac{1}{2} \int d\Omega_{\boldsymbol{k}} \, k^2 \left\langle |(\boldsymbol{B}\cdot\nabla\boldsymbol{B})(\boldsymbol{k})|^2 \right\rangle. \qquad (21)$$

We find (Fig. 7) that all these spectra grow self-similarly and

$$M_4(k) \sim k^0, \quad M_{\boldsymbol{B}\times\boldsymbol{J}}(k) \simeq \tfrac{1}{4} k^2 M_4(k), \qquad (22)$$

$$M_{\boldsymbol{B}\cdot\boldsymbol{J}}(k) \simeq k_{\boldsymbol{B}\cdot\boldsymbol{J}}^2 M_4(k), \quad T(k) \simeq k_{\parallel}^2 M_4(k), \qquad (23)$$

with $k_{\parallel}$ and $k_{\boldsymbol{B}\cdot\boldsymbol{J}}$ defined by equations (13) and (17).

This simple behavior is due to the folded structure. If the magnetic field variation is dominated by direction reversals, then, for $k_\nu \ll k \ll k_\eta$, the main contribution to the integral

$$\left\langle |(B^2)(\boldsymbol{k})|^2 \right\rangle = \int d^3 k' \int d^3 k'' \left\langle \boldsymbol{B}(\boldsymbol{k}') \cdot \boldsymbol{B}(\boldsymbol{k} - \boldsymbol{k}') \right.$$
$$\left. \times \, \boldsymbol{B}(\boldsymbol{k}'') \cdot \boldsymbol{B}(-\boldsymbol{k} - \boldsymbol{k}'') \right\rangle \qquad (24)$$

is from k', $k'' \sim k_\eta$ with the proviso that $\boldsymbol{k}'$, $\boldsymbol{k}''$, and $\boldsymbol{k}$ are all in the direction of the reversal (i.e., transverse to the flux sheet). Expanding in $\boldsymbol{k}$, we get to zeroth order, $\langle |(B^2)(\boldsymbol{k})|^2 \rangle \simeq \langle B^4 \rangle \propto k^0$. Since the spectrum is essentially one-dimensional (peaked

for $\boldsymbol{k}$ transverse to the flux sheet), we get $M_4(k) \sim k^0$. The rest of the fourth-order spectra can be worked out in the same way and equations (22) and (23) are readily obtained.

These results prove useful in §§ 4.2 and 5.3.4.

3.2.3. Magnetic Field Strength and Curvature

The field geometry can be studied in a more detailed way in terms of the curvature $\boldsymbol{K} = \hat{\boldsymbol{b}} \cdot \nabla \hat{\boldsymbol{b}}$ of the field lines ($\hat{\boldsymbol{b}} = \boldsymbol{B}/B$). $K = |\boldsymbol{K}|$ satisfies (cf. Drummond & Münch 1991)

$$\frac{d}{dt} K = (\hat{\boldsymbol{n}}\hat{\boldsymbol{n}}:\nabla\boldsymbol{u} - 2\hat{\boldsymbol{b}}\hat{\boldsymbol{b}}:\nabla\boldsymbol{u})K + \hat{\boldsymbol{b}}\hat{\boldsymbol{b}}:(\nabla\nabla\boldsymbol{u})\cdot\hat{\boldsymbol{n}}, \quad (25)$$

where $\hat{\boldsymbol{n}} = \boldsymbol{K}/K$ and resistive terms have been dropped. Equation (25) is a straightforward consequence of equation (2). A standard kinematic calculation of the rms curvature, $K_{rms} = \langle K^2 \rangle^{1/2}$, shows that it grows exponentially in the diffusion-free regime (Malyshkin 2001; Schekochihin et al. 2002c; see also Fig. 6). Since curvature is an inverse scale, it is clear that in the diffusive regime, K_{rms} must saturate at some Pr_m-dependent value.

The growth of K_{rms} does not contradict our previous claim that magnetic field lines are straight up to the flow scale. As the field is stretched and folded, it is organized in long thin structures (folds) where it is only significantly curved in the bends (turning points). The flow stretches the straight segments of the field, while the curved fields in the bends remain weak (this is simply a consequence of flux and volume conservation; see Schekochihin et al. 2002c, 2002d). Thus, there is anticorrelation between the field-line curvature and the field strength.

The most straightforward statistical measure of this anticorrelation is the correlation coefficient defined as follows:

$$C_{K,B} = \frac{\langle K^2 B^2 \rangle - \langle K^2 \rangle \langle B^2 \rangle}{\langle K^2 \rangle \langle B^2 \rangle}. \qquad (26)$$
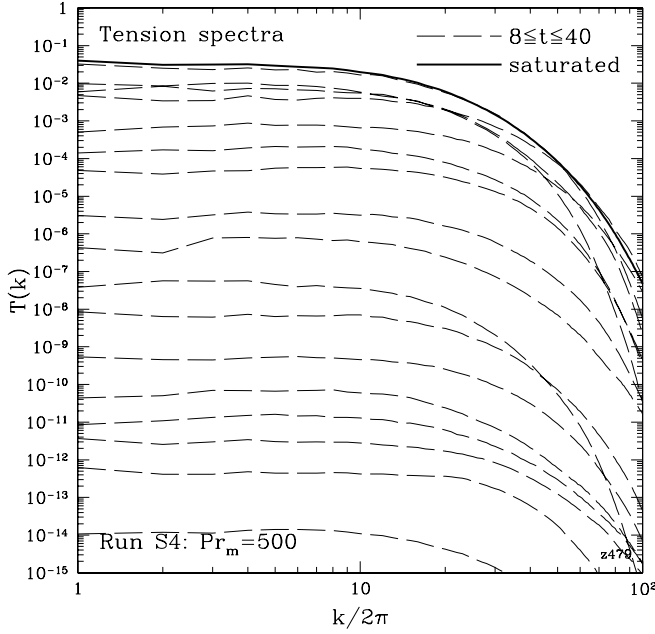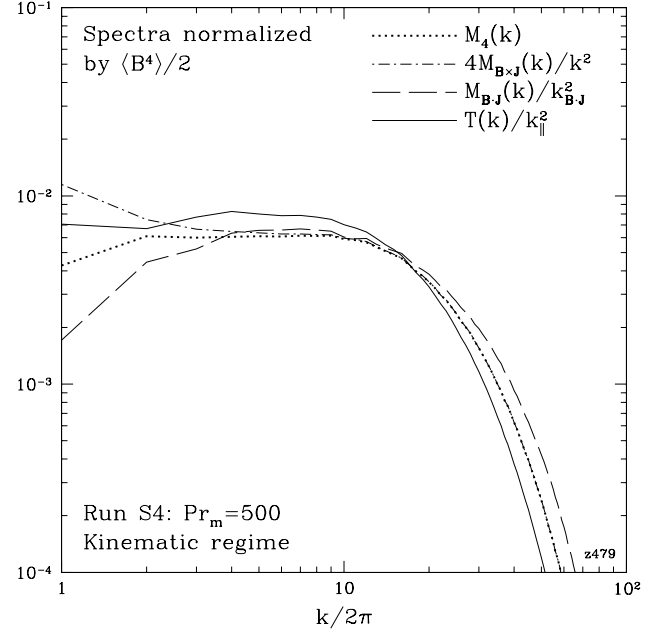
Fig. 7a

Fig. 7b

Fig. 7.—(a) Tension spectra for run S4 for $8 \leq t \leq 40$ at intervals $\Delta t = 2$ and in the saturated state. (b) Fourth-order spectra defined in eqs. (18)–(21) (normalized by $\langle B^4 \rangle/2$ and averaged) during the kinematic stage of run S4. The evolution of all these spectra is analogous to that of $T(k)$ shown in (a).

In all runs, it is found to be within 6% of its minimum possible value of -1 (Table 1). Furthermore, we notice that the mean square tension force (see eq. [1]) is

$$\left\langle |\boldsymbol{B} \cdot \nabla \boldsymbol{B}|^2 \right\rangle = \left\langle B^4 K^2 \right\rangle + \left\langle B^4 |\nabla_\parallel B/B|^2 \right\rangle, \qquad (27)$$

so the fact that $K_{\mathrm{rms}}^2 \sim \langle |\boldsymbol{B} \cdot \nabla \boldsymbol{B}|^2/B^4 \rangle$ is large (and grows with Pr_m) while $k_\parallel^2 = \langle |\boldsymbol{B} \cdot \nabla \boldsymbol{B}|^2 \rangle/\langle B^4 \rangle \sim k_\nu^2$ also indicates that the curvature in the regions of growing field remains comparable to the inverse scale of the flow.[8]

Let us give an illustration of the anticorrelation between B and K for a typical snapshot of the field. In Schekochihin et al. (2002c), we noted that this anticorrelation was manifest in cross sections of field strength and curvature. Figure 5 does, indeed, show that field lines are straight (and direction reversing) in the areas of strong field. The same point can be made by scatter plots of B versus K during the kinematic stage of our run S4 (Fig. 8). Since the distributions of both magnetic field (§ 3.4) and curvature (§ 3.2.4) are intermittent, the scatter is quite wide. It is clear, however, that magnetic fields with $B \gtrsim B_{\mathrm{rms}}$ have curvatures well below K_{rms} while the fields with curvatures $K \gtrsim K_{\mathrm{rms}}$ are quite weak.

If we consider equation (25) together with the evolution equation for the magnetic field strength,

$$\frac{d}{dt} B = \left(\hat{\boldsymbol{b}}\hat{\boldsymbol{b}} : \nabla \boldsymbol{u} \right) B + \eta \Delta B - \eta |\nabla \hat{\boldsymbol{b}}|^2 B, \qquad (28)$$

and drop both the resistive terms and the second derivatives of the velocity field (bending terms), we might observe that

$$\frac{d}{dt} \ln\left(BK^{1/2} \right) = \frac{1}{2} (\hat{\boldsymbol{n}}\hat{\boldsymbol{n}} : \nabla \boldsymbol{u}). \qquad (29)$$

The formal solution in the comoving frame is

$$\ln\left(BK^{1/2} \right)(t) = \frac{1}{2} \int^t dt'\, \hat{\boldsymbol{n}}\hat{\boldsymbol{n}} : \nabla \boldsymbol{u}(t') \equiv \frac{1}{4} \zeta_n(t), \qquad (30)$$
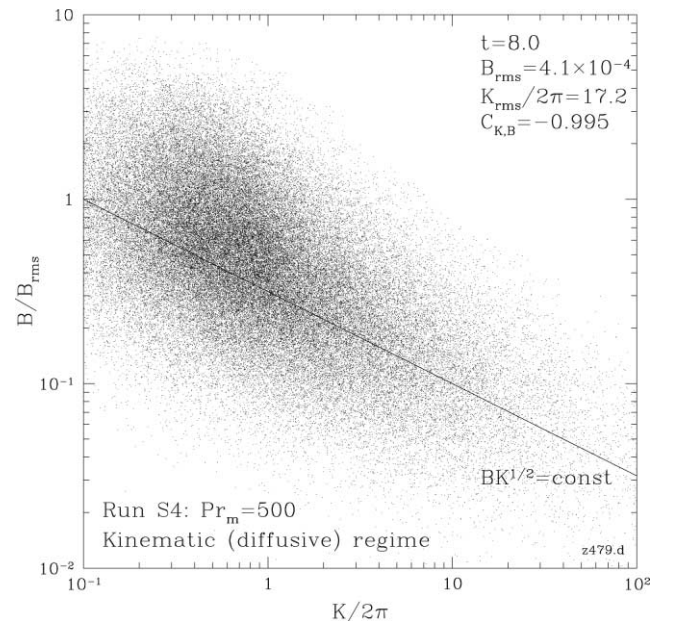

Fig. 8.—Scatter plot of B vs. K at $t = 8$ during the kinematic stage of our run S4 (the 256^3 data were thinned out by a factor of 200).

---

[8] The second term in eq. (27) represents the contribution from the mirror force $\nabla_\parallel B/B$, which is also large only in the bends, where its rms value grows at the same rate as K_{rms} (Schekochihin et al. 2002c). The pdf of the mirror force has a power tail with the same scaling as the pdf of curvature (§ 3.2.4) and is, therefore, also dominated by the outer scales (A. A. Schekochihin 2003, unpublished).

while for the field strength we have

$$\ln B(t) = \int^t dt' \, \hat{\boldsymbol{b}}\hat{\boldsymbol{b}}:\nabla \boldsymbol{u}(t') \equiv \frac{1}{2}\zeta_b(t). \qquad (31)$$

It can be shown (A. A. Schekochihin 2002, unpublished), for the Kazantsev model velocity given by equation (7) and in neglect of bending and diffusion, that the joint probability density function (pdf) of $\zeta_b(t)/t$ and $\zeta_n(t)/t$ is exactly the same as the joint pdf of $\zeta_1(t)/t$ and $\zeta_2(t)/t$, the finite-time Lyapunov exponents corresponding to the stretching and the "null" direction of the flow (see § 3.3 for a quick overview of the relevant definitions). This means that while $\zeta_b(t)$ increases linearly with time and is responsible for the field stretching, $\zeta_n(t)$ fluctuates around zero. Equation (30) then suggests that $BK^{1/2}$ is a special combination in which the effect of stretching is cancelled.[9] Least-squares fits performed on log scatter plots of B versus K such as Figure 8 give $BK^{\alpha} = $ const with $\alpha \simeq 0.47$, which gives a measure of both the detailed anticorrelation between B and K and the extent to which it can be understood via essentially geometrical arguments such as the one we have just presented.[10] Clearly, these should break down for curvatures close to either the inverse flow scale ($K \sim k_\nu$) or the inverse resistive scale ($K \sim k_\eta$), but it is nontrivial that they appear to work quite well away from the cutoffs.

3.2.4. The Curvature Distribution

We have seen that the large values of K_{rms} are due to the large values of curvature in the bends, where the field itself is weak. Figure 8 indicates that these only occupy a small fraction of the volume (in most places, fields are strong and straight). In order to ascertain that this is true, as well as to get a more detailed statistical description of the field-line geometry, Schekochihin et al. (2002c) found the pdf of curvature analytically:

$$P_K(K) = \frac{6}{7}\frac{K}{\left[1 + (K/K_*)^2\right]^{10/7}}, \qquad (32)$$

where $K_* = (2\kappa_4/7\kappa_2)^{1/2}$ (see eq. [8] for definitions of κ_2 and κ_4). This solution means that in most of the volume, the field-line curvature is comparable to the inverse eddy size ($K \sim K_* \sim k_\nu$), while the distribution of curvatures in the bends is characterized by a power law $P_K(K) \sim K^{-13/7}$. This scaling is
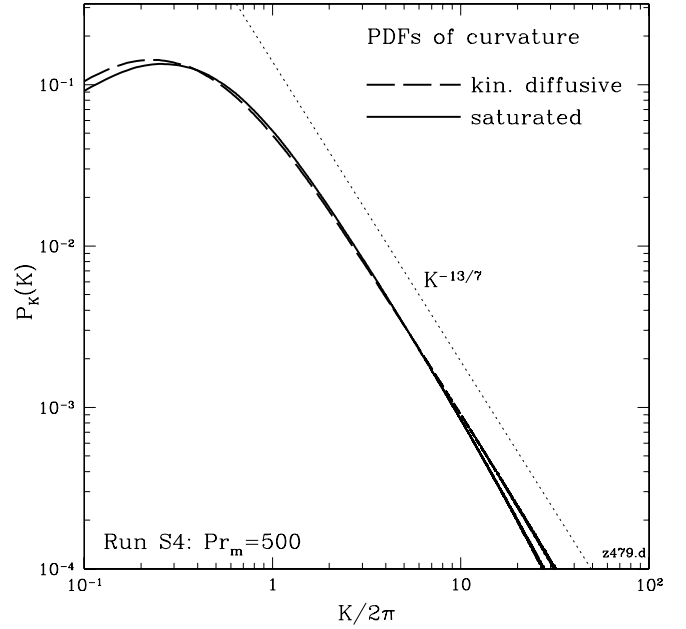

FIG. 9.—Curvature pdf's for run S4 during the kinematic regime (with diffusion) and in the saturated state. Curvature pdf's for all other runs are similar.

reproduced very well in our simulations (see Fig. 9). Note that we find all curvature-related quantities to be quite well converged already after a relatively short running time (unlike the quantities containing field strength, which fluctuate very strongly). We believe that this is due to statistics of curvature being a geometrical property of the field lines independent of the fluctuating stretching rates (see footnote 8).

A stationary power-like pdf of K is possible because curvature, unlike field strength, has an explicit dependence not only on $\nabla \boldsymbol{u}$ but also on $\nabla\nabla \boldsymbol{u}$. The second derivatives of $\boldsymbol{u}$ enter as a source term in equation (25) and are responsible for bending the fields. Thus, the flow scale is explicitly present in the curvature equation and, consequently, in the curvature statistics.

Formally speaking, integer moments of the distribution given by equation (32) diverge: in the diffusion-free calculation of Schekochihin et al. (2002c), while the pdf converges to the stationary profile given by equation (32), all moments $\langle K^n \rangle$ grow exponentially without bound. In the problem with diffusion, the power tail of the curvature pdf is cut off at the resistive scale ($K \sim k_\eta$) and the moments saturate at values that scale with Pr_m: e.g., $K_{\mathrm{rms}} \sim k_\nu \, \mathrm{Pr}_m^{2/7}$ asymptotically with $\mathrm{Pr}_m \to \infty$. The numerical results demonstrate the (nontrivial) fact that the curvature statistics above the resistive scale are not affected by the presence of diffusion. In other words, there is no resistive anomaly for the curvature: $\eta \to +0$ and $\eta = 0$ give the same result. Note that the use of hyperdiffusion does not change the scaling of $P_K(K)$ (Schekochihin et al. 2002d), another indication that curvature statistics do not depend on the dissipation mechanism. It can be seen in § 3.4 that, unlike the curvature, the field strength has statistics that are crucially influenced by the resistive cutoff.

A note of caution is in order. We have found in the course of our numerical investigations that the geometric properties of the dynamo-generated field, while very well behaved in terms of convergence in time, are quite sensitive to spatial resolution. Specifically, with our spectral code, if the magnetic diffusivity η is not large enough to ensure a fairly large separation between the resistive scale and the dealiasing cutoff,

---

[9] In Schekochihin et al. (2002d), we argued that $BK \sim$ const based on a flux conservation argument, which, however, involved some ad hoc assumptions about the fold geometry. Constantin et al. (1995) and Brandenburg et al. (1995) also argued in favor of $BK \sim$ const on the basis of an alternative form of eq. (25). The numerical evidence presented here and in § 4.1 appears rather to support $BK^{1/2} = $ const. It is, however, possible that in the regions of strong field and low curvature, the relation between B and K is closer to $B \sim 1/K$.

[10] The underlying geometrical nature of the curvature-related statistics becomes especially clear in two dimensions. The curvature and field strength in two dimensions are related by $BK^{1/3} = $ const (again neglecting diffusion and bending). This follows from the fact that, in two dimensions, $\hat{\boldsymbol{n}} \perp \hat{\boldsymbol{b}}$, so, $\hat{\boldsymbol{b}}$ being the stretching direction, $\hat{\boldsymbol{n}}$ must necessarily be the compressive one; incompressibility then requires $\zeta_n = -\zeta_b$, whence $d\ln(BK^{1/3})/dt = 0$. A statistical calculation for the Kazantsev model shows that the pdf of $\ln(BK^{1/3})$ is a δ-function (A. A. Schekochihin 2002, unpublished). A purely geometrical consideration of the field lines also gives $BK^{1/3} = $ const (Thiffeault 2004). Furthermore, it turns out that the power tail of the curvature pdf in two dimensions derived by Schekochihin et al. (2002c) for the Kazantsev dynamo model, $P_K(K) \sim K^{-5/3}$, can be reproduced for the curvature distribution along a generic parabola (J.-L. Thiffeault 2002, private communication). It is an open question whether similar purely geometric treatment is possible in three dimensions.

the folded structure is polluted by spurious small-scale "ringing" in the field. The method of computing curvature is also important. Better quality results are obtained by using the formula $K = (B \cdot \nabla B) \cdot (I - \hat{b}\hat{b})/B^2$ than by directly differentiating the unit vector ($K = \hat{b} \cdot \nabla \hat{b}$).

3.3. *How Is the Small-Scale Dynamo Possible?*

The folded-structure diagnostics considered in § 3.2 tell us what field configurations are generated by random stretching. Diffusion did not figure prominently in the theoretical discussion that we have offered in support of our numerical results. Its only effect has been to set the minimum scale of field variation (reversals and curvature). However, if the fields reverse at the resistive scale, why are they not destroyed by diffusion? In other words, how is the small-scale dynamo possible at all?

Let us consider the simplest imaginable model of turbulent stretching: a velocity field random in time and exactly linear in space (Zel'dovich et al. 1984). In this model, any physics that depends on the finiteness of the flow scale is lost: for example, the stationary curvature pdf (§ 3.2.4) cannot be derived for an exactly linear velocity (a more serious shortcoming will be the incorrect result for the growth rates of $\langle B^n \rangle$; see § 3.4). The fields produced by a linear flow still have a folded structure, but there is no bending, so the folds can be arbitrarily long.

If the velocity field is linear, equation (2) is solved (in the comoving frame) by the *Ansatz*

$$B(t, \, x) = \int \frac{dk_0^3}{(2\pi)^3} \tilde{B}(t, \, k_0) e^{ik(t, \, k_0) \cdot x}, \quad (33)$$

where $k(0, \, k_0) = k_0$ and $\tilde{B}(0, \, k_0) = B_0(k_0)$ is the Fourier transform of the initial field. After direct substitution into equation (2), we find the following solution:

$$\tilde{B}^i(t, \, k_0) = \frac{\partial x^i}{\partial x_0^m}(t) B_0^m(k_0) \exp\left[-\eta \int_0^t dt' \, k^2(t, \, k_0)\right], \quad (34)$$

$$k_i = \frac{\partial x_0^m}{\partial x^i}(t) k_{0m}, \quad (35)$$

where $x_0 \rightarrow x(t)$ is the transformation of variables induced by the flow, i.e., $x(t) = x_0(t) + \int_0^t dt' \, u[t', \, x(t')]$. For a linear velocity field, $\partial x^i / \partial x_0^m$ depends on time only.

Equation (34) is a generalization of the Cauchy solution of the ideal induction equation. It can be used to express the statistics of the magnetic field in terms of its initial statistics and the statistics of the (contravariant) metric associated with the flow

$$g^{ij}(t) = \frac{\partial x^i}{\partial x_0^m} \frac{\partial x^j}{\partial x_0^m}. \quad (36)$$

The metric contains all the statistical information necessary to describe random advection of arbitrary tensor fields by the ambient velocity field (e.g., Boldyrev & Schekochihin 2000). Since g^{ij} is symmetric and positive definite, it has a set of real positive eigenvalues $\{e^{\zeta_1}, \, e^{\zeta_2}, \, e^{\zeta_3}\}$ and an orthonormal basis $\{\hat{e}_1, \, \hat{e}_2, \, \hat{e}_3\}$. This is the Lyapunov basis of the flow, and $\zeta_i(t)/t$ are the finite-time Lyapunov exponents. The quantities ζ_i can be considered ordered so that $\zeta_1 \geq \zeta_2 \geq \zeta_3$. Incompressibility requires that $\zeta_1 + \zeta_2 + \zeta_3 = 0$ at all times. Therefore, $\zeta_1 > 0$ corresponds to the stretching direction, $\zeta_3 < 0$ to the compressive direction, and ζ_2 to the "null" direction. The exponent ζ_2 can be either positive or negative. In time-reversible flows
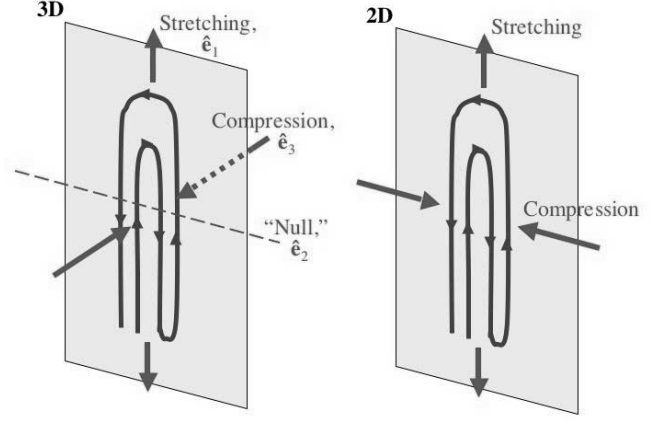

FIG. 10.—Fold alignment in three and two dimensions.

(e.g., in the Kazantsev model), $\langle \zeta_2 \rangle = 0$ (in real turbulent flows, it is usually positive). Note that Lyapunov eigenvectors stabilize exponentially fast in time, while the finite-time Lyapunov exponents ζ_i/t converge to constant values as $\sim 1/t$ (Goldhirsch et al. 1987).

Equation (34) implies that B aligns with the stretching direction $\hat{e}_1$. In an ideal fluid,

$$B^2 \sim \exp(\zeta_1) \quad (37)$$

for a typical realization.[11] While $\tilde{B}$ transforms as a vector (times the exponential factor due to diffusion; see eq. [34]), k transforms as a covector (eq. [35]). Therefore, it aligns with the stretching direction of the *covariant* metric, which is the inverse of g^{ij}. Its stretching direction is then the same as the compressive direction of g^{ij}, with exponent $-\zeta_3 > 0$, so k aligns with the compressive direction $\hat{e}_3$ and grows exponentially in time. Therefore, most modes $\tilde{B}(t, \, k_0)$ (eq. [34]) decay superexponentially. The only modes that are not thus suppressed are those for which the angle between the initial wavenumber k_0 and the compressive direction is very close to 90°, with the window of allowed angles narrowing exponentially fast in time (Zel'dovich et al. 1984). Since $k \perp \tilde{B}$ and $\tilde{B} \parallel \hat{e}_1$, we have $k \parallel \hat{e}_2$; i.e., the surviving fields can have reversals only in the "null" direction. In contrast, in two dimensions, the field aligned with the stretching direction must necessarily reverse in the compressive direction, so the folds are destroyed by diffusion (see simulations by Kinney et al. 2000). These statements (illustrated by Fig. 10) explain qualitatively why small-scale dynamo works in three dimensions but not in two dimensions (Zel'dovich 1957). Even in three dimensions, diffusion leads to suppression of most modes. Zel'dovich et al. (1984) showed that the remaining ones, with the correct alignment of k and B, are sufficient to make the total magnetic energy grow as

$$B^2 \sim \exp[(\zeta_1 - \zeta_2)/2]. \quad (38)$$

In the linear velocity model, a system of infinite size can contain an infinite number of initial wavenumbers k_0 (no new modes are produced by a linear velocity field). Only an exponentially small fraction of k_0 values contribute to the growing

---

[11] In other words, $\zeta_1 = \zeta_b$, where ζ_b is defined in eq. (31). As we noted in § 3.2.3, it is also possible to show that the curvature $K = \hat{b} \cdot \nabla \hat{b}$ aligns with the "null" direction and $\zeta_2 = \zeta_n$ (eq. [30]) for a linear velocity field.

field at any given time. In a finite system, only a finite number of modes can exist, limited by the system-size and resistive cutoffs. In a linear velocity field, they would all eventually be suppressed. In a finite-scale flow, besides stretching, there is also bending of folds, which effectively means that new modes are made. Thus, the effect of the finiteness of the flow scale is that modes are continually resupplied.

One might wonder how the Zel'dovich et al. (1984) small-scale dynamo mechanism relates to the classic "stretch-twist-fold" (STF) picture of the fast dynamo (Vainshtein & Zel'dovich 1972; Childress & Gilbert 1995). The mechanism outlined above makes the small-scale dynamo possible as a *statistical* effect: the random flow produces certain typical structures (folds), then diffusion selects a subset of these structures that turns out to be sufficiently large *on the average* to give rise to energy growth. No specific form of the flow is prescribed: three-dimensionality, randomness in time, and spatial smoothness are all that is required. In contrast, the STF picture shows what might happen to a flux loop in three dimensions if a particular set of transformations is applied to it. Vainshtein et al. (1996) studied numerically the evolution of a single circular field line in a chaotic flow that was designed to favor STF transformations. They observed that only at the very beginning of the evolution could the line be seen to actually stretch, twist, and fold. It then quickly became randomly tangled and, while the field did grow exponentially, it was not possible to claim that the mechanism of this growth was successive stretching, twisting, and folding. Note also that in order to twist the field lines, the flow must possess pointwise helicity (net helicity is not required because the sense of the twist can be arbitrary). However, numerical experiments by Hughes et al. (1996) suggest that flows with zero pointwise helicity can still generate small-scale fields. Thus, while the STF mechanism is, in principle, a viable dynamo, it remains unclear whether a generic turbulent flow contains enough STF realizations to amplify magnetic energy this way, whether this is the statistically prevalent kind of dynamo, and what its relation to the Zel'dovich et al. (1984) mechanism is.

It would be worthwhile to make careful measurements of the fold alignment with respect to the local Lyapunov basis in numerical simulations. We leave such a study outside the scope of this paper.

3.4. *Self-Similar Growth and Intermittency*

The subviscous range is bounded on the IR side by the viscous scale k_ν^{-1} (the flow scale) and on the UV side by the resistive scale k_η^{-1}. Taking $k_\nu \to 0$ amounts to assuming a linear velocity field; $k_\eta \to \infty$ is the diffusion-free limit. Both limits are singular for at least some of the statistical quantities of interest. For the magnetic energy spectrum, the resistive cutoff k_η is explicitly present, but the IR cutoff $k_* \sim k_\nu$ only enters via a small correction to the growth rate (eq. [12]). On the other hand, the flow scale is present explicitly in the quantities related to the field structure: thus, e.g., the field-line curvature is allowed to have a stationary pdf only because of the broken scale invariance on the IR side ($K_* \sim k_\nu$; eq. [32]), while diffusion simply cuts off the pdf at large K. In both cases, analytical theory is facilitated because one of the cutoffs does not matter.

For the field strength distribution, both cutoffs turn out to be important. Analytical theory exists only for the diffusion-free case ($k_\eta = \infty$; § 3.4.1) and for a purely linear velocity field with diffusion ($k_\nu = 0$, k_η finite; § 3.4.2). Neither of the two limits correctly describes intermittency of the magnetic field

generated by a finite-scale flow (§ 3.4.3). The linear velocity model (reviewed in § 3.3) is very helpful in understanding the way the small-scale dynamo works in the presence of diffusion. The inadequacy of this model as a theory of intermittency has not until now been properly appreciated, so we would like to emphasize the importance of the results reported in § 3.4.3.

3.4.1. *The Diffusion-free Case*

The situation in the diffusion-free regime is straightforward. Equation (2) with $\eta = 0$ admits the formal solution given by equation (31) for $B(t)$ in the comoving frame, so, on the basis of the Central Limit Theorem, B should have a lognormal distribution. As usual, the Kazantsev model given by equation (7) allows for an exact solution. The resulting pdf of B is, indeed, lognormal, with a growing mean $\langle \ln [B(t)] \rangle = \frac{3}{4} \kappa_2 t$ and dispersion $D = \kappa_2 t$ (see eq. [41]). As the width of this lognormal profile grows with time, the field becomes increasingly more intermittent: the moments of the field strength are

$$\langle B^n \rangle \propto \exp\left[\tfrac{1}{4} \kappa_2 n(n + 3)t\right]. \tag{39}$$

This formula can be obtained both from direct averaging of the induction equation (e.g., Schekochihin & Kulsrud 2001) and from averaging equation (37) over the statistics of the finite-time Lyapunov exponent $\zeta_1(t)/t$ (Chertkov et al. 1999).

A good conventional measure of intermittency is the kurtosis $\langle B^4 \rangle / \langle B^2 \rangle^2 \propto \exp(2\kappa_2 t)$, which can be roughly interpreted as the inverse volume filling fraction. The kurtosis and all other normalized moments $\langle B^{mn} \rangle / \langle B^m \rangle^n$ grow exponentially. This means that the dominant contribution to each moment $\langle B^n \rangle$ comes from a different substructure, which occupies an exponentially decreasing fraction of the volume compared with those contributing to lower moments. This is because the fields everywhere are stretched exponentially, but with a fluctuating stretching rate $\zeta_1(t)/t$ (eq. [37]), so any occasional difference between substructures tends to be amplified exponentially.

3.4.2. *A Model with Diffusion and a Linear Velocity Field*

The situation changes dramatically when diffusion is introduced. Exact theory for one-point statistics in this case is problematic even for the Kazantsev velocity because of the closure problem associated with the diffusion term. The problem is solvable, however, for the particular case when the velocity field is exactly linear and the system domain is infinite (Zel'dovich et al. 1984; Chertkov et al. 1999; Nazarenko et al. 2003; West et al. 2004). The general outline of the solution was given in § 3.3, leading to the growth of a typical field realization according to equation (38). Chertkov et al. (1999) worked out the moments $\langle B^{2n} \rangle$ averaged over the (Gaussian) distribution of ζ_i for the Kazantsev model and found

$$\langle B^{2n} \rangle \propto \mathrm{Pr}_m^{5n/4} \exp[(3/16)\kappa_2 n(n + 4)t]. \tag{40}$$

Thus, it appeared that, in the diffusive regime, while the specific expression for the moments changed, the intermittency continued to increase exponentially in time just as it did in the diffusion-free case.

3.4.3. *The Finite-Scale Flow: Self-Similarity*

We already saw in § 3.2 that the linear velocity model is not sufficient to describe the field structure. The intermittency
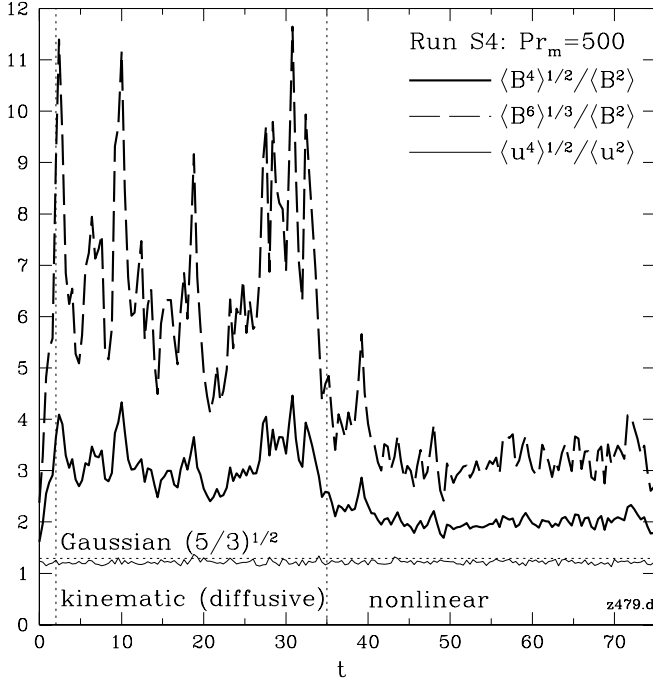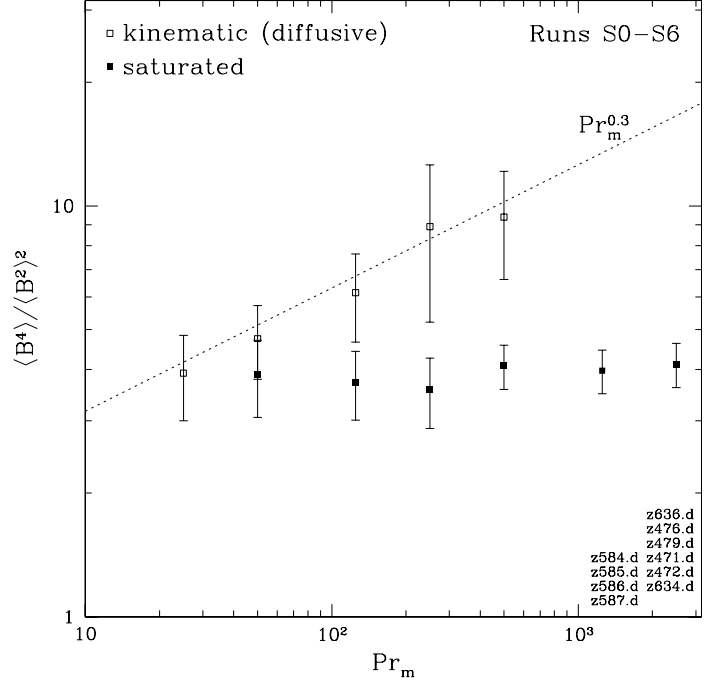
FIG. 11a

FIG. 11b

FIG. 11.—(a) Evolution of normalized moments of the magnetic field strength for run S4. The (square root of) kurtosis of the velocity field is given for comparison. (b) Kurtosis $\langle B^4 \rangle / \langle B^2 \rangle^2$ of the magnetic field strength during the kinematic stage of runs S0–S4 and in the saturated state of runs S1–S6. The values plotted are listed in Table 1.

properties of the field strength are also affected (and, indeed, drastically changed) by the presence of the finite system scale.

In an infinite system, intermittency can grow with time because for ever higher moments $\langle B^n \rangle$, ever smaller sets of substructures can always be found in which the field has exponentially outgrown the rest of the system and that, therefore, dominantly contribute to $\langle B^n \rangle$. By contrast, in a finite system, only a finite number of exponentially growing substructures can exist, so the contribution to all moments must eventually come from the same fastest growing one. The statistics of the field should, therefore, be *self-similar*, with $\langle B^n \rangle$ growing at rates proportional to n, not n^2, and all normalized moments $\langle B^{mn} \rangle / \langle B^m \rangle \langle B^n \rangle$ saturating.[12]

In our simulations, there is unambiguous evidence for the self-similar evolution. After initial diffusion-free growth, the normalized moments saturate (Fig. 11a). The pdf of the magnetic field strength becomes self-similar: namely, the pdf's of $B/B_{\rm rms}$ collapse onto a single stationary profile throughout the kinematic stage of the dynamo (Fig. 12). The large-B tail of the pdf of $B/B_{\rm rms}$ is reasonably well fitted by a lognormal distribution. Specifically, suppose that the pdf of $z = \ln B$ is

$$P_z(z) = (\pi D)^{-1/2} \exp\left[-\frac{(z - \langle \ln B \rangle)^2}{D}\right]. \qquad (41)$$

[12] This effect was not properly appreciated in our discussion of the kinematic dynamo in Schekochihin et al. (2002d). Note that for the problem of passive scalar decay, self-similar behavior was found in two-dimensional maps (the so-called strange mode; see Pierrehumbert 1994, 2000; Sukhatme & Pierrehumbert 2002) and even in scalar-mixing experiments (Rothstein et al. 1999). Numerical simulations of the advection-diffusion equation in two dimensions have shown the same property (Fereday & Haynes 2004). In map dynamos studied by Ott and coworkers (Ott 1998), all moments of the field also grew at the same rate.

Then $\langle B^n \rangle \propto \exp(\langle \ln B \rangle n + Dn^2/4)$, so $D = \ln(\langle B^4 \rangle^{1/2}/\langle B^2 \rangle)$. In the diffusive regime, $D = $ const and the field strength statistics become self-similar: the pdf of $\zeta = \ln(B/B_{\rm rms})$ is stationary,

$$P_\zeta(\zeta) = (\pi D)^{-1/2} \exp\left[-\frac{(\zeta + D/2)^2}{D}\right]. \qquad (42)$$

The lognormal fit in Figure 13 is obtained by calculating D from the numerical data and comparing the profile given by equation (42) with the numerically calculated pdf. The fit is qualitative but decent, considering the simplicity of the chosen profile given by equation (42) and large statistical errors in determining $\langle B^4 \rangle / \langle B^2 \rangle^2$ (Fig. 11b).

The pdf at small B appears to be power-like, $BP(B) \sim B^{2.7\ldots2.8}$ in all regimes (Fig. 12b). This tail extends to the limit of our diagnostic's resolution [$BP(B) \sim 10^{-5}$ at $B \sim 10^{-3}B_{\rm rms}$, not shown], but there may be an unresolved lognormal tail at even smaller B. It is clear that, while the large-B tail describes the straight segments of the folds, the small-B tail gives the field strength distribution for the weak fields in the bends.

Note that, in space, intermittency of the field strength means that the growing fields do not uniformly fill the volume. More specifically, intermittency is often associated with the presence of "coherent structures" that have disparate spatial dimensions. For the dynamo-generated magnetic fields, they are the folds, for which the disparate dimensions are their length and the field-reversal scale. A linear velocity field allows the folds to be elongated indefinitely, thus giving rise to arbitrarily large aspect ratios between the two scales. In reality, the length of the folds cannot be larger than the scale of the flow because of the bending of the folds. The aspect ratio is then bounded from above by the maximum allowed scale separation $\sim Pr_m^{1/2}$.
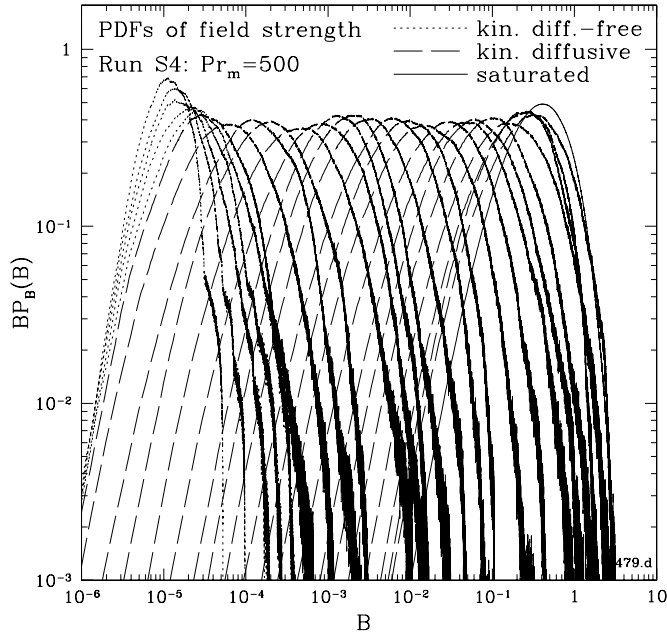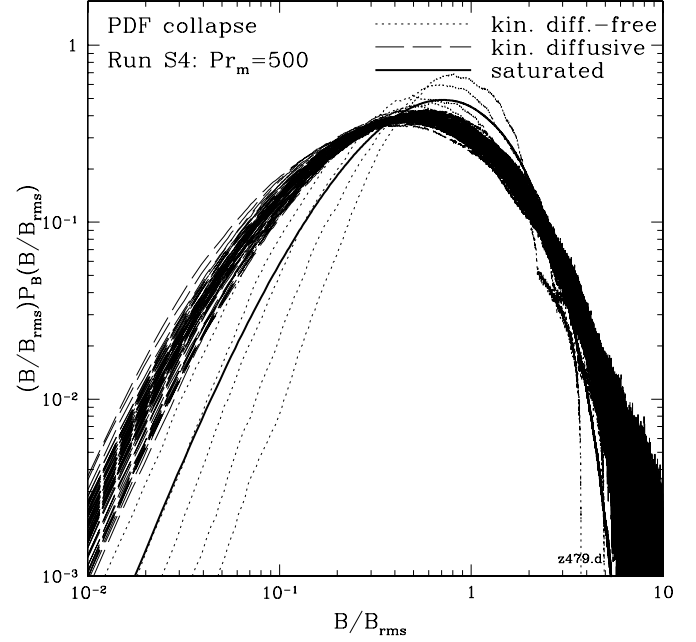
Fig. 12a

Fig. 12b

FIG. 12.—(a) Evolution of the pdf of the magnetic field strength for run S4. The same times are represented as in Fig. 4a. (b) Collapse of the field strength pdf's in the kinematic stage of run S4 onto a self-similar profile. These are pdf's of $B/B_{\rm rms}$. The pdf in the saturated state is shown for comparison.

The hypothetical lognormal pdf given by equation (41) is self-similar only if its dispersion D does not depend on time. In contrast, in the diffusion-free regime, we had $D \sim \gamma t$, where $\gamma \sim \nabla u$ is the stretching rate. In the case of $\eta > 0$ and linear velocity field, the formula for $\langle B^n \rangle$ derived by Chertkov et al. (1999) (eq. [40]) is also consistent with a lognormal distribution for which $D \sim \gamma t$. Both results are only valid transiently, during the time that it takes magnetic fluctuations to

FIG. 13.—The pdf of $B/B_{\rm rms}$ for run S4 (averaged over the kinematic diffusive stage) and the lognormal profile given by eq. (42) with the same D. Also given is the pdf in the saturated state. The pdf's for all other runs are similar.

reach the resistive scale (in the former case) or the system (flow) scale (in the latter case). Since the scale separation is $\sim \mathrm{Pr}_m^{1/2}$ and the spreading over scales proceeds exponentially fast at the rate $\sim \gamma$ (§ 3.1), the time during which intermittency increases is $t_* \sim \gamma^{-1} \ln \mathrm{Pr}_m^{1/2}$. Physically, this is the time necessary to form a typical fold with length of the order of the flow scale and field reversals at the resistive scale, starting from either a flow-scale or a resistive-scale fluctuation. We might conjecture that this time determines the characteristic magnitude of the dispersion in the self-similar regime: $D \sim \gamma t_* \sim \ln \mathrm{Pr}_m^{1/2}$, which implies that the kurtosis $\langle B^4 \rangle / \langle B^2 \rangle^2 = \exp{(2D)}$ increases with Pr_m in a power-like fashion. The specific power law depends on prefactors that may be nonuniversal. The same holds for other normalized moments. Figure 11b is an attempt to test this hypothesis for a sequence of simulations with increasing Pr_m. The fluctuations in the kinematic regime are very large (see Fig. 11a), so the error bars are too wide to allow us to claim definite confirmation of the power-like behavior, but our results are consistent with a $\langle B^4 \rangle / \langle B^2 \rangle^2 \sim \mathrm{Pr}_m^{0.3}$.

A caveat is in order. At our resolutions, the lognormal fit is, in fact, not the only one that is compatible with the numerical evidence. Stretched exponential and even steep power-tail $[P(B) \sim B^{-4.5}]$ fits of comparable quality can be achieved. Note, however, that a stretched exponential would not be compatible with a Pr_m-dependent kurtosis.

We emphasize that the self-similarity reported here is statistical, not exact. Namely, it does not imply that the magnetic field is simply a growing eigenmode of the induction equation (2). Such an eigenmode does exist for some finite-scale nonrandom (and time independent) flows and maps (Childress & Gilbert 1995). The self-similar pdf we have found here is a natural generalization of this eigenmode dynamo to random flows.

A testimony to the statistical nature of the self-similarity is the tendency of the growing field configuration to undergo sudden disruptions when the self-similar profiles are rapidly
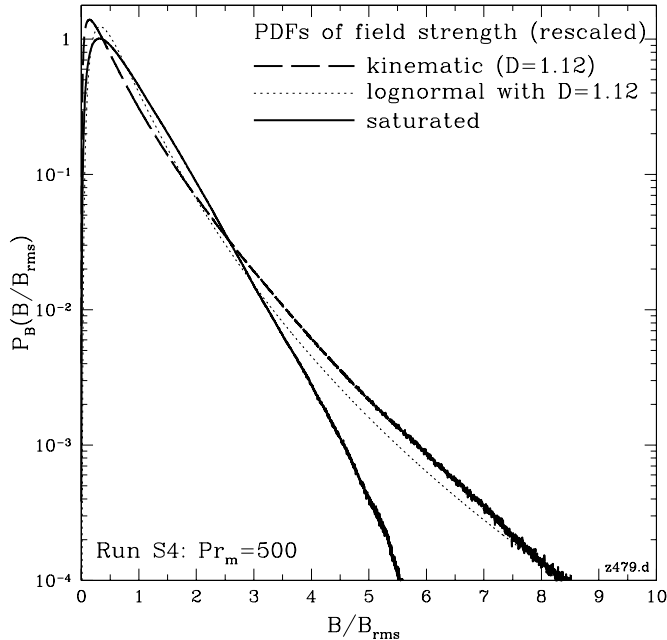
destroyed and then regenerated by the dynamo. These disruptions are manifested, e.g., in sudden destruction of the large-k tails of magnetic spectra (Fig. 4a). These events are correlated with large downward fluctuations of the velocity field. Indeed, when such a fluctuation occurs, the stretching rate $\gamma \sim \nabla u$ drops, the resistive scale $l_\eta \sim (\eta/\gamma)^{1/2}$ increases, and the whole field structure with direction reversals at the previously established smaller resistive scale is quickly dissipated. Since it is the stronger straight direction-reversing fields that are destroyed, the tail of the field strength pdf is suppressed. The self-similar statistics are quickly reestablished as the magnetic field adjusts to the new stretching rate.

Of course, the disruptions are nothing more than extreme events in what is a continuous series of fluctuations. Their presence shows the degree of disorder behind the self-similar statistics.

3.5. *Summary of the Kinematic Dynamo*

We have established the following properties of the kinematic regime:

1. The bulk of the exponentially growing magnetic energy is concentrated at the resistive scale $l_\eta \sim \mathrm{Pr}_m^{-1/2} l_\nu$. The magnetic energy spectrum peaks at $k_\eta \sim l_\eta^{-1}$, and in the subviscous range $k_\nu \ll k \ll k_\eta$ it has a positive spectral exponent consistent with the theoretical prediction $k^{3/2}$ (Kazantsev 1968; Kulsrud & Anderson 1992).

2. The fields generated by the dynamo have folded structure: they reverse direction at the resistive scale with the field lines remaining straight (and fairly well aligned) up to the scale of the flow. It is the direction reversals that are responsible for the magnetic energy spectrum peaking at the resistive scale. In the regions of curved field (bends), the field is weak. The field's strength and its curvature are, thus, anticorrelated. The theory of Schekochihin et al. (2002c) is broadly confirmed.

3. The growing direction-reversing fields are intermittent in space. The field strength distribution is consistent with a lognormal profile and evolves self-similarly with time. The volume fraction occupied by the growing fields decreases with increasing Pr_m in a power-like fashion.

The Zel'dovich et al. (1984) mechanism of fold alignment (§ 3.3) explains the existence of the dynamo.

4. THE NONLINEAR SATURATED STATE

The kinematic growth of the magnetic energy must culminate in a saturated nonlinear state. When does the nonlinearity (the Lorentz tension force in eq. [1]) become important? We showed in § 3.2 that the kinematic dynamo produced folded fields for which $\boldsymbol{B}\cdot\nabla\boldsymbol{B} \sim k_\nu B^2$. This means that the tension force can start to oppose the purely hydrodynamic terms in equation (1) once $\boldsymbol{B}\cdot\nabla\boldsymbol{B} \sim \boldsymbol{u}\cdot\nabla\boldsymbol{u} \Leftrightarrow B^2 \sim u_\nu^2$, i.e., when the magnetic energy becomes comparable to the energy of the viscous-scale eddies. Note that this is a nontrivial statement that only holds for the folded field: in an unstructured field with the same $k_{\mathrm{rms}} \sim k_\eta$, we would have had $\boldsymbol{B}\cdot\nabla\boldsymbol{B} \sim k_\eta B^2$ and the nonlinearity would have set in at much lower field energies $B^2/u_\nu^2 \sim k_\nu/k_\eta \sim \mathrm{Pr}_m^{-1/2}$.

In runs S1–S6, the viscous scale is the same as the forcing scale, so the above arguments imply saturation with roughly equal kinetic and magnetic energies. We find that the saturated values of $\langle B^2 \rangle$ grow with Pr_m toward an apparent constant asymptotic value somewhat above $\langle u^2 \rangle$ (Fig. 14; cf. Brummell et al. 2001).
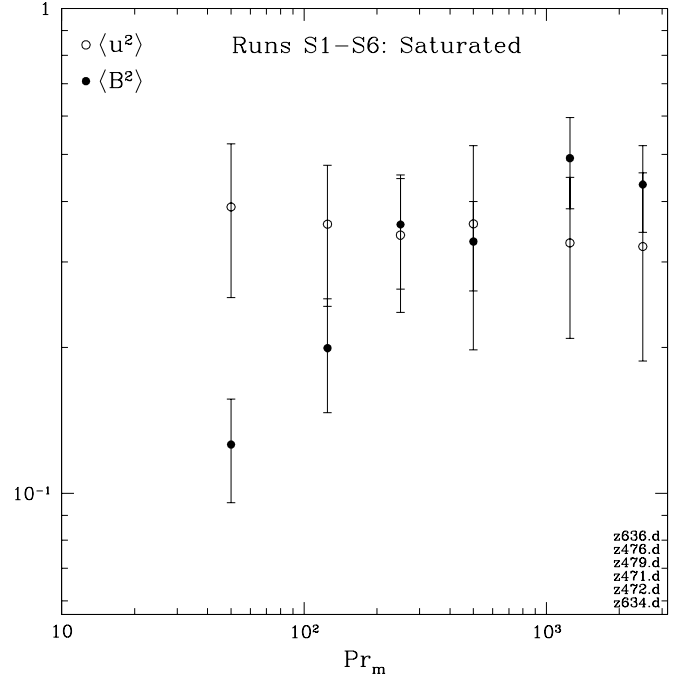

Fig. 14.—Saturated values of the kinetic and magnetic energies vs. Pr_m. The values plotted are listed in Table 1.

Although a number of heuristic models of back-reaction have recently been proposed (Subramanian 1999, 2003; Kim 1999, 2000; Boldyrev 2001; Nazarenko et al. 2001; Schekochihin et al. 2002b, 2002d, 2004b; see also § 4.3), the exact mechanism of the nonlinear saturation in isotropic MHD turbulence is not currently well understood even on the qualitative level. One must, therefore, probe the nonlinear physics by careful numerical analysis. As always in turbulence problems, only statistical statements can be expected to have any degree of universal applicability. The statistical averages are replaced by time averages, so, in order to collect statistics, simulations must be run for a long time *after* the statistical steady state has been achieved. We present statistical results averaged over 20 time units, after all discernible systematic change of the nonlinear state ceased.

We first establish the survival of the folded field structure in the saturated state (§ 4.1), then look at the magnetically induced subviscous velocity fluctuations (§ 4.2), and, finally, study the magnetic energy spectrum, for which a nonlinear saturation model is described and tested (§ 4.3). Intermittency in the saturated state is considered in § 4.4. A summary is given in § 4.5.

4.1. *Persistence of the Folded Structure*

A key fact that we learn from numerical simulations is that the field stays folded after its energy saturates (Fig. 15). All main features of the folded structure observed in the kinematic regime (§ 3.2) carry over to the saturated state:

1. Field varies along itself at the scale of the flow. Its characteristic parallel wavenumber (eq. [13]) is $k_\parallel \sim k_\nu$ and does not depend on Pr_m, while $k_{\boldsymbol{B}\times\boldsymbol{J}}$ and k_{rms} (eqs. [14] and [15]) increase with Pr_m (Fig. 16; cf. Brandenburg et al. 1995; Brummell et al. 2001). The scaling $k_{\mathrm{rms}} \sim k_{\boldsymbol{B}\times\boldsymbol{J}} \sim \mathrm{Pr}_m^{1/2}$ appears to be recovered asymptotically with Pr_m but is much less well satisfied at our finite Pr_m than it was in the kinematic case (cf. Fig. 6b). This is consistent with the flattening of the magnetic energy spectrum discussed in § 4.3.
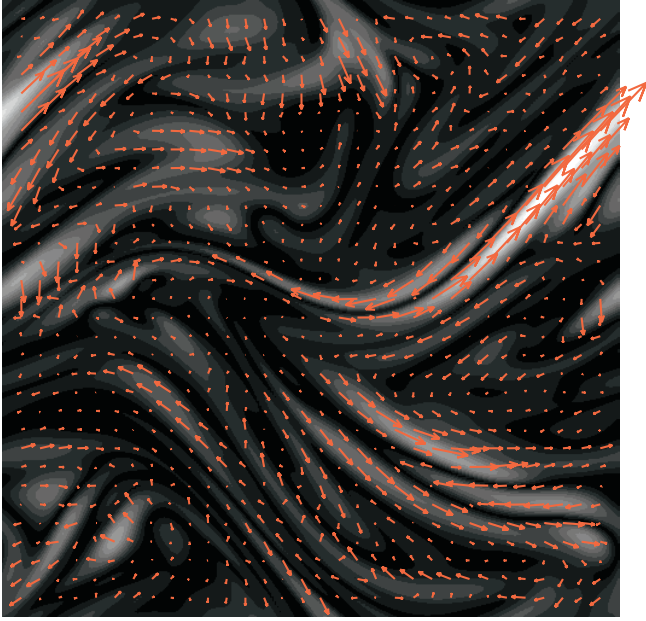
Fig. 15.—Field structure at $t = 76$ in the saturated state of run S4. This is the nonlinear counterpart of Fig. 5.

Fig. 17.—Scatter plot of B vs. K at $t = 76$ in the saturated state of our run S4 (the 256^3 data were thinned out by a factor of 200).

2. The magnetic field strength and curvature remain anti-correlated with the correlation coefficient $C_{K,B}$ (eq. [26]) within 4% of -1 (Table 1) and the log scatter plots of B versus K least squares fitted by $BK^\alpha = \text{const}$ with $\alpha \simeq 0.45$ (Fig. 17; cf. § 3.2.3).

3. The curvature pdf in the saturated state has a power tail with scaling very close to the kinematic $K^{-13/7}$ (the scaling in the saturated case may be slightly steeper than in the kinematic case; see Fig. 9). The bulk of the pdf is concentrated at the flow scales (cf. § 3.2.4).
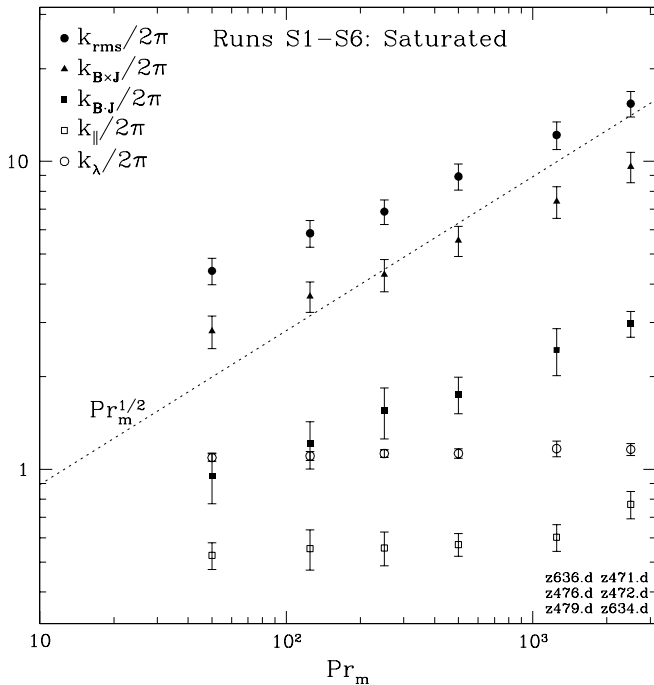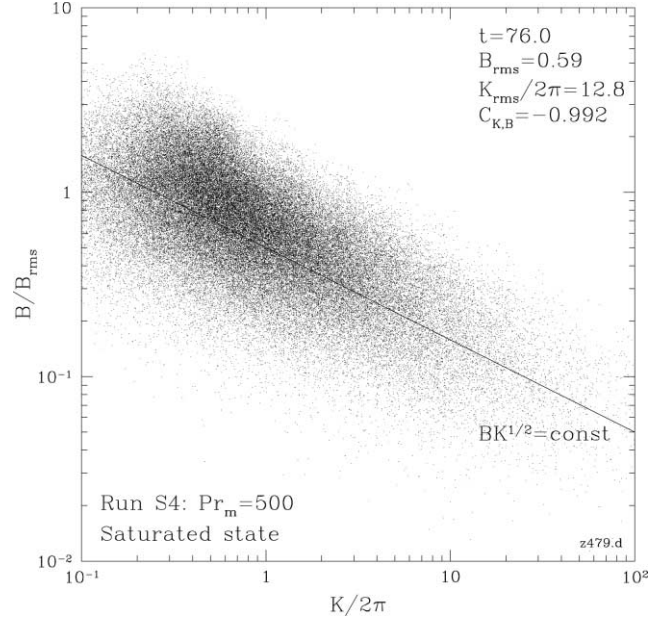

Fig. 16.—Averaged values of various characteristic wavenumbers (defined in § 3.2) vs. Pr_m in the saturated state of runs S1–S6. The values plotted are listed in Table 1. Note that the value of $k_\parallel$ for run S6 is too large as a result of this run being somewhat underresolved.

Physically, it is clear that the preservation of the folded structure is inevitable. The large viscosity of the medium does not allow the setting up of the kind of detailed small-scale flows that would be required to unfold the field without destroying it. Furthermore, a wholesale evacuation of the small-scale degrees of freedom would lead to an unstable situation in which any significant velocity fluctuation would set in motion small-scale field generation and refolding. The latter point was checked numerically by Maron et al. (2004).

The persistence of the kinematic scaling of the tail of the curvature pdf also makes sense. The tail describes the curvature distribution in the bends of the folds, where the magnetic field remains weak even when field energies in the straight segments of the folds approach equipartition levels. Therefore, the situation in the bends is quasi-kinematic, so the curvature statistics are almost the same as in the kinematic limit.

We note one feature of the field structure in the saturated state that differs from the kinematic regime: $k_{B\cdot J}$ (eq. [17]) increases somewhat (Fig. 6a) and appears to scale with Pr_m in the same way as k_{rms} and $k_{B\times J}$: we find $k_{\mathrm{rms}} : k_{B\times J} : k_{B\cdot J} \sim 5{:}3{:}1$ (Fig. 16). This indicates that the direction-reversing fields are less well aligned than in the kinematic case. Geometrically, one can interpret this effect as a transition from flux sheets to flux ribbons. While intuitively such a transition might be attributable to increased mixing efficiency of the velocity field in the saturated state (see § 4.3.1), we do not currently have a satisfactory theoretical picture of this nonlinear effect.

Saturation requires some form of suppression of stretching by the tension force in equation (1). Since the stretching motions are large scale, the back-reaction must have a large-scale coherence. The folded fields, while formally small scale, possess such a large-scale coherence in the form of slow (in space) parallel variation. The persistence of the folded structure in the saturated state is crucial for the saturation model in § 4.3.

4.2. The Tension Force and the Subviscous Velocity Spectrum

The first traces of nonlinearity appear already in the kinematic stage in the form of the small-scale modification of the
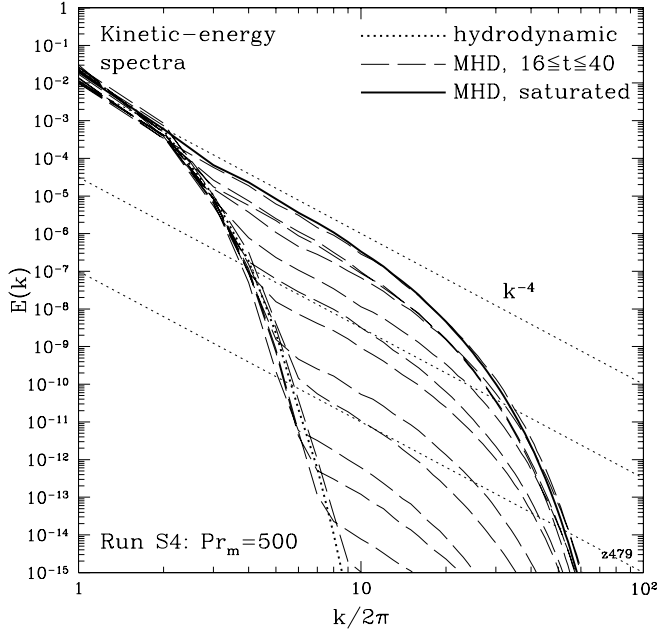
FIG. 18.—Evolution of the kinetic energy spectrum for run S4. We plot the spectrum in the purely hydrodynamic regime ($B = 0$), the spectrum in the saturated state, and the evolving spectra for $16 \leq t \leq 40$ at time intervals of $\Delta t = 2$. The corresponding evolution of the tension spectra is given in Fig. 7a.
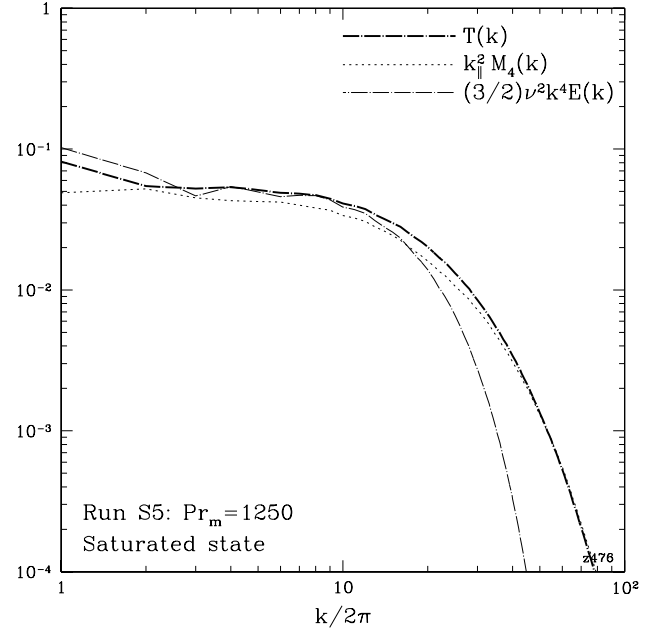

FIG. 19.—Tension spectrum for run S5 (saturated state). For comparison, we also plot the kinetic energy spectrum $E(k)$ compensated by $(3/2)\nu^2 k^4$ and the spectrum of B^2, multiplied by $k_\parallel^2$ (as defined by eq. [13]). The results for runs S1–S4 and S6 are analogous.

velocity spectrum. For $k \gg k_\nu$, the Navier-Stokes equation (1) reduces to the following force balance (in $\boldsymbol{k}$ space):

$$\nu k^2 \boldsymbol{u}(\boldsymbol{k}) \simeq -i\boldsymbol{k}p(\boldsymbol{k}) + \boldsymbol{F}(\boldsymbol{k}), \qquad (43)$$

where $\boldsymbol{F} = \boldsymbol{B} \cdot \nabla \boldsymbol{B}$ is the tension force. Pressure is determined from the incompressibility constraint, $\boldsymbol{k} \cdot \boldsymbol{u}(\boldsymbol{k}) = 0$, and we get for the velocity spectrum at $k \gg k_\nu$

$$E(k) = \frac{1}{2} \int d\Omega_{\boldsymbol{k}} \, k^2 \left\langle |\boldsymbol{u}(\boldsymbol{k})|^2 \right\rangle$$
$$\simeq \frac{1}{2\nu^2 k^4} \int d\Omega_{\boldsymbol{k}} \, k^2 \left\langle \boldsymbol{F}(\boldsymbol{k}) \cdot \left(\mathbf{I} - \frac{\boldsymbol{k}\boldsymbol{k}}{k^2} \right) \cdot \boldsymbol{F}(-\boldsymbol{k}) \right\rangle. \quad (44)$$

By the same argument as in § 3.2.2, the angle integral on the right-hand side is $\sim k^0$, so $E(k) \sim k^{-4}$. Figure 18 shows that the velocity spectrum does indeed develop such a tail at subviscous scales already during the kinematic dynamo stage. The tail thickens as the tension force grows ($F \propto B^2$).

In the saturated state, the tension spectrum remains flat, as does $M_4(k)$, and the relation $T(k) \simeq k_\parallel^2 M_4(k)$ persists: indeed, since the folded structure is preserved, the argument given in § 3.2.2 should continue to apply. The velocity spectrum keeps its k^{-4} tail, and we find that

$$E(k) \simeq \frac{2}{3} \frac{1}{\nu^2 k^4} T(k) \qquad (45)$$

is quite well satisfied (Fig. 19).

Thus, the subviscous k^{-4} tail of the velocity spectrum is a passive feature. It contains very little energy and has nothing to do with the large-scale back-reaction mechanism that causes saturation. It is simply another signature of the folded structure and is present for both kinematic and nonlinear dynamo.

4.3. *Local Anisotropy and Steady State Spectra*

Let us now turn to the key issue of the dynamo physics: how does the dynamo saturate? There must exist a nonlinear

feedback mechanism that (1) maintains a statistically steady magnetic energy level and (2) is compatible with the strongly fluctuating velocity field continuously stirred by the random forcing. Here we outline a model for the saturated spectrum we proposed recently (see Schekochihin et al. 2004b, where it is presented in a somewhat different form) and compare its predictions with our simulations.

4.3.1. *Dynamo Saturation via Local Anisotropization*

Saturation can be achieved if stretching motions are nonlinearly suppressed. This does not have to mean complete elimination of all turbulence: only the $\hat{\boldsymbol{b}}\hat{\boldsymbol{b}}{:}\nabla\boldsymbol{u}$ component of the rate-of-strain tensor leads to work being done against the Lorentz force and must, therefore, be suppressed. It is then natural that the velocity field should become anisotropic with respect to the local direction of the magnetic field. Since the magnetic field has a folded structure (§ 4.1), such a local direction is defined by the tensor $\hat{b}^i \hat{b}^j$, which varies at the scale of the flow (direction reversals cancel). The back-reaction term $\boldsymbol{B} \cdot \nabla \boldsymbol{B}$ in equation (1) is quadratic in $\boldsymbol{B}$, so it makes sense that the nonlinearly modified velocity should be indifferent to field reversals but anisotropic with respect to the direction of the folds.

In order to model such an anisotropization, we build on the existing kinematic theory based on the Kazantsev velocity given by equation (7). Thus far, isotropic correlators $\kappa^{ij}(\boldsymbol{y})$ have been assumed. Now we let κ^{ij} depend on the local direction of the folds. In the presence of one preferred direction defined by the tensor $\hat{b}^i \hat{b}^j$, the correlator of an incompressible velocity field in $\boldsymbol{k}$ space has the following general form:

$$\kappa^{ij}(\boldsymbol{k}) = \kappa^{(i)}(k, \, |\mu|)\big(\delta^{ij} - \hat{k}_i \hat{k}_j\big)$$
$$+ \kappa^{(a)}(k, \, |\mu|)\big(\hat{b}^i \hat{b}^j + \mu^2 \hat{k}_i \hat{k}_j - \mu \hat{b}^i \hat{k}_j - \mu \hat{k}_i \hat{b}^j\big), \quad (46)$$

where $\hat{\boldsymbol{k}} = \boldsymbol{k}/k$, $\mu = \hat{\boldsymbol{k}} \cdot \hat{\boldsymbol{b}}$. It is then possible (Schekochihin et al. 2004b) to derive an equation for the magnetic energy

spectrum at $k \gg k_\nu$ that takes into account the dependence of the velocity statistics on the local direction of the field:

$$\partial_t M = \frac{1}{8}\gamma_\perp \frac{\partial}{\partial k}\left[(1+2\sigma_\parallel)k^2\frac{\partial M}{\partial k} - (1+4\sigma_\perp+10\sigma_\parallel)kM\right]$$
$$+ 2(\sigma_\perp+\sigma_\parallel)\gamma_\perp M - 2\eta k^2 M, \qquad (47)$$

where

$$\gamma_\perp = \int \frac{d^3k}{(2\pi)^3} k_\perp^2 \kappa_\perp(\boldsymbol{k}), \qquad (48)$$

$$\sigma_\perp = \frac{1}{\gamma_\perp}\int \frac{d^3k}{(2\pi)^3} k_\parallel^2 \kappa_\perp(\boldsymbol{k}), \qquad (49)$$

$$\sigma_\parallel = \frac{1}{\gamma_\perp}\int \frac{d^3k}{(2\pi)^3} k_\parallel^2 \kappa_\parallel(\boldsymbol{k}), \qquad (50)$$

and we have denoted $k_\perp = k(1-\mu^2)^{1/2}$, $k_\parallel = k\mu$,

$$\kappa_\perp(\boldsymbol{k}) = \frac{1}{2}(\delta^{ij}-\hat{b}^i\hat{b}^j)\kappa^{ij}(\boldsymbol{k})$$
$$= \frac{1}{2}\left[(1+\mu^2)\kappa^{(i)}(k,\ |\mu|) + \mu^2(1-\mu^2)\kappa^{(a)}(k,\ |\mu|)\right], \qquad (51)$$

$$\kappa_\parallel(\boldsymbol{k}) = \frac{1}{2}\hat{b}^i\hat{b}^j\kappa^{ij}(\boldsymbol{k})$$
$$= \frac{1}{2}(1-\mu^2)\left[\kappa^{(i)}(k,\ |\mu|) + (1-\mu^2)\kappa^{(a)}(k,\ |\mu|)\right]. \qquad (52)$$

In the isotropic case, $\kappa^{(i)} = \kappa^{(i)}(k)$, $\kappa^{(a)} = 0$, which gives $\sigma_\perp = \frac{2}{3}$, $\sigma_\parallel = \frac{1}{6}$, and $\gamma_\perp = (6/5)\bar\gamma$ so equation (47) reduces to the standard kinematic case (eq. [9]).

The derivation of equation (47) depends on the assumption that the tensor $\hat{b}^i\hat{b}^j$ changes at the scale of the flow. This is only true in the regions where the fields are strong and straight. The regions of curved fields (bends of the folds) are not properly described by this formalism, but the fields there are weak (§ 4.1) and occupy a small fraction of the volume compared to the strong straight ones (because of the steep power tail of the curvature pdf; Fig. 9). Since it is the stronger fields that dominate the back-reaction, we believe that our description is a reasonable one.

With a zero-flux boundary condition imposed at some $k_* \sim k_\nu$ and in the limit $\eta \to +0$, equation (47) has the eigenfunction

$$M(k) = (\text{const})e^{\gamma t}k^s K_0(k/k_\eta), \qquad (53)$$

$$k_\eta = \left[(1+2\sigma_\parallel)\gamma_\perp 16\eta\right]^{1/2}, \qquad (54)$$

$$\gamma = \gamma_\perp\left[2(\sigma_\perp+\sigma_\parallel) - \frac{(1+2\sigma_\perp+6\sigma_\parallel)^2}{8(1+2\sigma_\parallel)}\right], \qquad (55)$$

$$s = 2\frac{\sigma_\perp+2\sigma_\parallel}{1+2\sigma_\parallel}. \qquad (56)$$

In the isotropic case, we get the growing kinematic solution: $\gamma = \frac{3}{4}\bar\gamma$ and $s = 3/2$ (see § 3.1). This growth can be quenched by making velocity anisotropic so that it varies more slowly along the folds than across: the values of $\sigma_\perp$ and $\sigma_\parallel$ then drop compared to the isotropic case, and so does the growth rate γ until the dynamo is shut down. Thus, saturation can be achieved by anisotropizing the statistics of the velocity gradients.

The parallel gradients of the velocity field that occur in the numerators $\sigma_\perp$ and $\sigma_\parallel$ (eqs. [49] and [50]) represent stretching motions, while the perpendicular gradients that contribute to $\gamma_\perp$ (eq. [48]) correspond to the two-dimensional mixing (interchange-like) motions that shuffle and bring the direction-reversing magnetic fields sufficiently close together for them to annihilate resistively. The decrease in the values of $\sigma_\perp$ and $\sigma_\parallel$ means that the comparative strengths of mixing and stretching change in favor of mixing. The steady solution is thus a result of a balance between weakened stretching and two-dimensional mixing of the folded fields by the partially two-dimensionalized random flow.

Note that the mixing rate $\gamma_\perp$ may or may not be changed by the nonlinearity, with dynamo saturation achievable either way, provided that the stretching rates weaken sufficiently. What happens to $\gamma_\perp$ is important because it enters the expression for k_η (eq. [54]) and thereby determines the shape of the saturated spectrum. It can be seen in § 5.2 that whether mixing is suppressed is a key issue for the large-Re dynamo. For now, we assume that $\gamma_\perp$ is unchanged and see if we can get a reasonable model of saturation for our viscosity-dominated runs.

4.3.2. Solution of the Model

The condition for saturation is $\gamma = 0$ (see eq. [55]). This, however, does not uniquely fix $\sigma_\perp$ and $\sigma_\parallel$ but only relates them via a quadratic equation. Thus, to get a specific solution, we must make a further assumption about $\sigma_\perp$ and $\sigma_\parallel$. One plausible argument is that the anisotropization of the velocity gradients occurs in such a way that all modes with k above some self-consistently chosen cutoff k_s (the stretching wavenumber) are completely two-dimensional (have $k_\parallel = 0$), while the motions with $k < k_s$ are still isotropic (this is certainly a sensible assumption in the case of large Re; see Schekochihin et al. 2004b and § 5.2). Then the reduction in the integrals in equations (49) and (50) is due to the shrinking of the integration domain in k space, but the integrands are still isotropic [$\kappa^{(i)} = \kappa^{(i)}(k)$, $\kappa^{(a)} = 0$ for $k < k_s$], which implies that $\sigma_\perp/\sigma_\parallel = 4$ as in the isotropic case.

With this assumption, the dynamo saturates ($\gamma = 0$) when $\sigma_\perp = 4\sigma_\parallel \simeq 0.078$. The spectral exponent (eq. [56]) is $s \simeq 0.23$, which, however, is clearly a model-dependent number.

4.3.3. Matching with Simulation Results

The solution given by equation (53) is valid in the limit $k_\eta \gg k_* \sim k_\nu$ (Pr$_m \gg 1$), but, as we are about to see, convergence in Pr$_m$ is only logarithmic. Numerical solution of equation (47) shows that scale separations of several decades are required for the scaling to be discernible. No such scale separations are achievable in direct numerical simulations. Therefore, in order to make a meaningful comparison, we must consider model-predicted spectra for the case of finite separations between the resistive cutoff k_η and the infrared cutoff k_*, where the boundary condition is imposed. Seeking steady solutions of equation (47), we get

$$M(k) = (\text{const})k^s K_{i\tilde\nu(\sigma_\perp,\sigma_\parallel)}(k/k_\eta), \qquad (57)$$

where $\tilde\nu(\sigma_\perp,\ \sigma_\parallel) = [8(\gamma/\gamma_\perp)/(1+2\sigma_\parallel)]^{1/2}$ and k_η, γ, s are defined in equations (54)–(56). The equation for $\sigma_\perp$ and $\sigma_\parallel$ is

obtained from the zero-flux boundary condition: the expression in square brackets in equation (47) must vanish at $k = k_*$ (i.e., no energy passes through the left boundary in k space). This gives

$$\frac{k_*}{k_\eta} K'_{i\tilde{\nu}}\left(\frac{k_*}{k_\eta}\right) - \frac{1 + 2\sigma_\perp + 6\sigma_\parallel}{1 + 2\sigma_\parallel} K_{i\tilde{\nu}}\left(\frac{k_*}{k_\eta}\right) = 0. \quad (58)$$

Together with the assumption $\sigma_\perp = 4\sigma_\parallel$, this is a transcendental equation for $\sigma_\parallel$, which can be solved numerically for any fixed set of parameters k_*, η, $\gamma_\perp$.

Note that in the limit of $k_* \ll k_\eta$, equation (58) reduces to $\sin[\tilde{\nu} \ln(k_*/2k_\eta)] = 0$, whence

$$\gamma = \frac{(1 + 2\sigma_\parallel)\pi^2}{8\left[\ln\left(k_*/2k_\eta\right)\right]^2} \gamma_\perp \sim O\left[\frac{1}{\left(\ln \mathrm{Pr}_m^{1/2}\right)^2}\right]. \quad (59)$$

As $\mathrm{Pr}_m \to \infty$, we have $\gamma \to 0$, converging logarithmically. This is the asymptotic solution discussed in §§ 4.3.1 and 4.3.2.

To make a comparison with our numerical results, we set $k_* = k_0 = 2\pi$, the box wavenumber, and use the following (isotropic) expression for the mixing rate: $\gamma_\perp = (6/5)\tilde{\gamma} = c(\epsilon/\nu)^{1/2}$, where ν is viscosity, $\epsilon = 1$ is the mean forcing power (see eq. [4]), and c is an adjustable parameter. We have compared the model solutions with the (normalized) spectra obtained in our viscosity-dominated runs. The adjustable parameter c was the same ($c = 0.3$) for all cases. The entire sequence is well fitted by the model (except at $k/2\pi = 1, 2$, where boundary conditions and discretization effects are important; see Fig. 20).

Considering the simplicity of our model, its ability to predict nonasymptotic numerical spectra so well is remarkable. It shows that numerical results are consistent with magnetic energy spectra that are peaked at the resistive scale and would have a very flat positive spectral exponent in the interval $k_\nu \ll k \ll k_\eta$ if sufficiently large scale separations were resolved.

4.4. *Intermittency*

In the saturated state, intermittency is reduced, implying tighter packing of the system domain by the magnetic field (Fig. 11a). It is not a surprising result: nonlinear back-reaction imposes an upper bound on the field growth, and once the strongest fields in the dominant substructure saturate, the weaker ones elsewhere have an opportunity to catch up. The pdf of the saturated field is exponential at large B (Fig. 13; cf. Brandenburg et al. 1996; Cattaneo 1999). In the saturated state, the kurtosis does not depend on Pr_m (Fig. 11b). Furthermore, while B_{rms} is not Pr_m independent for finite values of Pr_m (Fig. 14), the pdf of B/B_{rms} is the same for all Pr_m.

For $B \ll B_{\mathrm{rms}}$, the pdf is power-like, $P(B) \sim B^{1.7\ldots 1.8}$, and unchanged from the kinematic regime (see § 3.4.3 and Fig. 12b). This tail is made up of the weak fields in the bends of the folds. As we argued in § 4.1 in the context of the curvature distribution, these fields remain quasi-kinematic, with no significant change in their statistics compared to the kinematic regime.

4.5. *Summary of the Saturated State*

We now summarize what we have learned about the saturated state of the dynamo in the viscosity-dominated regime:

1. The folded field structure inherited from the kinematic regime is preserved: magnetic fields remain organized in flux
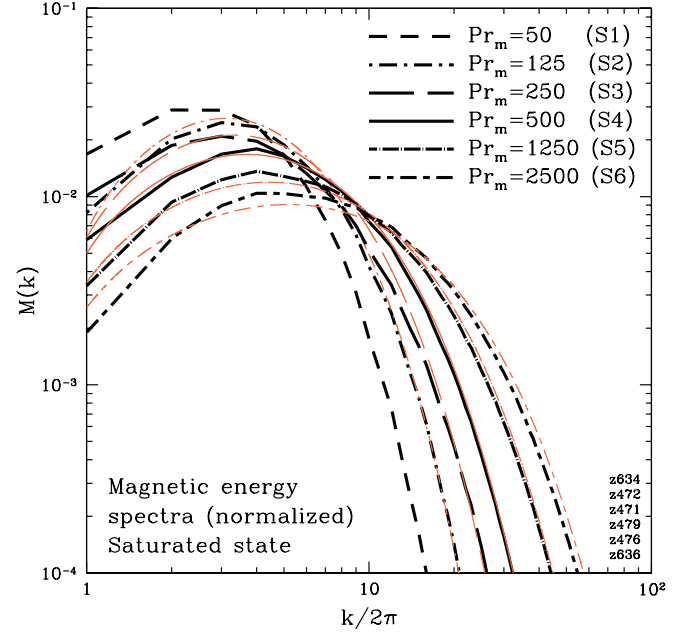

FIG. 20.—Magnetic energy spectra (normalized by the total magnetic energy) in the saturated state. The thin red lines are spectra predicted by our model. For run S1, the model does not give energy growth, but Pr_m in this case is too small for any asymptotic consideration to be applicable.

sheets (or ribbons) with alternating field direction, and field strength and field-line curvature are anticorrelated. The scale separation between the fold length (flow scale) and the direction-reversal scale (resistive scale) is $\mathrm{Pr}_m^{1/2}$.

2. The velocity field in the subviscous scale range ($k > k_\nu$) develops a k^{-4} spectrum, which is induced by the subviscous fluctuations of the Lorentz tension force and plays no part in the nonlinear back-reaction.

3. The saturated magnetic energy spectrum is flatter than in the kinematic case, but the bulk of the energy is still at the resistive scale. Accessible numerical resolutions do not allow us to measure the spectral exponent. However, the numerically obtained spectra are in an excellent agreement with those predicted for the same values of Pr_m by a simple saturation model, which, in the limit of very large Pr_m, would give a very flat positive exponent. This model is based on the idea that the nonlinear saturation is achieved via anisotropization of the velocity gradient statistics with respect to the local direction of the folds. The anisotropization consists in a reduction of the stretching component of the flow compared to its mixing component. The saturated spectra result from a balance between the weakened stretching and the mixing of the fields by quasi–two-dimensional interchange-like motions.

4. The fields in the saturated state are somewhat more tightly packed than in the kinematic regime but are still intermittent: instead of a lognormal pdf, they have an exponential one. Unlike in the kinematic case, the volume-filling fraction is independent of Pr_m.

5. SMALL-SCALE DYNAMO IN TURBULENCE WITH LARGE REYNOLDS NUMBERS

Up to this point, we have not, in fact, attempted to study the turbulent dynamo in the proper sense. Because of the large viscosity, our velocity was spatially smooth and single scale. The only feature that distinguished our model from synthetic dynamos in prescribed flows (such as those reviewed in
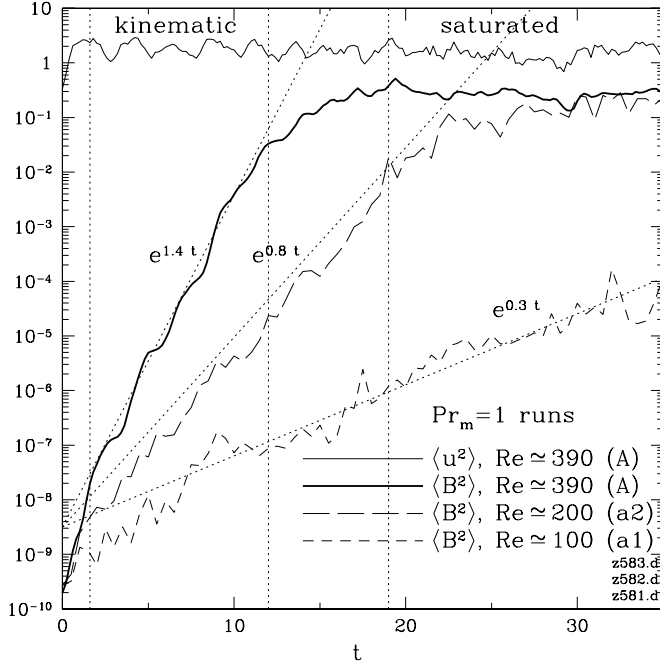
FIG. 21a

FIG. 21b

FIG. 21.—Growth and saturation of the magnetic energy for (a) $Pr_m = 1$ runs (run a1 saturates around $t = 50$, not shown) and (b) run B.
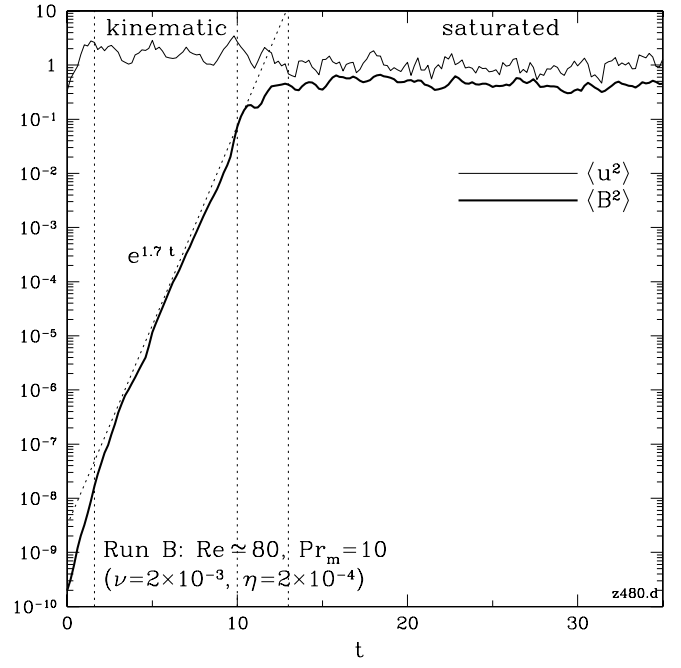
Childress & Gilbert 1995) was that our velocity was random in time (because of the random forcing), homogeneous in space (had no fixed spatial features such as stagnation points), and subject to the physical nonlinear back-reaction associated with the Lorentz tension term in equation (1). The main motivation for dwelling on this regime at such length was that a parameter scan in Pr_m could be afforded within accessible resolutions. However, if the small-scale dynamo theory is to make statements about physical reality, its ultimate goal must be to understand small-scale dynamo in turbulent velocity fields with large Reynolds numbers. In other words, we must attack the problem of *isotropic MHD turbulence*.

This problem is essentially distinct from the more studied anisotropic case in which a strong mean field is imposed on the system. The latter case is somewhat better understood, mostly because we have what is probably a correct heuristic view of it as a turbulence of interacting Alfvén wave packets (due to Kraichnan 1965), just as our intuition about Kolmogorov turbulence is based on the idea of the constitutive fluid motions as "eddies" (note, however, that the more recent and increasingly widely accepted phenomenology of Goldreich & Sridhar 1995 with its idea of critical balance has blurred the distinction between Alfvén wave packets and eddies).

It is the presence of the mean field that makes Alfvén waves possible. If no mean field is imposed, it is tempting to assume that we are still dealing with Alfvén waves, except now waves at small scales see the outer-scale magnetic fluctuations as the local mean field, along which these waves can propagate. However, in order for such a scheme to work, the outer-scale fluctuations must be more energetic than the small-scale ones, i.e., the bulk of the magnetic energy must be self-consistently kept at large (box) scales by some nonlinear mechanism. We are about to see that this does not happen (§ 5.1.2).

Resolution constraints do not permit a meaningful parameter scan in the large-Re and large-Pr_m regime, so we limit our discussion to two representative runs at the 256^3 resolution: run A is

a traditional $Pr_m = 1$ run with $\nu = 5 \times 10^{-4}$, while run B has $Pr_m = 10$ and $\nu = 2 \times 10^{-3}$. Let us define the Reynolds number as

$$ Re = \frac{\langle u^2 \rangle^{1/2}}{\nu k_0}, \qquad (60) $$

where $k_0 = 2\pi$ is the box wavenumber. Then in the saturated (kinematic) stage we have $Re \simeq 390$ (450) for run A and $Re \simeq 80$ (100) for run B. The corresponding values of the Taylor-microscale Reynolds number defined by

$$ Re_\lambda = \frac{(\langle u^2 \rangle/3)^{1/2}\lambda}{\nu} = \left(\frac{5}{3}\right)^{1/2}\frac{\langle u^2 \rangle^{1/2}}{\nu k_\lambda} \qquad (61) $$

(see Frisch 1995 and eq. [16]) are $Re_\lambda \simeq 155$ (116) for run A and $Re_\lambda \simeq 45$ (50) for run B. In a few instances, we shall compare run A with two other $Pr_m = 1$ runs (a1 and a2; see Table 1) that have lower Re. None of these runs are truly asymptotic in either Pr_m or Re, so we do not attempt to extract scalings and all our conclusions are tentative.

Note that even in the case of $Pr_m = 1$ (Fig. 21a), the resolution constraints for isotropic MHD are more severe than for purely hydrodynamic simulations because (1) the resistive scale is smaller than the viscous scale (see Figs. 22a and 23a) and (2) in order to achieve statistical steady state and collect adequate statistical information, simulations must be run for tens of box crossing times, not just one or two as in the hydrodynamic case. The highest resolution simulation of incompressible isotropic MHD to date is a 1024^3 one with $Re \simeq 960$ and $Pr_m = 1$ by Haugen et al. (2003), who were able to run it for a few box crossing times. It appears, however, that even larger resolutions and $Pr_m \gg 1$ runs are needed to make statements about the truly asymptotic case.

In § 5.1 we describe the growth, saturation, and spectra of the magnetic energy in runs A and B on a purely factual level.
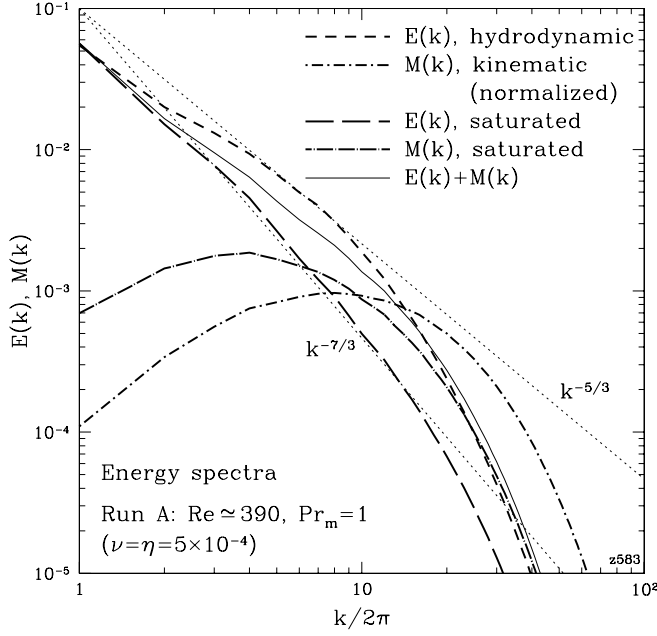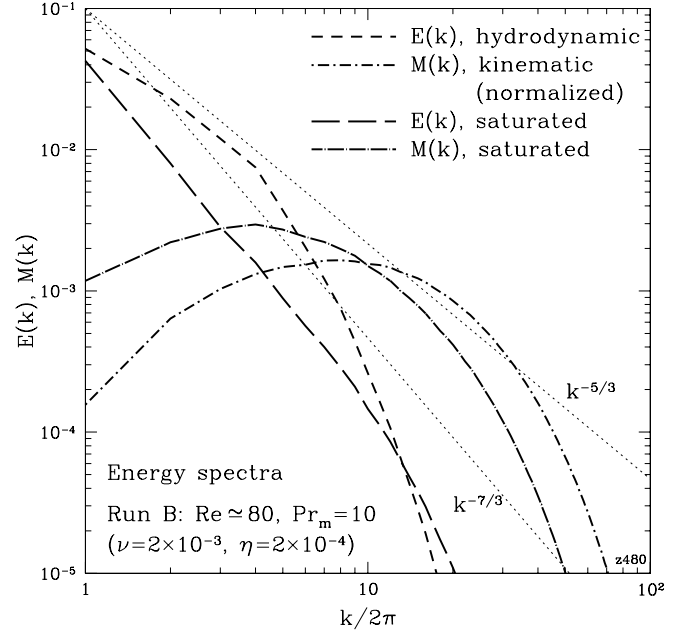
FIG. 22a

FIG. 22b

FIG. 22.—Energy spectra for (a) run A and (b) run B in the kinematic regime and in the saturated state. The magnetic energy spectra in the kinematic regime are normalized by the total magnetic energy, then averaged and rescaled by the total magnetic energy of the saturated state (for comparison with the saturated spectra).

A theoretical discussion is given in § 5.2. In § 5.3 we return to the numerical results to test our theoretical arguments and to make some tentative conclusions (§ 5.3.5). Intermittency is studied in § 5.4. The summary of the main results is in § 7.

5.1. Growth, Saturation, and Energy Spectra: Facts

5.1.1. The Kinematic Regime

The small-scale kinematic dynamo in the large-Pr_m limit depends very little on the particulars of the velocity field (as

long as this velocity is three-dimensional and sufficiently chaotic). As seen below, all indications are that our runs A and B are nonasymptotic cases of the large-Pr_m regime; i.e., the same stretching and folding mechanism is responsible for the small-scale field generation. In their kinematic stage, these runs are, therefore, very similar to the viscosity-dominated simulations.

Both runs exhibit exponential magnetic energy growth in the kinematic regime (Fig. 21). In Kolmogorov turbulence, small eddies turn over faster than the large ones, so dominant
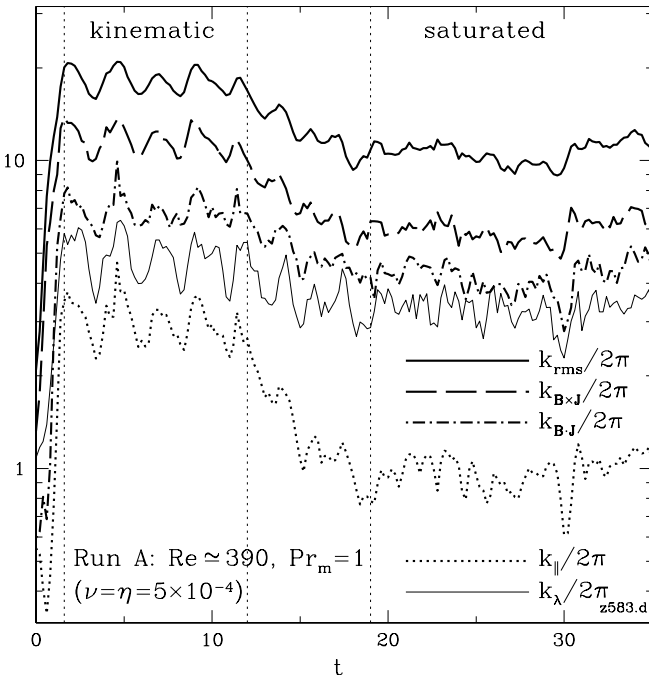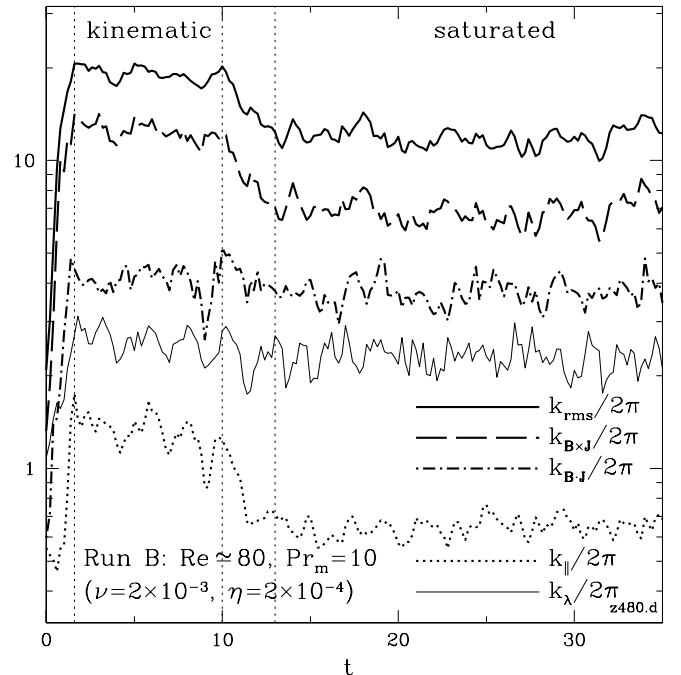

FIG. 23a

FIG. 23b

FIG. 23.—Evolution of characteristic wavenumbers (defined in § 3.2.1) for (a) run A and (b) run B. Note that for Kolmogorov turbulence, $k_\lambda \sim Re^{-1/4} k_\nu$.

TABLE 2
TIMESCALES AND ENERGY RATIOS

Run	Re	τ_{box}^{-1}	Γ_{rms}	γ	$\langle B^2 \rangle / \langle u^2 \rangle$
a1	110	1.3	5.6	0.30	0.037
a2	210	1.3	7.7	0.79	0.12
A	450	1.4	11	1.4	0.16
B	100	1.2	5.3	1.7	0.43
S4	2.0	0.64	1.1	0.53	0.92

stretching is done by the viscous eddies. We expect, therefore, that the growth rate is $\gamma \sim \Gamma_{\text{rms}}$ when $\text{Re} \gg 1$, where $\Gamma_{\text{rms}} = (\langle |\nabla \boldsymbol{u}|^2 \rangle / 15)^{1/2}$ is the rms rate of strain. Since $\nu \langle |\nabla \boldsymbol{u}|^2 \rangle = \epsilon = 1$ (eq. [4]), we have $\Gamma_{\text{rms}} \sim \text{Re}^{1/2} \tau_{\text{box}}^{-1}$, where $\tau_{\text{box}} = \langle u^2 \rangle^{-1/2}$ is the box crossing time (the box size is 1). In principle, to check these statements, we need an Re parameter scan at constant large Pr_m. While this is not possible at current resolutions, $\text{Pr}_m = 1$ runs can be used to establish qualitatively that γ increases with Re. In Table 2 we give values of γ (least-squares fit; see also Fig. 21a), Γ_{rms}, and τ_{box}^{-1} for run A and for two extra runs with $\text{Pr}_m = 1$ and smaller Re. For comparison, we also include the data for runs B and S4. Even though the numerical values of γ are substantially smaller than Γ_{rms} (and might appear, misleadingly, to be closer to τ_{box}^{-1}), it is clear that both Γ_{rms} and γ grow with Re, while τ_{box}^{-1} stays the same. The smallness of the values of γ relative to the rms rate of strain should probably be attributed to the resistive correction being order unity for $\text{Pr}_m = 1$ and moderate values of Re_m in our runs (see eq. [12]).

It is fair to observe that the increase of γ with Re that we see has, in fact, two causes: the growth of the rate of strain with Re and the increasing value of Re_m. Indeed, in run a1, $\text{Re}_m \simeq 100$ is quite close to the critical value $\text{Re}_{m,c}$, below which there is no dynamo: this is demonstrated by run a0 (Table 1), which has $\text{Re}_m \simeq 52$ and decays [this implies $\text{Re}_{m,c} \in (52, 100)$, which is the same estimate as that for the viscosity-dominated runs; see § 3.1]. The effect of finite Re_m on the value of γ will saturate at large Re_m, while the large-Re asymptotic should be $\gamma \sim \text{Re}^{1/2}$. The values of Re in our runs are not large enough for us to be able to make statements about scalings. Simulations at larger Re appear to be consistent with the scaling $\gamma \sim \text{Re}^{1/2}$ (N. E. Haugen 2003, private communication).

In both runs A and B, the magnetic energy, initially at the box scale, is quickly piled up the resistive scale, just as in the viscosity-dominated case. The evolution of the spectra is again self-similar (analogous to Fig. 4a). The normalized spectra averaged over the kinematic regime are shown in Fig. 22.

5.1.2. The Saturated State

The dynamo eventually saturates and a statistical steady state is achieved (Fig. 21). The kinetic energy $\langle u^2 \rangle$ in this regime is smaller than in the purely hydrodynamic case ($\boldsymbol{B} = 0$). The magnetic energy $\langle B^2 \rangle$ is smaller than $\langle u^2 \rangle$ by a factor of 6 in run A and by a factor of ~ 2.3 in run B (Table 1). The saturated spectra (Fig. 22) exhibit no scale-by-scale equipartition between the kinetic and magnetic energies even at $\text{Pr}_m = 1$.

In both runs A and B, the kinetic energy spectrum in the purely hydrodynamic regime has a very short segment consistent with the Kolmogorov $k^{-5/3}$ scaling (this is somewhat better pronounced for run A). In the nonlinear saturated MHD state, the spectrum is steeper: in each of the runs, there is a

segment best fitted by $k^{-7/3}$. It is not clear if this scaling (if it is really there) survives in the large-Re limit or is simply a limited-resolution effect (spectra steeper than Kolmogorov sometimes appear in hydrodynamic simulations with too large viscosity; see theoretical discussion in Frisch 1995). If this scaling is, in fact, asymptotic in Re, it is a feature of the fully developed isotropic MHD turbulence for which, at present, we have no theoretical explanation (see some further observations in § 5.2). What is certainly true is that (1) the kinetic energy is dominated by the large (box) scales and (2) the characteristic "eddy" time $\sim [k^3 E(k)]^{1/2}$ peaks at the viscous scale.

The magnetic energy spectrum is shifted toward small (resistive) scales, with a substantial excess of magnetic over kinetic energy there. There is no discernible scaling. Note that the shapes of the magnetic energy spectra in runs A, B, and S1–S6 (Fig. 20) are not very different. Thus, it appears that there is no inverse cascade of magnetic energy and that the characteristic scale of the magnetic field is the resistive scale.

The fact that numerical simulations do not support equipartition was first explicitly emphasized by Maron et al. (2004), even though many prior numerical studies had found similar spectra (Meneguzzi et al. 1981; Kida et al. 1991; Miller et al. 1996; Cho & Vishniac 2000; Chou 2001). However, there was a reluctance to accept that numerical evidence was at odds with the equipartition hypothesis and, therefore, with the standard Alfvénic phenomenology. In order to extract scalings, a popular device (due originally to Kida et al. 1991) has been to consider the spectrum of the total energy, $E(k) + M(k)$. In our opinion, this choice of diagnostic obscures rather than clarifies the situation. Indeed, it only makes sense to add the spectra together if there is a symmetry between $\boldsymbol{u}$ and $\boldsymbol{B}$. For the spectra that obtain for $\text{Pr}_m = 1$ and at limited resolutions, adding $E(k)$ and $M(k)$ gives one what might be a false impression that a Kolmogorov scaling actually emerges, as shown in Figure 22a. However, without equipartition, there is no obvious reason why asymmetric kinetic and magnetic energy spectra should add up to something that has a Kolmogorov scaling.

One could argue that all current simulations are non-asymptotic and that, were the resolution to be increased dramatically, equipartition and Kolmogorov scaling would emerge at hitherto inaccessible small scales. While this cannot be ruled out, the indications so far are not encouraging. Haugen et al. (2003, 2004) performed simulations at resolutions ranging from 64^3 to 1024^3 (with $\text{Pr}_m = 1$ and maximum $\text{Re} = 960$). In none of their runs were the kinetic and magnetic energies in scale-by-scale equipartition, with magnetic energy always shifted toward the small scales. Furthermore, they found that the Kolmogorov scaling that seemed to hold at 256^3 (cf. Fig. 22a) actually got worse at 1024^3, with magnetic energy bulging up at small scales. They attributed this problem to some form of the bottleneck effect, i.e., essentially, to nonlocal interactions in k space. Small-scale dynamo is, in fact, just that: a nonlocal interaction between velocity and magnetic fields.

A Kolmogorov scaling for the total energy was also reported by Biskamp & Müller (2000), who simulated *decaying* isotropic MHD turbulence with $\text{Pr}_m = 1$ at resolutions of 512^3. It is, however, unlikely that decaying MHD results apply to the forced case. Indeed, the kinetic and magnetic energy spectra that Biskamp & Müller (2000) found in their self-similarly decaying regime were quite different from those for the forced case: while again there was no equipartition, it was the magnetic energy that dominated the kinetic one at large scales (we presume that this is due to large-scale MHD equilibrium structures).

Thus, on the balance of the available numerical results, while we cannot definitively claim that the equipartition theory is wrong, it is certainly true that there is no evidence in support of it and a fairly strong case against.

5.2. *The Physics of Saturation: Selective Decay, Alfvén Waves, and Mixing*

Let us consider what are the reasonable physical scenarios of nonlinear transition from field growth (dynamo) to saturation and what they imply about the final state.

5.2.1. *The Intermediate Nonlinear Regime*

The folded field structure implies the criterion for the onset of nonlinearity: the back-reaction is controlled by the Lorentz tension force $\mathbf{B} \cdot \nabla \mathbf{B} \sim k_\parallel B^2$, which only depends on the parallel gradient of the field and does not know about direction reversals ($k_\parallel \sim k_\nu$). Balancing $\mathbf{B} \cdot \nabla \mathbf{B} \sim \mathbf{u} \cdot \nabla \mathbf{u}$, we find that back-reaction is important when magnetic energy becomes comparable to the energy of the viscous-scale eddies. Eddies at scales above viscous are still more energetic than the magnetic field and continue to stretch it at their (slower) turnover rate. When the field energy reaches the energy of these eddies, they are also suppressed and the dominant remaining stretching is done by yet larger and slower eddies. Consider a time t when the total magnetic energy $\langle B^2 \rangle(t)$ is less than its final saturation value but larger than the energy of the viscous-scale eddies. Let the stretching scale $l_s(t)$ be the scale of the eddies whose energy is equal to $\langle B^2 \rangle$, i.e.,

$$u_{l_s}^2 \sim \langle B^2 \rangle. \tag{62}$$

All eddies smaller than l_s have had their stretching component suppressed, while all the larger eddies are slower, so, at time t, the effective rate at which the field is being stretched is u_{l_s}/l_s. Using this and equation (62), we estimate

$$\frac{d}{dt} \langle B^2 \rangle \sim \frac{u_{l_s}}{l_s} \langle B^2 \rangle \sim \frac{u_{l_s}^3}{l_s} \sim \epsilon = \text{const}, \tag{63}$$

where ϵ is the Kolmogorov energy flux. Equation (63) implies $\langle B^2 \rangle(t) \sim \epsilon t$; i.e., there is an intermediate period of nonlinear evolution between the onset of nonlinearity and saturation, during which the magnetic energy grows proportionally to time rather than exponentially. The force balance underpinning the back-reaction by the folded fields on the eddies of size l_s is

$$\mathbf{u} \cdot \nabla \mathbf{u} \sim \frac{u_{l_s}^2}{l_s} \sim \mathbf{B} \cdot \nabla \mathbf{B} \sim k_\parallel \langle B^2 \rangle, \tag{64}$$

so that $k_\parallel \sim l_s^{-1}$, i.e., the folds are elongated to the stretching scale (for a slightly more quantitative argument in favor of fold elongation, see Schekochihin et al. 2002b).

The key question is by how much l_s can exceed the viscous scale l_ν, for it is the saturated value of l_s that will determine the saturated magnetic energy and its spectral distribution. Saturation is achieved when the nonlinear growth according to equation (63) is balanced by diffusion:

$$\frac{u_{l_s}}{l_s} \sim \frac{\eta}{l_\eta^2}. \tag{65}$$

Therefore, in order to determine l_s, we need to know what happens to the resistive scale l_η in the nonlinear regime. There are two main possibilities (subject to the caveats in § 6.1).

5.2.2. *Saturation with Efficient Mixing*

If the velocities at $l < l_s$ act as interchange-like motions in the plane transverse to the local direction of the folds and, consequently, mix the field lines in a quasi–two-dimensional fashion, then the resistive scale is determined by the characteristic timescale of these motions *at the viscous scale*,

$$\frac{\eta}{l_\eta^2} \sim \frac{u_{l_\nu}}{l_\nu}. \tag{66}$$

Comparing this with equation (65), we see that l_s cannot grow larger than l_ν by more than a factor of order unity. In this case, the motions at or just above the viscous scale are anisotropized, so mixing is enhanced and wins the competition with stretching, leading to saturation. The magnetic energy saturates at a value determined by the energy of the viscous-scale eddies. Thus, the signature of this type of saturation would be the following dependence of the saturated magnetic energy on Re:

$$\langle B^2 \rangle \sim u_{l_\nu}^2 \sim \text{Re}^{-1/2} \langle u^2 \rangle. \tag{67}$$

5.2.3. *Saturation with Inefficient Mixing*

The second possibility is that mixing by motions at $l < l_s$ is inefficient, so that both stretching and mixing of the field is mostly done by the stretching-scale eddies. It is then the turnover time of these eddies that determines the resistive scale of the magnetic fields, giving (from eqs. [65], [62], and [63])

$$l_\eta \sim \left(\frac{\eta l_s}{u_{l_s}} \right)^{1/2} \sim (\eta t)^{1/2}. \tag{68}$$

Physically, this expression describes selective decay of the magnetic energy at scales too small to be sustainable by the weakened stretching (or mixing). In this scenario, the magnetic energy is free to grow to the equipartition level,

$$\langle B^2 \rangle \sim \langle u^2 \rangle, \tag{69}$$

at which point $l_s \sim l_0$ and the resistive scale is determined by the stretching rate of the outer-scale eddies:

$$l_\eta \sim \left(\frac{\eta l_0}{u_{l_0}} \right)^{1/2} \sim \text{Re}_m^{-1/2} l_0 \sim \text{Re}^{1/4} \text{Pr}_m^{-1/2} l_\nu, \tag{70}$$

i.e., it is larger by a factor of $\text{Re}^{1/4}$ than in the kinematic regime. Note that the condition for l_η to be distinguishably smaller than l_ν in a numerical experiment is, therefore,

$$\text{Pr}_m \gg \text{Re}^{1/2} \gg 1, \tag{71}$$

which is impossible to satisfy at present resolutions. Since the folds elongate so that $k_\parallel \sim l_s^{-1} \sim l_0^{-1}$ (§ 5.2.1), the separation between the direction-reversal scale and the fold length increases:

$$\frac{k_\eta}{k_\parallel} \sim \frac{l_0}{l_\eta} \sim \text{Re}^{1/2} \text{Pr}_m^{1/2}, \tag{72}$$

which is a factor of $\text{Re}^{1/2}$ larger than in the kinematic regime.
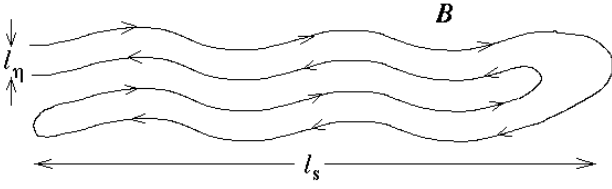
FIG. 24.—Alfvén waves along folded fields: a sketch.

If the velocities at $l < l_s$ are not interchange-like mixing motions, what are they? There is another type of motion that does not amplify the magnetic field and can, theoretically, be present below the stretching scale: Alfvén waves can propagate along the folded direction-reversing magnetic fields (Fig. 24). These waves are damped by viscosity and make a contribution to both the kinetic and magnetic energy spectra. Their dispersion relation is $\omega^2 = \boldsymbol{kk}:\hat{\boldsymbol{b}}\hat{\boldsymbol{b}}\langle B^2 \rangle$ for $k_\nu \ll k \ll k_\| \sim l_s^{-1}$ (Schekochihin et al. 2002b). This interval is nonempty provided that $l_s \gg l_\nu$. Therefore, mixing must be inefficient in a turbulence made up of such waves: otherwise, l_s cannot grow sufficiently far above l_ν for them to exist in the first place.

Detecting these Alfvén waves in numerical simulations is a considerable challenge both because of large scale separations that must be resolved and because designing the appropriate diagnostics is not straightforward. The simulations we present here are not appropriate for such a task. However, some of the physical possibilities we have anticipated can be tested.

5.3. Numerical Evidence: Facts and Interpretations

5.3.1. Saturated Energy Levels

The key challenge now is the resolution of the dichotomy described in §§ 5.2.2 and 5.2.3: saturation with magnetic energy comparable to the viscous eddy energy (eq. [67]) or to the total energy of the turbulence (eq. [69]). The most direct approach would be to look at the scaling of the ratio $\langle B^2 \rangle / \langle u^2 \rangle$

with Re at constant large Pr_m, but this is not yet possible at current resolutions. At $Pr_m = 1$, $\langle B^2 \rangle / \langle u^2 \rangle$ increases with Re (Table 2). In the higher resolution Re scan with $Pr_m = 1$ produced by Haugen et al. (2003), $\langle B^2 \rangle / \langle u^2 \rangle$ appeared to saturate at larger Re. Similar results were reported in earlier numerical studies (Kida et al. 1991; Kleva & Drake 1995; Miller et al. 1996; Archontis et al. 2003b). Thus, at least for $Pr_m = 1$, numerical results do not support the scaling given by equation (67), suggesting that it is the second possibility (§ 5.2.3) that is realized.

5.3.2. The Intermediate Nonlinear Regime

We now examine the evolution of our runs A and B from the kinematic to nonlinear regimes to see if we can identify any of the features of the saturation scenarios proposed in § 5.2.

We notice immediately that, between the kinematic stage of exponential growth and the saturated statistically steady state, an intermediate nonlinear stage during which the magnetic energy grows slower than exponentially is manifest in run A and, to a lesser extent, in run B (Fig. 21). This intermediate regime was not present in the viscosity-dominated runs and is clearly a large-Re effect in agreement with the argument in § 5.2.1.

5.3.3. The Folded Structure

Employing the same diagnostics as in §§ 3 and 4, we find that the folded structure appears to survive in runs A and B despite the moderate values of Pr_m.

The time histories of the characteristic wavenumbers (defined in § 3.2.1) are shown in Figure 23. In the kinematic regime, $k_{\mathrm{rms}} \sim k_{\boldsymbol{B} \times \boldsymbol{J}} \gg k_\|$. During the intermediate nonlinear regime, $k_\|$ decreases further and becomes comparable to the box wavenumber. The resistive wavenumber k_{rms} also decreases, but by a lesser amount, which is consistent with the ideas of selective decay, fold elongation, and increased scale separation in the folds in the saturated state set forth in §§ 5.2.1 and 5.2.3 (see eq. [72]). The fold elongation is a new effect: it could not be
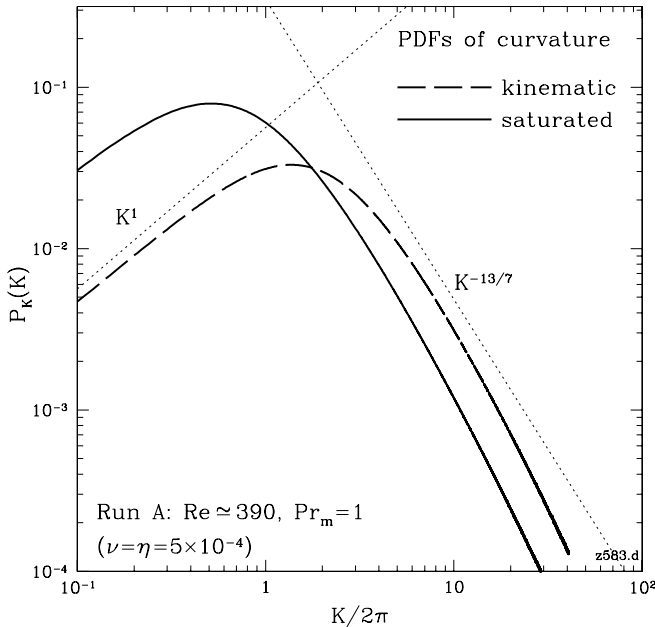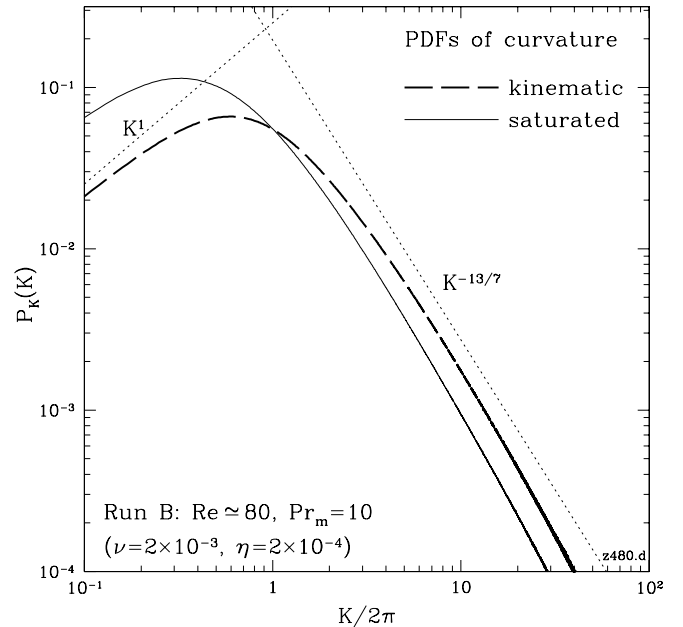

FIG. 25a

FIG. 25b

FIG. 25.—Curvature pdf's for (a) run A and (b) run B during the kinematic regime and in the saturated state. The slopes corresponding to K^1 and $K^{-13/7}$ (see eq. [32]) are given for reference.
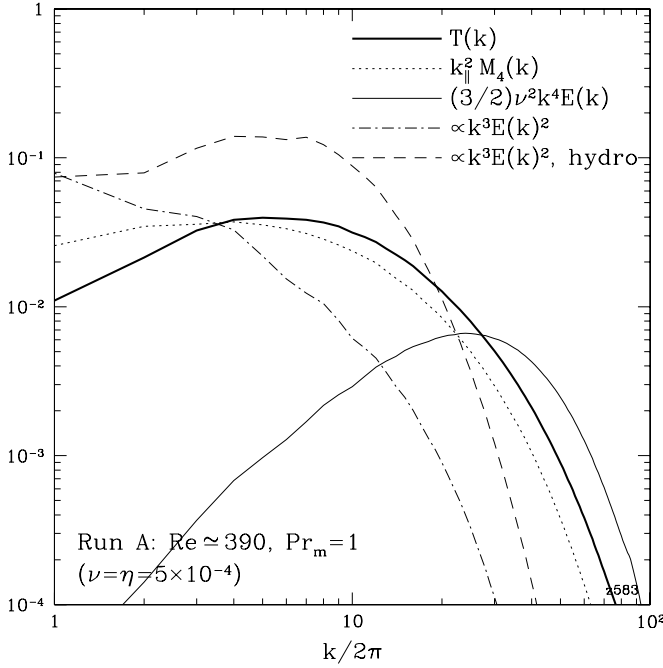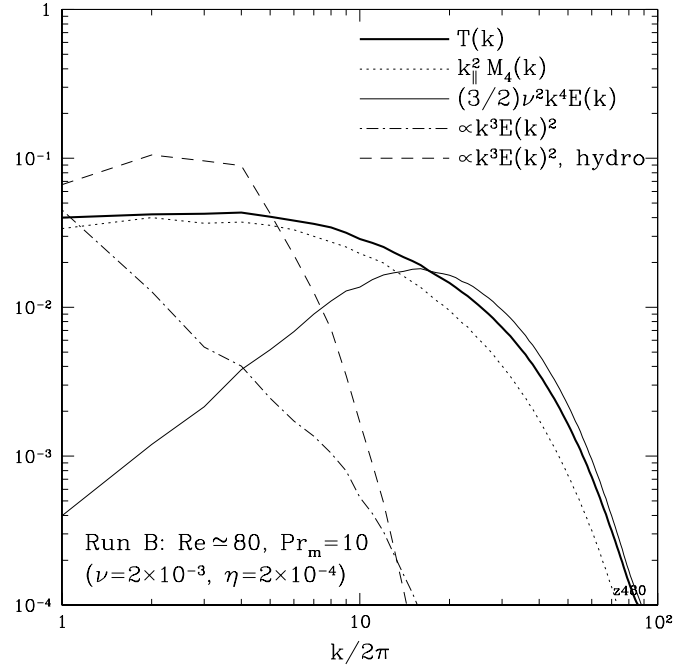
Fig. 26a

Fig. 26b

Fig. 26.—Tension spectra for (*a*) run A and (*b*) run B in the saturated state. For comparison, we also plot the kinetic energy spectrum $E(k)$ compensated by $(3/2)\nu^2 k^4$, the spectrum of B^2, multiplied by $k_\parallel^2$ (as defined by eq. [13]), and $k^3 E(k)^2$ (divided by 10) in both hydrodynamic and nonlinear MHD regimes.

seen in the viscosity-dominated runs (§ 4), for which there was no separation between the viscous and box scales.

All other features associated with the folded structure that we reported in §§ 3.2 and 4.1 for the viscosity-dominated runs carry over to runs A and B: the magnetic field strength and curvature are anticorrelated (e.g., the correlation coefficient $C_{K,B}$, eq. [26], is within 6% of -1; see Table 1) and the pdf's of curvature (Fig. 25) are again concentrated at velocity scales. The power tail appears to be somewhat steeper than $K^{-13/7}$ predicted for the large-Pr_m case (the steepening is more pronounced for run A). Interestingly, the scaling $P_K(K) \sim K$ at $K \ll k_\nu$ (to the left of the peak) suggested by equation (32) seems to be in evidence for the kinematic pdf's. The elongation of the folds in the saturated state compared to the kinematic regime is manifested by the peak of the curvature pdf shifting to the left.

5.3.4. *The Tension Spectra*

Let us now look at the magnetic back-reaction $\boldsymbol{B}\cdot\nabla\boldsymbol{B}$ as a function of k: the tension spectra for runs A and B are plotted in Figure 26. For run B, the tension spectrum is flat up to the outer (box) scale; for run A, it has a plateau that starts at $k/2\pi \sim 3$, which should probably also be interpreted as corresponding to the outer scale. Based on the argument of § 3.2.2, such flat tension spectra are consistent with magnetic fields that are folded with the characteristic fold length at the outer scale. In a further confirmation of the consistency of this view, the relation $T(k) \simeq k_\parallel^2 M_4(k)$ (eq. [23]) roughly holds (see Fig. 26).

Thus, the tension spectra in runs A and B have similar properties to those in the viscosity-dominated case (§ 4.2), except the tension force $\boldsymbol{B}\cdot\nabla\boldsymbol{B}$ is no longer passively compensated by the velocities as in equation (43): Figure 26 shows that the relation given by equation (45) is only satisfied at very small scales. Instead, in the saturated state, we expect the nonlinear balance given by equation (65) to hold at the stretching

scale l_s with velocities at $l > l_s$ remaining essentially hydrodynamic and velocities at $l < l_s$ modified so that they cannot significantly affect the folded structure, i.e., either mix or stretch the magnetic field. Since equation (65) is only an order-of-magnitude statement, it is not meaningful to compare the actual values of $\boldsymbol{u}\cdot\nabla\boldsymbol{u}$ and $\boldsymbol{B}\cdot\nabla\boldsymbol{B}$. However, it is still instructive to compare the behavior of $T(k)$ with that of $k^3 E(k)^2$, a quantity that roughly measures the spectrum of the hydrodynamic interaction term $\boldsymbol{u}\cdot\nabla\boldsymbol{u}$. In Figure 26, this quantity is plotted in both the purely hydrodynamic case and the saturated MHD state [note that the absolute magnitude of $k^3 E(k)^2$ has been rescaled in Fig. 26 and should not be compared to that of $T(k)$]. Interestingly, the intervals of flat $T(k)$ for both runs coincide with the intervals where there is a substantial suppression of $k^3 E(k)^2$ in the MHD case compared to the hydrodynamic case. These intervals correspond to the steeper than Kolmogorov scaling of the kinetic energy spectra noted in § 5.1.2. While we reiterate the caveat made in § 5.1.2 that this scaling might be an artifact of limited resolution, it is just possible that we are dealing with a genuine spectral signature of the nonlinearly modified fluid motions in the interval $k_s < k < k_\nu$.

Based on these plots, we hypothetically identify the stretching wavenumbers for our runs: for run A, $k_s/2\pi \simeq 3$; for run B, $k_s/2\pi \simeq 1$. The resistive and viscous cutoffs for these runs are all around $k/2\pi \sim 10$ and hard to tell apart in the saturated state, which is consistent with the estimates in § 5.2.3 and $\mathrm{Pr}_m \gtrsim 1$ (note that even run B does not really satisfy the condition given by eq. [71] necessary for k_ν and k_η to be distinguishable).

5.3.5. *Tentative Conclusions*

At the fairly low values of Re that our runs have, we cannot test scalings such as equations (67), (69), (70), and (72) so as to make a definite distinction between the two scenarios of saturation (§ 5.2.2 vs. § 5.2.3). On the qualitative level,
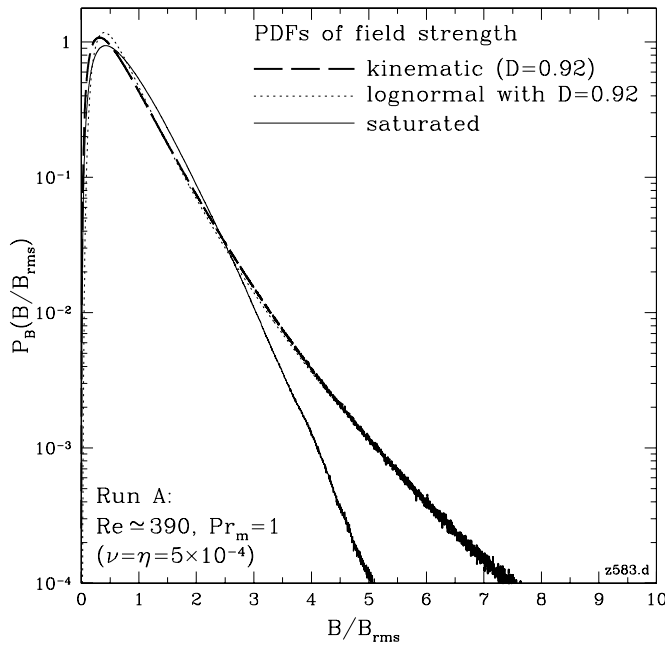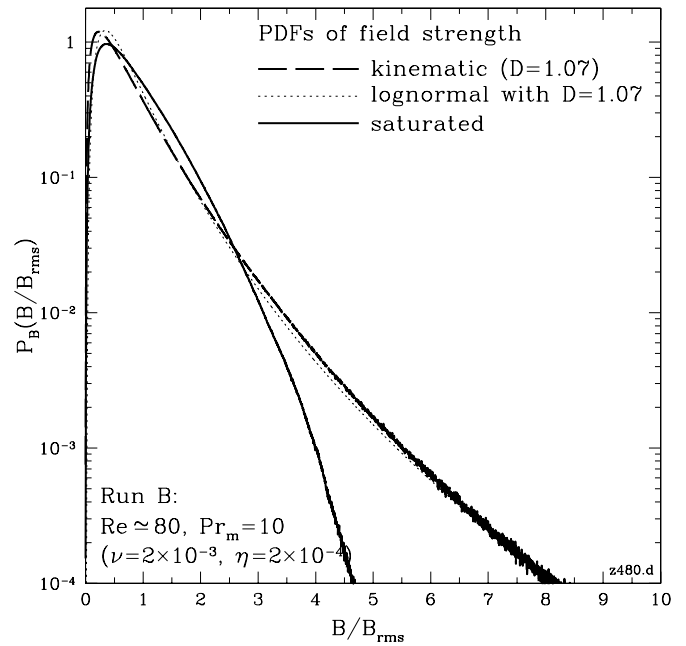
FIG. 27.—The pdf's of B/B_{rms} for (a) run A and (b) run B averaged over the kinematic stages of these runs and the corresponding lognormal profiles (eq. [42]) with the same D. The pdf's in the saturated state are also given.

however, our results appear to favor the second scenario: (1) increase of the ratio $\langle B^2\rangle/\langle u^2\rangle$ with Re, (2) the presence of an intermediate nonlinear regime, (3) the evolution of the characteristic wavenumbers (selective decay and fold elongation), (4) the evidence of the folded structure up to the box scale (curvature pdf's, anticorrelation between curvature and field strength, flat tension spectra), and (5) the nonlinear modification of the kinetic energy spectra up to the box scale are all consistent with the conclusion that the stretching scale in saturation is comparable to the outer scale, not the viscous scale,[13] as suggested in § 5.2.3. In this second scenario of saturation, the velocities at scales below $l_s \sim l_0$ do not destroy the folded direction-reversing magnetic fields. The magnetic fluctuations are of two kinds: the folds of length l_0 with direction reversals at l_η (eq. [70]) and (hypothetically) Alfvén waves propagating along the folds with k in the inertial range (§ 5.2.3). The dynamo is saturated at an energy that is comparable to $\langle u^2\rangle$.

The mechanism of this saturation should be entirely controlled by what happens at the outer scale. Since the motions at this scale are directly excited by the forcing, the nonlinear dynamics there may not be totally dissimilar from the nonlinear dynamics in the viscosity-dominated case. In other words, we might conjecture that saturation results from a competition of weakened stretching and enhanced mixing *at the outer (forcing) scale* (the hypothesis that the dynamo saturation is controlled by the outer timescale was first explicitly formulated by Maron et al. 2004).

In § 4.3 we constructed a quantitatively successful model of saturation in the viscosity-dominated case by assuming

that velocity gradients are partially anisotropized, leading to weakened stretching but unsuppressed mixing. Since the viscosity-dominated runs have Re ~ 1, the stretching scale is the box scale, $l_s \sim l_0$, which is also the viscous scale, $l_0 \sim l_\nu$, so the success of this model cannot be construed to favor either of the saturation scenarios outlined in § 5.2. The fact that the mixing rate did not have to be suppressed in order for correct results to be obtained is consistent with both the scenario of efficient mixing of the field by the eddies at the viscous scale l_ν and the idea that the saturated state is controlled by the balance between mixing and stretching at the box scale l_0.

The reader is referred to § 6.1.2 for some further caveats.

5.4. Intermittency

We complete our standard set of diagnostics by looking at the pdf's of the magnetic field strength in runs A and B.

In the kinematic regime, their evolution is again self-similar with the pdf's of B/B_{rms} collapsing onto stationary profiles (similarly to Fig. 12). These profiles (averaged over the kinematic stages of the runs) are shown in Figure 27. The lognormal fit (eq. [42]) works even better for these runs than it did for the viscosity-dominated case in § 3.4.3 (Fig. 13).

The intermittency is reduced in the saturated state: the evolution of the normalized moments is analogous to the viscosity-dominated case (Fig. 11a) with the values of kurtosis in the saturated state still super-Gaussian, but substantially smaller than in the kinematic regime (see Table 1). On a semilog plot, the pdf's in the saturated state of both runs (Fig. 27) have straight segments in the region of strong fields (exponential tails). However, at even larger B, there appears to be a knee followed by steeper decay. To a lesser extent, the same feature was also present in the viscosity-dominated case (Fig. 13). We believe that this feature might be due to resolution effects and/or insufficient averaging (as these values of B correspond to very rare events), so the physical pdf at large B is exponential.

---

[13] In principle, it is not excluded that the stretching scale l_s saturates at some Re-dependent value intermediate between l_0 and l_ν. In fact, one might consider the fact that k_s appears to be somewhat larger than the box wavenumber in run A suggestive of such an outcome. Much higher resolutions are necessary to test this possibility. However, the scale invariance of the inertial range makes saturation with $l_0 \ll l_s \ll l_\nu$ a priori unlikely.

Note that exponential pdf's of the magnetic field strength were reported previously in $\mathrm{Pr}_m \gtrsim 1$ simulations of compressible convection with rotation (Brandenburg et al. 1996) and of Boussinesq convection (Cattaneo 1999). Thus, exponential tails of the field strength pdf appear to be a fairly universal feature in MHD turbulence (at least away from the boundaries; see Cattaneo 1999; Thelen & Cattaneo 2000).

6. DISCUSSION

6.1. *Are All Small-Scale Dynamos Large-*Pr_m *Dynamos?*

The fundamental mechanism of magnetic energy generation by three-dimensional chaotic and/or random flows (due to Zel'dovich et al. 1984) is based on the idea that the structure of a locally uniform rate-of-strain tensor in three dimensions allows for a winning configuration of magnetic fields: the field aligns with the stretching direction of the flow but varies (reverses) along the "null" direction, so that compression cannot cancel the effect of stretching (see § 3.3). Thus, the folded structure, which has been the leitmotif of this paper, is an essential ingredient in our understanding of the very existence of the dynamo.

The Zel'dovich et al. (1984) mechanism is universal in the sense that the particulars of the flow matter little. However, two properties are essential: (1) the flow must be spatially smooth, and (2) the magnetic field must be able to vary at scales much smaller than the scale of the flow. Only if these conditions are satisfied can one think of the flow as locally linear and make the above inferences about the growing field's structure. The turbulent dynamo with large Pr_m satisfies these conditions and so do all deterministic chaotic dynamos (see reviews by Childress & Gilbert 1995; Ott 1998). The small-scale dynamo, as usually understood in the literature (this paper included), is the large-Pr_m dynamo.

A smooth random flow is not, strictly speaking, turbulence. Turbulent motions at scales above the viscous cutoff are spatially rough and cannot be approximated by a linear velocity field (locally uniform rate of strain). To what extent then is the Zel'dovich et al. (1984) mechanism applicable to physical systems and numerical simulations in which Pr_m is not large?

6.1.1. *Suppression of Small-Scale Dynamo at Low* Pr_m

A natural way to approach this issue is to consider the opposite limit: $\mathrm{Pr}_m \ll 1$ (but Re and Re_m are still large). In this case, the resistive scale is in the hydrodynamic inertial range and the dominant interaction is between velocities and magnetic fields at that scale. Is there a dynamo in such a case?

There currently is no physical understanding of the low-Pr_m dynamo: the standard heuristic argument involving stretching, turbulent diffusion, and resistive diffusion fails to produce an unambiguous prediction about the viability of the dynamo because all these effects are of the same order and the outcome of their competition is a quantitative, rather than a qualitative, issue. A number of simulations found in various MHD contexts that dynamo shuts down when Pr_m is too small (Nordlund et al. 1992; Brandenburg et al. 1996; Nore et al. 1997; Christensen et al. 1999; Maron et al. 2004; Schekochihin et al. 2004a; Haugen et al. 2004). In particular, in Schekochihin et al. (2004a), we studied this problem using the same code and the same numerical setup as in this paper and found that dynamo at low Pr_m is shut down even though the magnetic Reynolds number Re_m is the same as for successful dynamos with $\mathrm{Pr}_m \geq 1$. We identified two possible interpretations: either a nonhelical small-scale dy-

namo with low Pr_m does not exist at all, or the critical Re_m for such a dynamo is much larger than for the case of $\mathrm{Pr}_m \geq 1$ and cannot be resolved (cf. Rogachevskii & Kleeorin 1997; Boldyrev & Cattaneo 2004).

If a low-Pr_m dynamo does exist, what is the structure of the magnetic fields generated by it? The Zel'dovich et al. (1984) mechanism does not apply: we cannot have folded fields as there is no field flow scale separation necessary to maintain them. Thus, the question is whether the large-Pr_m dynamo is the only kind of nonhelical small-scale dynamo or there exists yet another, as yet unexplored, variety.

6.1.2. *Small-Scale Dynamo at* $\mathrm{Pr}_m \sim 1$

Resolving this issue is important for interpreting the simulations with $\mathrm{Pr}_m \sim 1$. It is clear that the *kinematic* dynamo in such runs is of the large-Pr_m kind: we have seen that all the main features of the viscosity-dominated runs carry over to the case of $\mathrm{Re} \sim 10^2$ and $\mathrm{Pr}_m \gtrsim 1$ (the scale separations such as $k_{\mathrm{rms}} k_\parallel$ change smoothly as a transition from viscosity-dominated large-Pr to turbulent $\mathrm{Pr} \sim 1$ regime is made; see Schekochihin et al. 2004a). This dynamo is driven by the viscous-scale eddies, and whatever the inertial range velocities might do is guaranteed to happen at a slower rate. However, when the stretching component of the viscous-scale eddies is nonlinearly suppressed, it is crucial to know if the inertial range velocities that take over can also generate magnetic field *at their own scale*. The heuristic saturation scenarios proposed in § 5.2 were based on treating these velocities simply as larger eddies acting on the magnetic field the same way as the viscous eddies did. This description is incomplete if there exists a second kind of small-scale dynamo generating magnetic fields in the inertial range. In the latter case, the $\mathrm{Pr}_m \sim 1$ simulations are in a mixed regime containing both the folded fields resulting from large-Pr_m–type dynamo and some other kind of magnetic fluctuations generated by the hypothetical inertial range dynamo (plus, possibly, the Alfvén-like waves discussed in § 5.2.3).

The two alternative scenarios of saturation described in § 5.2 and interpretations of the numerical results in favor of either are, thus, qualified by the above discussion.

6.2. *Large-*Pr_m *Dynamo in Three Dimensions versus the Two-Dimensional Case*

Small-scale magnetic fields in the large-Pr_m regime were previously studied numerically in two dimensions by Kinney et al. (2000). Since the frozen-in property of the field lines holds equally well in two and three dimensions, the folded structure in two dimensions looks very similar to the folded structure in three dimensions. Such features as disparity between parallel and transverse scales of the field variation, power-like tails of curvature distributions, and anticorrelation between field strength and field-line curvature are present in both cases (Kinney et al. 2000; Schekochihin et al. 2002c). The reason for such similarity is that the folded structure is an ideal effect: it is just a geometric property of the field lines arising from random stretching by the flow. Diffusion has a selection effect on the folded fields with opposite outcomes in three and in two dimensions: in three dimensions, the folds can align in such a way as to support growth of magnetic energy, in contrast to two dimensions, where stretching is always overcome by diffusion (see § 3.3). Indeed, the magnetic field in two dimensions can be written in terms of a scalar stream function, $\boldsymbol{B} = (\partial A/\partial y, \, -\partial A/\partial x)$. It is then

readily obtained that A satisfies the advection-diffusion equation (Zel'dovich 1957)

$$\partial_t A + \boldsymbol{u} \cdot \nabla A = \eta \Delta A, \qquad (73)$$

implying eventual decay of the field. However, the eventuality of decay does not preclude transient growth and even a slowly decaying nonlinear "saturation" phase, which was studied in some detail by Kinney et al. (2000). They found persistent folded structure, near-flat tension spectra, and k^{-4} spectra of the subviscous velocities induced by the tension force—results that are analogous to those of §§ 4.1 and 4.2, confirming the geometric nature of these features. The key difference is that the possibility of sustained dynamo action in three dimensions leads to a saturated nonlinear state (§ 4.3), while in two dimensions, the nonlinear state is eroded at the resistive timescale and the field is destroyed.

Another feature that arises in three dimensions, but is absent in two dimensions, is the possibility for a degree of misalignment between the reversing fields in the folds: this was measured tentatively by $k_{\boldsymbol{B} \cdot \boldsymbol{J}}$ in §§ 3.2.1 and 4.1. We noted in § 4.1 that $k_{\boldsymbol{B} \cdot \boldsymbol{J}}$ was larger in the saturated state than during the kinematic growth, perhaps indicating a transition from flux sheets to flux ribbons. There is, at present, no quantitative theory of three-dimensional magnetic structures and field alignment. We have not attempted a full-fledged numerical characterization of these features: such a study is left for future work.

6.3. Diagnosing MHD Turbulence

In this paper, the set of statistical quantities that were used to analyze numerical data was limited to three groups:

1. Energy spectra: they show energy distribution over scales but miss essential information about the structure of the field; also spectra of second-order quantities related to the Lorentz force.
2. Characteristic wavenumbers, pdf's of the field-line curvature, and correlations between the curvature and the field strength: these describe the structure of the field.
3. The pdf's and moments of the field strength: they characterize the volume filling property of the magnetic field.

All diagnostics in the last two groups (1) are of order higher than 2 in magnetic field, (2) contain magnetic field but not velocity or its correlations with magnetic field, and (3) are one point in space. That one has to go beyond second-order statistics is due to the structured and intermittent nature of the magnetic field and to the fact that magnetic back-reaction ($\boldsymbol{B} \cdot \nabla \boldsymbol{B}$) is quadratic in $\boldsymbol{B}$. Points 2 and 3 are limitations of our description of MHD turbulence and deserve some discussion.

6.3.1. Flow Statistics

The results reported in this paper are almost exclusively on the statistics of the magnetic field. However, in our discussion of back-reaction and saturation in §§ 4.3 and 5.2 we had to make conjectures about the way dynamically important magnetic fields modify the flow. The assumptions that helped us to construct a saturation model for the viscosity-dominated runs were fairly natural: thus, it is clear already from the induction equation itself that, in order to stop magnetic field from growing, the $\hat{\boldsymbol{b}}\hat{\boldsymbol{b}}$ component of the rate-of-strain tensor must be suppressed. Indeed, we do find that both $\langle \hat{\boldsymbol{b}}\hat{\boldsymbol{b}} : \nabla \boldsymbol{u} \rangle$ and $\langle |\hat{\boldsymbol{b}}\hat{\boldsymbol{b}} : \nabla \boldsymbol{u}|^2 \rangle$ decrease as the transition from the kinematic

to nonlinear regime occurs. However, in order to resolve the questions raised in § 5.2 about the mixing efficiency of the surviving motions in the saturated state, the existence of the Alfvén waves propagating along folds, etc., a detailed and systematic study of the velocity statistics and, especially, of the velocity–magnetic field correlations is required.

Very little numerical evidence on this subject is available in the literature. In part, this scarcity is due to the fact that even a qualitative physical picture of the magnetic back-reaction has been lacking, so it is not obvious what the interesting diagnostics are. Extant results include statements about the growth of $\langle \boldsymbol{u} \cdot \boldsymbol{B} \rangle$ correlations (Pouquet et al. 1986), positive correlation between high current and high rate of strain and alignment of magnetic field parallel to the vorticity vector (Miller et al. 1996), suppression of chaos of Lagrangian trajectories by the magnetic field (Cattaneo et al. 1996; Zienicke et al. 1998), and evidence of nonlocal interaction between large-scale velocities and small-scale magnetic fields based on energy transfer spectra (Kida et al. 1991; Cho & Vishniac 2000) and on experiments with switching off velocity field (Maron et al. 2004). All these results can be made sense of on the basis of more or less straightforward heuristic considerations. While they are all reflections of some underlying back-reaction mechanism, none of them tell us explicitly what this mechanism is. Much further analysis is necessary to diagnose it correctly. Such an analysis is the subject of our ongoing work.

6.3.2. Two-Point Statistics: Structure Functions

The second limitation we have imposed on ourselves is that all our higher order statistics are one point. We believe that most of the physics that is qualitatively understood is already captured in the diagnostics we employ. Obviously, two-point statistics contain a great wealth of information that cannot be accessed by the one-point approach. We do not, e.g., attempt to study two-point spatial intermittency of the magnetic field.

In recent years, there has been an explosion of interest in the scaling of structure functions in MHD turbulence. These are defined by $S_n(y) = \langle |\psi(\boldsymbol{x} + \boldsymbol{y}) - \psi(\boldsymbol{x})|^n \rangle \sim y^{\zeta_n}$, where ψ is the quantity of interest (e.g., the longitudinal velocity field $u_L = \boldsymbol{u} \cdot \boldsymbol{y}/y$). The present surge of interest followed the publication by She & Lévêque (1994) of a phenomenological formula for ζ_n in hydrodynamic turbulence and the remarkable success it enjoyed in reproducing experimental and numerical scalings. Their model requires as input parameters the codimension of the most singular dissipative structures and the dimensional scaling of the cascade (eddy turnover) time. Applications of their idea to the MHD turbulence followed: first, based on the $k^{-3/2}$ spectrum of Iroshnikov (1964) and Kraichnan (1965) (Grauer et al. 1994; Politano & Pouquet 1995), and then on the Kolmogorov $k^{-5/3}$ spectrum (Müller & Biskamp 2000; see Biskamp 2003 for a review). The latter model matched numerical data for decaying MHD turbulence. In recent simulations, good fits were obtained by choosing ad hoc fractional values for the codimension of the dissipative structures (Müller et al. 2003; Haugen et al. 2004).

Notably, these models seemed to work for structure functions not of velocity but of the Elsässer fields $\boldsymbol{z}^{\pm} = \boldsymbol{u} \pm \boldsymbol{B}$, and it has been implicitly or explicitly assumed that magnetic fields and velocities are symmetric as in an Alfvén wave. However, there was no such symmetry in either the decaying isotropic simulations of Biskamp & Müller (2000) or the forced ones of Haugen et al. (2004). Even in simulations with a mean field, the structure functions of $\boldsymbol{u}$ and $\boldsymbol{B}$, when measured separately, turned out to have different scalings, velocity

being less intermittent than the magnetic field (Cho et al. 2003). On a qualitative level, this property has, in fact, been seen in most numerical simulations since Meneguzzi et al. (1981).

Considering Elsässer field scalings is made attractive by the exact result of Politano & Pouquet (1998a) stating that a mixed third-order structure function $\langle [z^{\mp}(x + y) - z^{\mp}(x)] \cdot (y/y)|z^{\pm}(x + y) - z^{\pm}(x)|^2\rangle \propto y$ has a linear inertial range scaling analogous to Kolmogorov's $\frac{4}{5}$ law (this result only holds for $\mathrm{Pr} = 1$; for arbitrary Pr, linear scaling was also proved for two other mixed triple correlators—not structure functions—of u and B; see Politano & Pouquet 1998b). Thus, while the Politano-Pouquet laws provide a set of constraints on u-B (or z^+-z^-) correlations, they do not have exact implications for any structure functions involving u, B, z^+, or z^- alone.

It is worthwhile to recall that the reason structure functions are the diagnostics of choice in hydrodynamic turbulence is the Galilean invariance of the velocity field: only velocity differences are really interesting. Phenomenological models of intermittency, the She-Lévêque model included, assume that interactions occur between comparable scales (locally in k space), thus giving rise to an energy cascade. Neither Galilean invariance nor k-space locality of interactions holds for magnetic fields: a constant magnetic field cannot be transformed out, and an interaction between velocity and magnetic fields at disparate scales is exactly what the small-scale dynamo is. The open questions are then (1) whether models in the mold of She-Lévêque are justified for MHD and, if they work, why they do so; and (2) whether, in view of the asymmetry between magnetic field and velocity, the Elsässer fields are meaningful.

Thus, analyzing two-point statistics of MHD turbulence is complicated by the unanswered questions about the basic structure of this turbulence and by the lack of clarity about what set of diagnostics constitutes a physically interesting and informative description. We leave these matters to future work.

7. SUMMARY

We now itemize the main points of this paper:

1. Magnetic fields and turbulence in astrophysical plasmas exist and interact at many disparate scales, which makes full global description unachievable by brute-force numerical simulations. We concentrate on small-scale turbulent fields to probe universal physics independent of large-scale object-specific features. In this spirit, we simulate incompressible, isotropic, homogeneous, randomly forced, nonhelical MHD turbulence in a periodic box.

2. If no mean field is imposed, all magnetic fields in the system are generated by the small-scale dynamo, which consists in random stretching and folding of the field lines and is best revealed in the limit of large Pr_m. In its kinematic stage, this dynamo is a one-timescale process insensitive to the particulars of the random flow. In Kolmogorov turbulence, it is controlled by the viscous-scale turbulent eddies. It can, therefore, be studied in the numerically feasible limit of $\mathrm{Re} \sim 1$ and $\mathrm{Pr}_m \gg 1$ with random external forcing. In this viscosity-dominated regime, we are able to carry out a parameter scan in Pr_m. This regime is a model for interaction between magnetic fields and the viscous-scale eddies, the forcing representing energy input from the larger scale eddies.

3. The salient feature of the small-scale dynamo is that it produces highly intermittent and structured fields. These fields are organized in folds whose length is comparable to the flow scale but that contain fields that reverse direction at the resistive scale. The scale separation between these scales is $\sim\mathrm{Pr}_m^{1/2}$. We diagnose the folded structure by measuring various average scale lengths of the field, the spectrum of the magnetic tension, the distributions of the field strength and of the field-line curvature, and the (anti)correlation between them. The folded structure implies that the system becomes nonlinear (the fields start reacting back on the flow via the Lorentz tension force) when the energy of the folded field becomes comparable to the energy of the viscous-scale eddies.

4. The folded structure is found to persist after the dynamo becomes nonlinear and saturates.

5. Saturation of the dynamo can be achieved via partial two-dimensionalization of the velocity gradient statistics with respect to the local direction of the folds, so that saturation is a result of quasi–two-dimensional mixing balancing weakened stretching of the field by the anisotropized flow. This mechanism is sufficiently robust for a simple semiquantitative model of saturation based on it to predict magnetic energy spectra in excellent agreement with the numerical results for the viscosity-dominated runs.

6. The folded structure is essential in saturation physics: while the magnetic field is formally small scale (as a result of direction reversals), the folds themselves possess spatial coherence at the flow scale, which allows them to exert a back-reaction on the flow. Both small-scale dynamo and this nonlinear back-reaction exemplify the nonlocality in k space of the interactions between the velocity and magnetic fields in MHD turbulence.

7. While the regime with both large Re and large Pr_m is not accessible at current resolutions, some progress is achieved by simulating the case of $\mathrm{Re} \gg 1$ and $\mathrm{Pr}_m \gtrsim 1$. The small-scale dynamo at $\mathrm{Pr}_m \sim 1$ belongs to the same class as the large-Pr_m dynamo: the magnetic field is generated at scales somewhat smaller than viscous and has a structure qualitatively similar to the folded structure of the fields in large-Pr_m viscosity-dominated runs.

8. In turbulence with large Re, the nature of the saturated state depends on how efficiently the anisotropized velocity gradients can mix the magnetic field lines. If mixing by the inertial range motions were unsuppressed, the magnetic energy would saturate at a below-equipartition level comparable to the energy of the viscous-scale eddies. Numerical evidence, while not definitive, does not appear to support such an outcome.

9. If both stretching and mixing are suppressed, we predict an intermediate nonlinear regime with magnetic energy growing proportionally to time from the viscous eddy to the outer eddy energy (increase by a factor of $\mathrm{Re}^{1/2}$), the fold length increasing to the outer scale (a factor of $\mathrm{Re}^{3/4}$), and the resistive scale increasing via selective decay by a lesser factor of $\mathrm{Re}^{1/4}$. While these scalings cannot be verified at current resolutions, we find clear evidence of an intermediate nonlinear growth regime featuring both fold elongation and selective decay.

10. The fully developed, forced, isotropic MHD turbulence is the saturated state of the small-scale dynamo. While phenomenological thinking rooted in the Alfvén wave physics of the MHD turbulence with a strong mean field leads one to expect a state of scale-by-scale equipartition between magnetic and kinetic energy and a Kolmogorov scaling of the spectra, none of the extant numerical evidence supports this view. Instead, the kinetic energy spectrum is dominated by the outer scale and has a steeper than Kolmogorov scaling in the inertial range, while the magnetic energy is dominated by small scales, at which it substantially exceeds kinetic energy.

11. Based on our numerical results and heuristic arguments, we conjecture that the saturated state of the dynamo is controlled by the balance of mixing and stretching by the anisotropized outer-scale turbulent motions. The magnetic fields in the saturated state are then a superposition of folds and Alfvén-like waves that can propagate along the folds. The existence of these waves in the inertial range is predicated on their not being efficient mixers of the magnetic fields. These waves are not as yet numerically detectable and, therefore, remain hypothetical.

In the context of our scenarios of saturation with efficient and inefficient mixing, it is interesting to recall the two basic alternatives put forward more than 50 years ago: magnetic energy saturation at the viscous eddy energy and scale (Batchelor 1950) or eventual equipartition between the magnetic and kinetic energy at all scales (Schlüter & Biermann 1950; Biermann & Schlüter 1951). Biermann & Schlüter's reasoning assumed interactions only between velocities and magnetic fields at the same scale. Batchelor's argument was based on the analogy between the evolution equations for the magnetic field and vorticity $\nabla \times u$. While this analogy has since been realized to be flawed even for $\mathrm{Pr}_m = 1$ (note the recent numerical investigations of this issue by Ohkitani 2002; Tsinober & Galanti 2003) and the magnetic fields have been shown to propagate to the resistive scale, it is still a theoretical and numerical challenge to demonstrate that magnetic energy grows above the viscous eddy energy and to explain why it can do so.

Since the time these alternatives were formulated, theoretical predictions and numerical results have ranged from completely ruling out the small-scale dynamo (Saffman 1963), to predicting magnetic energy pileup at the resistive scale (Vainshtein & Cattaneo 1992), to closure-based confirmation of scale-by-scale equipartition (Pouquet et al. 1976), to direct numerical simulations interpreted as evidence that there is a tendency toward the equipartition or, at least, Kolmogorov scaling (Haugen et al. 2003), to direct numerical simulations interpreted as evidence that such an equipartition is lacking (Maron et al. 2004). While our understanding of these alternatives has improved, the original dichotomy continues to define the terms of the debate.

The purpose of the present paper has been to collect a set of numerical results and physical considerations emphasizing the nonlocal (in k space) nature of the velocity–magnetic field interaction and the resulting dominance of magnetic fluctuations at small scales, which we believe to be the defining properties of isotropic MHD turbulence.

REFERENCES

Archontis, V., Dorch, S. B. F., & Nordlund, Å. 2003a, A&A, 397, 393
———. 2003b, A&A, 410, 759
Artamonova, O. V., & Sokoloff, D. D. 1986, Vestn. Mosk. Univ. Ser. 3. Fiz. Astron., 27, 8
Balbus, S. A. 2004, ApJ, submitted (astro-ph/0403678)
Balbus, S. A., & Hawley, J. F. 1998, Rev. Mod. Phys., 70, 1
Balsara, D. S., Kim, J., MacLow, M. M., & Mathews, G. 2004, preprint (astro-ph/0403660)
Batchelor, G. K. 1950, Proc. R. Soc. London A, 201, 405
———. 1959, J. Fluid Mech., 5, 113
Beck, R. 2000, Philos. Trans. R. Soc. London A, 358, 777
———. 2001, Space Sci. Rev., 99, 243
Beck, R., Brandenburg, A., Moss, D., Shukurov, A., & Sokoloff, D. 1996, ARA&A, 34, 155
Biermann, L., & Schlüter, A. 1951, Phys. Rev., 82, 863
Biskamp, D. 2003, Magnetohydrodynamic Turbulence (Cambridge: Cambridge Univ. Press)
Biskamp, D., & Müller, W.-C. 2000, Phys. Plasmas, 7, 4889
Boldyrev, S. A. 2001, ApJ, 562, 1081
Boldyrev, S. A., & Cattaneo, F. 2004, Phys. Rev. Lett., 92, 144501
Boldyrev, S. A., Nordlund, Å., & Padoan, P. 2002, Phys. Rev. Lett., 89, 031102
Boldyrev, S. A., & Schekochihin, A. A. 2000, Phys. Rev. E, 62, 545
Braginskii, S. I. 1965, Rev. Plasma Phys., 1, 205
Brandenburg, A. 2001, ApJ, 550, 824
Brandenburg, A., Jennings, R. L., Nordlund, Å., Rieutord, M., Stein, R. F., & Tuominen, I. 1996, J. Fluid Mech., 306, 325
Brandenburg, A., Procaccia, I., & Segel, D. 1995, Phys. Plasmas, 2, 1148
Brandenburg, A., & Subramanian, K. 2000, A&A, 361, L33
———. 2004, Phys. Rep., submitted (astro-ph/0405052)
Brandenburg, A., & Zweibel, E. G. 1994, ApJ, 427, L91
Brummell, N. H., Cattaneo, F., & Tobias, S. M. 2001, Fluid Dyn., 28, 237
Carilli, C. L., & Taylor, G. B. 2002, ARA&A, 40, 319
Cattaneo, F. 1999, ApJ, 515, L39

Cattaneo, F., Hughes, D. W., & Kim, E. 1996, Phys. Rev. Lett., 76, 2057
Cattaneo, F., Kim, E., Proctor, M., & Tao, L. 1995, Phys. Rev. Lett., 75, 1522
Chandran, B. D. G. 1997, ApJ, 482, 156
Chertkov, M., Falkovich, G., Kolokolov, I., & Vergassola, M. 1999, Phys. Rev. Lett., 83, 4065
Childress, S., & Gilbert, A. 1995, Stretch, Twist, Fold: The Fast Dynamo (Berlin: Springer)
Cho, J., Lazarian, A., & Vishniac, E. T. 2002, ApJ, 564, 291
———. 2003, ApJ, 595, 812
Cho, J., & Vishniac, E. T. 2000, ApJ, 538, 217
Chou, H. 2001, ApJ, 556, 1038
Christensen, U., Olson, P., & Glatzmaier, G. A. 1999, Geophys. J. Int., 138, 393
Constantin, P., Procaccia, I., & Segel, D. 1995, Phys. Rev. E, 51, 3207
Drummond, I. T., & Münch, W. 1991, J. Fluid Mech., 225, 529
Fereday, D. R., & Haynes, P. H. 2004, Phys. Fluids, submitted
Ferrière, K. 2001, Rev. Mod. Phys., 73, 1031
Foote, E. A., & Kulsrud, R. M. 1979, ApJ, 233, 302
Frisch, U. 1995, Turbulence: The Legacy of A. N. Kolmogorov (Cambridge: Cambridge Univ. Press)
Frisch, U., Pouquet, A., Léorat, J., & Mazure, A. 1975, J. Fluid Mech., 68, 769
Galanti, B., Sulem, P. L., & Pouquet, A. 1992, Geophys. Astrophys. Fluid Dyn., 66, 183
Goldhirsch, I., Sulem, P.-L., & Orszag, S. A. 1987, Physica D, 27, 311
Goldreich, P., & Sridhar, S. 1995, ApJ, 438, 763
Grauer, R., Krug, J., & Marliani, C. 1994, Phys. Lett. A, 195, 335
Gruzinov, A., Cowley, S., & Sudan, R. 1996, Phys. Rev. Lett., 77, 4342
Han, J. L., Ferrière, K., & Manchester, R. N. 2004, ApJ, 610, 820
Han, J.-L., & Wielebinski, R. 2002, Chinese J. Astron. Astrophys., 2, 293
Haugen, N. E. L., Brandenburg, A., & Dobler, W. 2003, ApJ, 597, L141
———. 2004, Phys. Rev. E, submitted (astro-ph/0307059)
Hughes, D. W., Cattaneo, F., & Kim, E.-J. 1996, Phys. Lett. A, 223, 167
Iroshnikov, P. 1964, Soviet Astron., 7, 566
Kazantsev, A. P. 1968, Soviet Phys.—JETP, 26, 1031

Kida, S., Yanase, S., & Mizushima, J. 1991, Phys. Fluids A, 3, 457
Kim, E. 1999, Phys. Lett. A, 259, 232
———. 2000, Phys. Plasmas, 7, 1746
Kim, E. J., & Diamond, P. H. 2002, ApJ, 578, L113
Kinney, R. M., Chandran, B., Cowley, S., & McWilliams, J. C. 2000, ApJ, 545, 907
Kleeorin, N., Rogachevskii, I., & Sokoloff, D. 2002, Phys. Rev. E, 65, 036303
Kleva, R. G., & Drake, J. F. 1995, Phys. Plasmas, 2, 4455
Kraichnan, R. H. 1965, Phys. Fluids, 8, 1385
———. 1968, Phys. Fluids, 11, 945
Kronberg, P. P. 1994, Rep. Prog. Phys., 57, 325
———. 2002, Phys. Today, 55, 40
Kronberg, P. P., Dufton, Q. W., Li, H., & Colgate, S. A. 2001, ApJ, 560, 178
Kulsrud, R. M. 1999, ARA&A, 37, 37
Kulsrud, R. M., & Anderson, S. W. 1992, ApJ, 396, 606
Kulsrud, R. M., Cen, R., Ostriker, J. P., & Ryu, D. 1997a, ApJ, 480, 481
Kulsrud, R. M., Cowley, S. C., Gruzinov, A. V., & Sudan, R. N. 1997b, Phys. Rep., 283, 213
Maksymczuk, J., & Gilbert, A. 1999, Geophys. Astrophys. Fluid Dyn., 90, 127
Malyshkin, L. 2001, ApJ, 559, 304
Malyshkin, L., & Kulsrud, R. 2002, ApJ, 571, 619
Maron, J. L., & Blackman, E. G. 2002, ApJ, 566, L41
Maron, J. L., Cowley, S. C., & McWilliams, J. C. 2004, ApJ, 603, 569
Maron, J. L., & Goldreich, P. 2001, ApJ, 554, 1175
Meneguzzi, M., Frisch, U., & Pouquet, A. 1981, Phys. Rev. Lett., 47, 1060
Miller, R. S., Mashayek, F., Adumitroaie, V., & Givi, P. 1996, Phys. Plasmas, 3, 3304
Mininni, P. D., Gomez, D. O., & Mahajan, S. M. 2003, ApJ, 587, 472
Minter, A. H., & Spangler, S. R. 1996, ApJ, 458, 194
Moffatt, H. K. 1978, Magnetic Field Generation in Electrically Conducting Fluids (Cambridge: Cambridge Univ. Press)
Montgomery, D. 1992, J. Geophys. Res. A, 97, 4309
Müller, W.-C., & Biskamp, D. 2000, Phys. Rev. Lett., 84, 475
Müller, W.-C., Biskamp, D., & Grappin, R. 2003, Phys. Rev. E, 67, 066302
Nazarenko, S. V., Falkovich, G. E., & Galtier, S. 2001, Phys. Rev. E, 63, 016408
Nazarenko, S. V., West, R. J., & Zaboronski, O. 2003, Phys. Rev. E, 68, 026311
Nordlund, Å., Brandenburg, A., Jennings, R. L., Rieutord, M., Ruokolainen, J., Stein, R. F., & Tuominen, I. 1992, ApJ, 392, 647
Nore, C., Brachet, M. E., Politano, H., & Pouquet, A. 1997, Phys. Plasmas, 4, 1
Ohkitani, K. 2002, Phys. Rev. E, 65, 046304
Ossendrijver, M. 2003, A&A Rev., 11, 287
Ott, E. 1998, Phys. Plasmas, 5, 1636
Parker, E. N. 1979, Cosmic Magnetic Fields: Their Origin and Activity (Oxford: Clarendon)
Pierrehumbert, R. T. 1994, Chaos Solitons Fractals, 4, 1091
———. 2000, Chaos, 10, 61
Politano, H., & Pouquet, A. 1995, Phys. Rev. E, 52, 636
———. 1998a, Geophys. Res. Lett., 25, 273
———. 1998b, Phys. Rev. E, 57, R21
Porter, D., Pouquet, A., & Woodward, P. 2002, Phys. Rev. E, 66, 026301
Pouquet, A., Frisch, U., & Léorat, J. 1976, J. Fluid Mech., 77, 321
Pouquet, A., Meneguzzi, M., & Frisch, U. 1986, Phys. Rev. A, 33, 4266
Proctor, M. R. E., & Zweibel, E. G. 1992, Geophys. Astrophys. Fluid Dyn., 64, 145

Rädler, K.-H., Kleeorin, N., & Rogachevskii, I. 2003, Geophys. Astrophys. Fluid Dyn., 97, 249
Rogachevskii, I., & Kleeorin, N. 1997, Phys. Rev. E, 56, 417
Rothstein, D., Henry, E., & Gollub, J. P. 1999, Nature, 401, 770
Ruzmaikin, A. A., Shukurov, A. M., & Sokoloff, D. D. 1988, Magnetic Fields of Galaxies (Dordrecht: Kluwer)
Saffman, P. G. 1963, J. Fluid Mech., 16, 545
Schekochihin, A. A., Boldyrev, S. A., & Kulsrud, R. M. 2002a, ApJ, 567, 828
Schekochihin, A. A., Cowley, S. C., Hammett, G. W., Maron, J. L., & McWilliams, J. C. 2002b, New J. Phys., 4, 84
Schekochihin, A. A., Cowley, S., Maron, J., & Malyshkin, L. 2002c, Phys. Rev. E, 65, 016305
Schekochihin, A. A., Cowley, S. C., Maron, J. L., & McWilliams, J. C. 2004a, Phys. Rev. Lett., 92, 054502
Schekochihin, A. A., Cowley, S. C., Taylor, S. F., Hammett, G. W., Maron, J. L., & McWilliams, J. C. 2004b, Phys. Rev. Lett., 92, 084504
Schekochihin, A. A., & Kulsrud, R. M. 2001, Phys. Plasmas, 8, 4937
Schekochihin, A. A., Maron, J. L., Cowley, S. C., & McWilliams, J. C. 2002d, ApJ, 576, 806
Schlüter, A., & Biermann, L. 1950, Z. Naturforsch., 5, 237
She, Z. S., & Lévêque, E. 1994, Phys. Rev. Lett., 72, 336
Spitzer, L. 1962, Physics of Fully Ionized Gases (New York: Wiley)
Subramanian, K. 1997, preprint (astro-ph/9708216)
———. 1999, Phys. Rev. Lett., 83, 2957
———. 2003, Phys. Rev. Lett., 90, 245003
Sukhatme, J., & Pierrehumbert, R. T. 2002, Phys. Rev. E, 66, 056302
Thelen, J.-C., & Cattaneo, F. 2000, MNRAS, 315, L13
Thiffeault, J.-L. 2004, Physica D, in press (nlin.CD/0204069)
Title, A. 2000, Philos. Trans. R. Soc. London A, 358, 657
Tobias, S. M. 2002, Philos. Trans. R. Soc. London A, 360, 2741
Tsinober, A., & Galanti, B. 2003, Phys. Fluids, 15, 3514
Vainshtein, S. I. 1972, Soviet Phys.—JETP, 35, 725
———. 1980, Soviet Phys.—JETP, 52, 1099
———. 1982, Soviet Phys.—JETP, 56, 86
Vainshtein, S. I., & Cattaneo, F. 1992, ApJ, 393, 165
Vainshtein, S. I., & Kichatinov, L. L. 1983, Geophys. Astrophys. Fluid Dyn., 24, 273
Vainshtein, S. I., Sagdeev, R. Z., Rosner, R., & Kim, E.-J. 1996, Phys. Rev. E, 53, 4729
Vainshtein, S. I., & Zel'dovich, Ya. B. 1972, Soviet Phys.—Uspekhi, 15, 159
Vallée, J. P. 1997, Fundam. Cosmic Phys., 19, 1
———. 1998, Fundam. Cosmic Phys., 19, 319
Weiss, N. O., & Tobias, S. M. 2000, Space Sci. Rev., 94, 99
West, R., Nazarenko, S., Laval, J.-P., & Galtier, S. 2004, A&A, 414, 807
Widrow, L. M. 2002, Rev. Mod. Phys., 74, 775
Zel'dovich, Ya. B. 1957, Soviet Phys.—JETP, 4, 460
Zel'dovich, Ya. B., Ruzmaikin, A. A., Molchanov, S. A., & Sokoloff, D. D. 1984, J. Fluid Mech., 144, 1
Zienicke, E., Politano, H., & Pouquet, A. 1998, Phys. Rev. Lett., 81, 4640
Zweibel, E. G. 1988, ApJ, 329, 384
———. 2002, ApJ, 567, 962
Zweibel, E. G., & Heiles, C. 1997, Nature, 385, 131